# Experimental Analysis and Numerical Modeling of the Friction Drilling Process

by

Scott F. Miller

A dissertation submitted in partial fulfillment
of the requirements for the degree of
Doctor of Philosophy
(Mechanical Engineering)
in The University of Michigan
2006

Doctoral Committee:

Associate Professor Albert J. Shih, Chair
Professor J. Wayne Jones
Professor Jun Ni
Associate Professor Claus Borgnakke

# DEDICATION

To My Parents

# ACKNOWLEDGEMENTS

I sincerely appreciate my advisor, Professor Albert Shih, for giving me the opportunity to explore this topic. I have learned and improved a lot with your encouragement, insightful advices, and guidance in the last five years. Your suggestions, effort, time, and energy help me develop the ideas that made the research a success.

I would like to thank my advisory committee members, Professor Jun Ni, Professor J. Wayne Jones, and Associate Professor Claus Borgnakke for your guidance and help.

I thank Phil Sklad, Peter Blau, Sam McSpadden, and Jun Qu for their guidance and support at Oak Ridge National Laboratory. I am very grateful to Tom Geer, Randy Parten, Tyler Jenkins, Jason Braden, Zhili Feng, Brian Jolly, and Chris Cofer for their technical help in my research. I would also like to thank the sponsor of this research, Oak Ridge National Laboratory.

I thank my parents as well as my brother and sister for their unfailing support and encouragement. I appreciate the help and suggestions from my research colleges; Rui Li, Jia Tao, Chen-Chun Kao, Steve White, Jie Luo, Steve Erskin, Zhenhua Huang, Honghai Zhu, Yingzhen Zhu, and Bin Shen.

# TABLE OF CONTENTS

# LIST OF TABLES

# LIST OF FIGURES

# ABSTRACT

Friction drilling is a nontraditional hole-making process. A rotating conical tool is applied to penetrate a hole and create a bushing in a single step without generating chip. The friction drilling process relies on the heat generated from the frictional force between the tool and sheet metal workpiece to soften, penetrate, and deform the work-material into a bushing.

Under the constant tool feed rate, the experimentally measured thrust force and torque were analyzed. The infrared camera system was applied to measure the temperature of the tool and workpiece.

High temperature and strain affect material properties and grain microstructure of the material surrounding a hole from friction drilling. Samples of cross sectioned holes were polished and etched for material analysis in carbon steel, alloy steel, aluminum and titanium. Knoop micro-hardness values were recorded and near hole microstructure was observed with optical micrographs.

The technical challenge for the brittle cast aluminum and magnesium alloys is to generate a cylindrical shaped bushing without significant radial fracture or petal formation. Two ideas of pre-heating the workpiece and high speed friction drilling were investigated. The thrust force and torque decreased and the bushing shape was improved with increased workpiece temperature.

The wear of a hard tungsten carbide tool used for friction drilling a low carbon steel workpiece was investigated. Measurements were made to characterize tool wear and monitor the effects of tool wear. Results indicate that the carbide tool is durable, showing minimal tool wear after drilling 11000 holes, but observations also indicate the progressively severe abrasive grooving on the tool tip.

The analytical model was created to predict the thrust force and torque in friction drilling based on the measured temperature, material properties, and estimated area of

contact. The explicit finite element method (FEM) was applied to model the large deformation, large plastic strain, and high temperature work-material deformation in the friction drilling process. Thrust force, torque, and temperature in FEM were compared to experimentally measured values. Workpiece temperature was found to approach the work-material solidus temperature. Distributions of plastic strain, temperature, and stress demonstrated the thermo-mechanical response of the workpiece.

# CHAPTER 1.

# INTRODUCTION

## 1.1. Background

Friction drilling, also known as thermal drilling, flow drilling, form drilling, or friction stir drilling, is a nontraditional hole-making method. The heat generated from friction between a rotating conical tool and the workpiece is used to soften the work-material and penetrate a hole. Figure 1.1 shows a schematic illustration of the five steps in friction drilling. The tip of the conical tool approaches and contacts the workpiece, as shown in Fig. 1.1(a). The tool tip, like the web center in twist drill, indents into the workpiece and supports the drill in both the radial and axial directions. Friction on the contact surface, created from axial force and relative angular velocity between tool and workpiece, produces heat and softens the workpiece material. As the tool is extruded into the workpiece, as shown in Fig. 1.1(b), it initially pushes the softened work-material sideward and upward. With the workpiece material heated and softened the tool is able to pierce through the workpiece, as shown in Fig. 1.1(c). Once the tool penetrates the workpiece, as shown in Fig. 1.1(d), the tool moves further forward to push aside more workpiece material and form the bushing using the cylindrical part of the tool. As the process is completed, the shoulder of the tool may contact the workpiece to collar the back extruded burr on the bushing. Finally, the tool retracts and leaves a hole with a bushing on the workpiece (Fig. 1.1(e)).

Friction drilling is a technique to create a bushing on sheet metal, tubing, or thin walled profiles for joining devices in a simple, efficient way. The bushing created in the process is usually two to three times as thick as the original workpiece. This added thickness can be threaded, providing a more solid connection for attachment than attempting to thread the original sheet. Figure 1.2 shows a cross section of the bushing

produced for a tapped and untapped hole. All work-material from the hole contributes to form the bushing. In addition, no cutting fluid or lubricant is necessary, which makes friction drilling a totally clean, environmentally friendly process.

## 1.2. Research motivation

In the automotive assembly plant, joining devices to sheet metal, tubing, or thin walled profiles in an effective way is a manufacturing challenge. Current processes, including weld nuts or threaded inserts, generally require welding or attaching by some other means, a small part to a piece of sheet metal that has been stamped or drilled. Methods currently employed include the weld nut, clench nut, J-nut and other threaded insert. These are designed to provide a larger number of engaged threads and thus higher clamping forces. A few examples are shown in Fig. 1.3. Weld nuts are actually welded to the sheet metal component or, in some cases, to a thicker reinforcing bracket. They differ slightly from clench nuts, which are generally inserted into a "clenching cavity" to locate them and prevent them from rotating. Clench nuts are also frequently welded into place to prevent them from moving prior to assembly. J-nuts are spring clips that are J-shaped or U-shaped and are inserted into a square opening that is usually stamped into a sheet-metal component. The nut provides contact area for only a single thread depth, so it is used for items that require very limited clamping force. J-nuts are generally inserted by hand just before the fastened component is attached with a hand-held power tool (often referred to as a nut runner, even though it more often runs a screw or bolt rather than a nut).

Friction drilling can simplify the joining process. First, it simplifies production. Processes of stamping holes and welding nuts or attaching clips, required for attaching a device in sheet metal, are replaced by a single friction drilling step. Second, the required equipment is reduced. Complicated robots employed to weld each nut to the sheet metal at the desired location of the stamped hole is eliminated. Instead, a simple friction drilling machining center can be used. Third, costs of inventory and keeping up with different weld nuts and threaded inserts are reduced. Fourth, friction drilling reduces waste of material. All material from the drilled hole is transformed to create the bushing.

This decreases chip cleaning and disposal cost. Fifth, a connection with a friction drilled hole is lighter than with most weld nuts or threaded inserts. The tapping method currently used employs a forming tap, and is also without chip. Thread forming fasteners (TFF) can be incorporated with the drilled hole [1]. This eliminates step of form tapping and adds to appeal of friction drilling.

Potential automotive applications for friction drilling are shown in Fig. 1.4. These include seat frame, exhaust system parts, fuel rail, seat handle, foot pedal, oxygen sensor, and castings. It is believed that the friction drilling technique can be applied on a broader scale in automotive industry. Potential for substitution of a friction drilling fastening process will need to be evaluated on a case-by-case basis. Aluminum and magnesium castings require bolt bosses and thick flanges to accommodate fastening. In hydro-formed components, punching holes and attaching weld nuts and clinch nuts are very difficult and/or expensive to accomplish. In certain cases, it appears that sheet metal components are made thicker than necessary for the sole purpose of providing more thread engagement for fasteners. In other cases a threaded hole is needed for attachment of an electrical ground, which requires little load carrying capability.

## 1.3. Literature review

The idea of rubbing two materials together to produce heat is as old as people learning to make fire in the stone age. However, applying the principle to drilling holes in metal is a more recent development. Most people who have worked in machine shops have at one time or another tried to drill a hole with a very dull bit. The result is a lot of smoke and heat. Jan Claude de Valliere, working on a little farm in the south of France some seventy-five years ago encountered the same problem [2]. He recognized that if enough heat is generated he could melt and form a hole through the metal. With that thought in mind, he developed a special drill designed to increase friction. After many trials, he found a shape that worked. Jan Claude de Valliere's invention was not at the time commercially or practically viable.

Publications on the subject of friction drilling are limited. Six patents have been awarded: first four by van Geffen [3-6] in 1976-80 and later by Head et al. [7] and

Hoogenboom [8] in 1984. France et al. [9-11] investigates the strength characteristics of friction drilled holes in metal tubing. Overy [12] and Bak [13] discussed the design aspect of the friction drilled holes. Kerkhofs et al. [14] studied the performance of coated friction drilling tools. These publications describe friction drilling tools, equipment needed, and evaluate performance issues of the tool and bushing created. However, past work has approached friction drilling with a "black box" point of view. In depth study of the friction drilling process is the purpose of this research. A complete analysis of the friction drilling process was performed for basic understanding of mechanics and details.

Friction drilling is similar in concept to friction stir welding (FSW). FSW is a solid state joining process invented in 1991 by The Welding Institute in Cambridge, UK [15,16]. Figure 1.5 gives a visual representation of FSW. In this process a rotating tool is used to generate frictional heat and create forging to facilitate continuous solid state joints. The tool consists of a pin, which protrudes from the lower surface of the tool, and the relatively large-diameter shoulder. Welding is initiated by first plunging the pin into the workpieces until the shoulder is in intimate contact with the component top surfaces. Friction heat is then generated as the shoulder rubs on the top surface under an apparent force. Once sufficient heat is generated and conducted into the workpiece, the tool is propelled forward. Material is softened by the heating action of the shoulder, and transported by the pin across the bondline, facilitating the joint. The only significant difference is that friction drilling heats and softens material to displace it and form a specific shape, while friction stir welding heats and softens material to mix and join it. Because of the obvious similarities between FSW and friction drilling, and the lack of publications on friction drilling, reference was made to papers on the subject of FSW in this research.

## 1.4. Frictional contact condition

The frictional phenomena that occur in friction drilling are complicated. Bowden proposed the welding, shearing, and ploughing theory of friction in 1950 for metals [17]. For friction drilling, friction between the tool and workpiece is described by adhesion and deformation in this theory. For the adhesion component of friction, local welding occurs

at the tips of asperities on the surfaces of the tool and workpiece, and the welded junctions are sheared due to the relative sliding between the surfaces. For the deformation or ploughing component, asperities in the harder tool surface plough through the softer work-material. In the normal case of dry sliding between rough surfaces, the contribution to friction from adhesion is at least twice as large as from deformation [17].

The local welding of the work-material to the friction drilling tool occurs because of the general nature of plastic flow of metals. When stress exceeds a critical value, there is a "plastic state" in which the work-material will flow in a manner similar to a highly viscous liquid [18]. However, most metals subject to plastic flow work harden appreciably, and the strength of a welded junction is therefore often greater than that of the softer work-material, which causes the shearing to take place inside the softer work-material.

Coefficient of friction is commonly used to quantify the friction behavior. The value of coefficient of friction depends on many factors and is very difficult to accurately quantify under complex contact conditions. Surface sliding conditions, including the contact pressure and speed, vary in friction drilling as the conical tool moves through the workpiece. Frictional heating at the tool-workpiece interface and workpiece temperature increase as sliding speed increases. This complicates experimental measurement of coefficient of friction with varying thermal and mechanical properties. Experimental measurement of coefficient of friction is not in the scope of this research.

## 1.5. Research issues

This study aims to provide deeper understanding of the friction drilling process. Details of problems and approaches in friction drilling are studied in the following sections of this dissertation.

### 1.5.1. Experimental analysis of the friction drilling process

The force, torque, and temperature in the friction drilling process have not been studied. It is the goal of this study to measure and characterize the thrust force, torque,

and temperature. Analysis of experimentally measured thrust force, torque, and temperature is needed to better understand underlying friction and heat generation.

Chapter 2 presents experimental analysis of thrust force, torque, and temperature in friction drilling. An experiment using a computer numerically controlled (CNC) mill and data acquisition system was set up to measure the thrust force and torque required to drill a hole. A method was devised to analyze the thrust force and torque at different stages of workpiece formation in the friction drilling process. A similar experiment was setup with the non-contact infrared (IR) camera system to measure the tool and workpiece temperatures during friction drilling. Calibration of the camera was necessary due to unknown emissivities of the tool and workpiece.

### 1.5.2. Microstructural alterations associated with friction drilling of steel, aluminum, and titanium

In the friction drilling process, workpiece microstructure and material properties change due to high strain and temperature. However, details of these changes have not been investigated for different work-materials. Hardness and strength of the material in the bushing and near the hole wall is also a concern. Studying the effect of friction drilling on workpiece grain microstructure, micro hardness, and bushing morphology is a goal of this research. Chapter 3 focuses on the metallurgical and micro-structural alterations produced as a result of friction drilling in four workpiece materials: AISI 4130 and 1020 steel, aluminum alloy 5052, and commercially pure (CP) titanium.

### 1.5.3. Friction drilling of cast metals

Cast metals exhibit the brittle property unappealing to friction drilling. For example, Fig. 1.6 shows the petaling problem of a hole in brittle cast aluminum material. The hole in Fig. 1.6 exhibits an undesirable bushing shaped like a flower. This is due to brittle fracture and radial peeling of work-material. Additional processes incorporated with friction drilling, such as workpiece preheating, have been developed to improve process effectiveness and flexibility. The goal of the research in Chapter 4 is to overcome the poor bushing shape due to the material fracture in friction drilling.

### 1.5.4. Tool wear

One of the major unanswered questions in friction drilling is the tool life. High temperature and force instigate questions about tool durability. Tool wear is a concern because it affects the characteristics and tolerances that are achievable. Different methods were applied to characterize effects of tool wear including the measurement of tool profile, tool weight, and microscopy. Results are discussed in Chapter 5.

### 1.5.5. Analytical and FEM modeling of the friction drilling process

A major challenge in friction drilling and related friction stir technologies is the process modeling. Accurate numerical models for friction drilling are lacking because large work-material deformation cause problems with simulation convergence and completion. Prior knowledge about distributions of stress, strain, temperature, etc. is not available. With proper modeling techniques, these can be generated.

In Chapter 6, two models are developed for friction drilling. One is a model to predict the thrust force and torque in friction drilling based on the measured temperature, material properties, and estimated area of contact. This model is applied to the friction drilling experiment in Chapter 2 for comparison. A finite element model using the ABAQUS/Explicit software was created for a more comprehensive approach. An investigation was conducted to determine the most acceptable coefficient of friction for the model. Experiments with similar process parameters were conducted for validation of thrust force, torque, and temperature generated in the model. This study builds the foundation for friction drilling prediction and process optimization.

### 1.5.6. Future work

The future work of this research is described in Chapter 7. A more inclusive friction model is needed to understand tribological aspects of the process and improve FEM. The model techniques can be extended to other friction stir technologies. Ideas for further optimization of friction drilling cast metals are discussed.

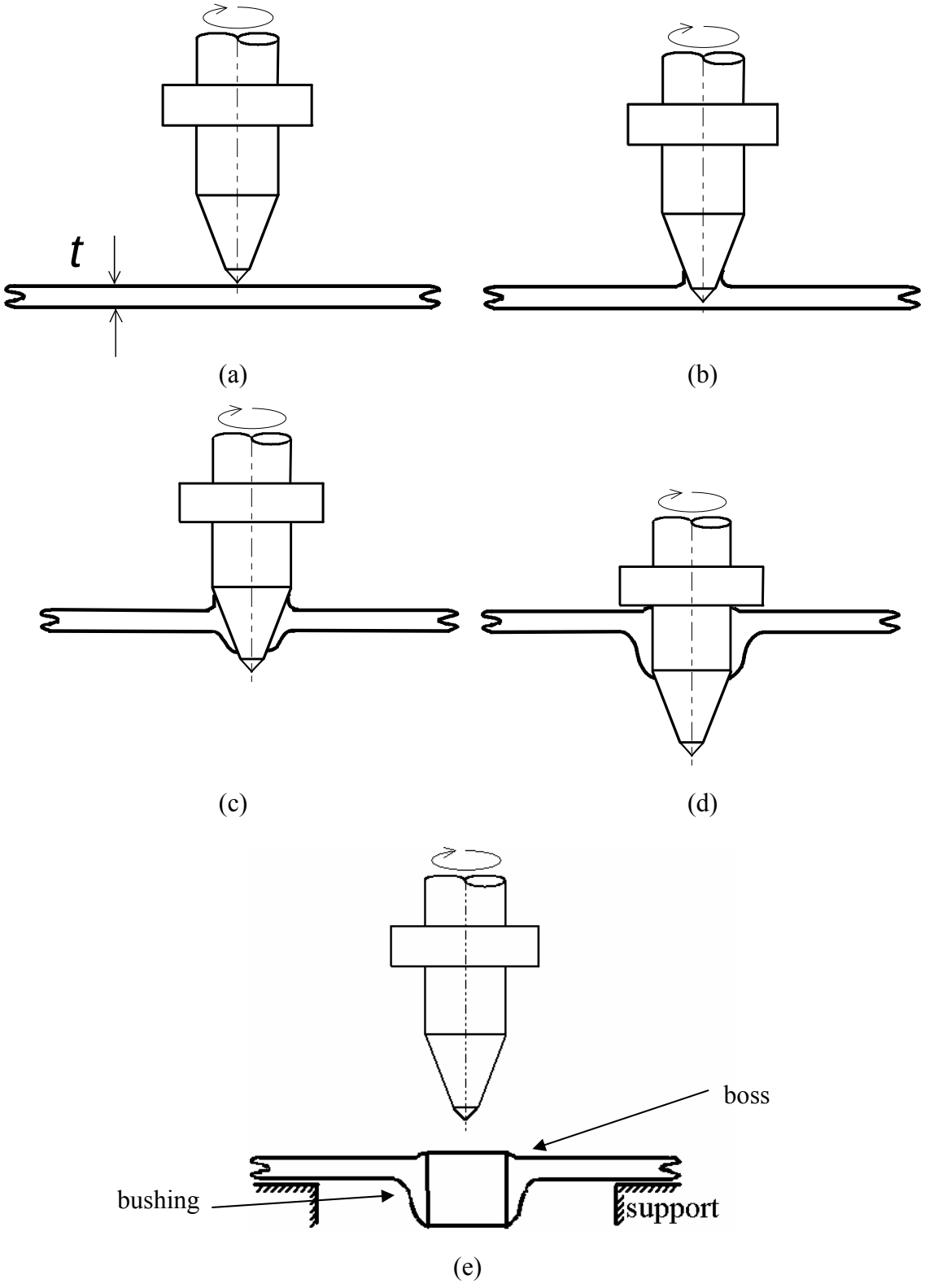


Figure 1.1. Illustration of stages in friction drilling process.

Figure 1.2. Resulting hole and bushing [19].

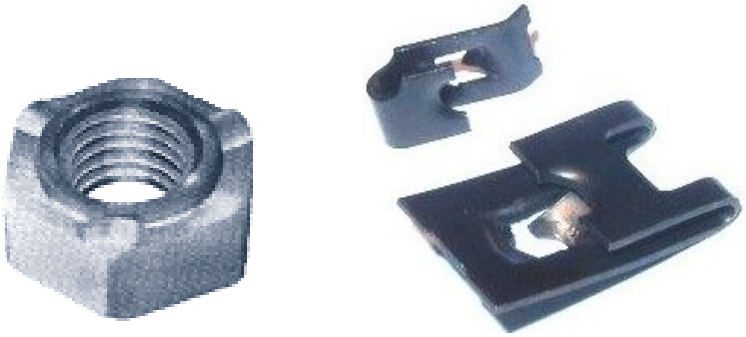

(a) (b)

Figure 1.3. (a) Weld nut and (b) J nut [20].

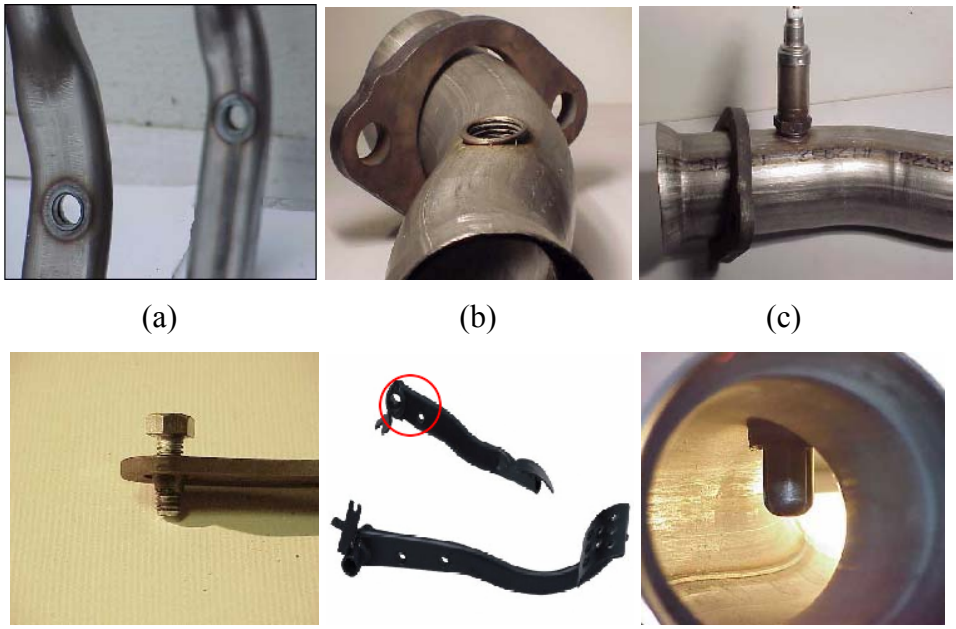


Figure 1.4. Automotive applications of friction drilling including (a) seat frame, (b) exhaust O2 sensor boss, (c) exhaust part, (d) seat handle, (e) foot pedal, and (f) oxygen sensor [19].

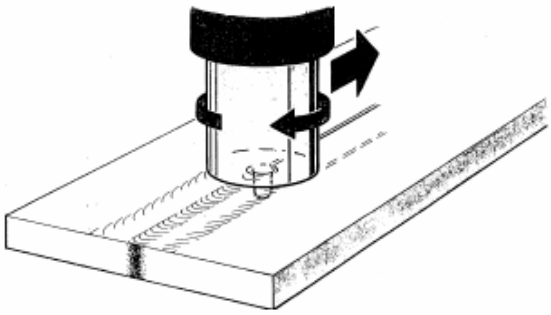

Figure 1.5. Schematic representation of friction stir welding [16].

Figure 1.6. Friction drilling cast Al part with flower shape bushing.

## References


[1] K.F.J. Ellwood, D. Fesko, and D.R. Bauer, An Axisymmetric Model for Thread Forming in Polycarbonate and Polypropylene Screw and Boss Fasteners, Polymer Engineering and Science 44 (8) (2004) 1498-1508.

[2] http://flowdrill.com/

[3] J.A. van Geffen, Piercing Tools, US Patent Number 3,939,683, 1976.

[4] J.A. van Geffen, Method and Apparatuses for Forming by Frictional Heat and Pressure Holes Surrounded Each by a Boss in a Metal Plate or the Wall of a Metal Tube, US Patent Number 4,175,413, 1979.

[5] J.A. van Geffen, Rotatable Piercing Tools for Forming Holes Surrounded Each by a Boss in Metal Plates or the Wall of Metal Tubes, US Patent Number 4,177,659, 1979.

[6] J.A. van Geffen, Rotatable Piercing Tools for Forming Bossed Holes, US Patent Number 4,185,486, 1980.

[7] G.D. Head, W.C. Le Master, L.P. Bredesky, and D.C. Winter, Flow Drilling Process and Tool Therefore, US Patent Number 4,428,214, 1984.

[8] A.J. Hoogenboom, Flow Drill for the Provision of Holes in Sheet Material, US Patent Number 4,454,741, 1984.

[9] J.E. France, J.B. Davidson, and P.A. Kirby, Strength and Rotational Stiffness of Simple Connections to Tubular Columns Using Flowdrill Connectors, Journal of Construction Steel Research 50 (1999) 15-34.

[10] J.E. France, J.B. Davidson, and P.A. Kirby, Moment-capacity and Rotational Stiffness of Endplate Connections to Concrete-filled Tubular Columns with Flowdrilled Connectors, Journal of Construction Steel Research 50 (1999) 35-48.

[11] J.E. France, J.B. Davidson, and P.A. Kirby, Strength and Rotational Response of Moment Connections to Tubular Columns Using Flowdrill Connectors, Journal of Construction Steel Research 50 (1999) 1-14.

[12] K. Overy, Flowdrilling – Bush Formation in Thin Metal, Chartered Mechanical Engineer 25 (7) (1978) 70-71.

[13] D. Bak, Friction, Heat from Integral Bushings, Design News 43 (11) (1987) 124.

[14] M. Kerkhofs, M.V. Stappen, M. D'Olieslaeger, C. Quaeyhaegens, and L.M. Stals, The Performance of (Ti,Al)N-coated Flowdrills, Surface and Coatings Technology 68/69 (1994) 741-746.

[15] W.M. Thomas, E.D. Nicholas, J.C. Needham, M.G. Murch, P. Temple-Smith, and C.J. Dawes, Friction stir butt welding, International Patent Application Number PCT/GB92/02203, 1991.

[16] J.E. Gould, T.J. Lienert, and Z. Feng, Recent Developments in Friction Stir Welding, Aerospace Manufacturing Technology Conference & Exposition, SAE Technical Paper Series 981875 (1998).

[17] D.F. Moore, Principles and Applications of Tribology, 1975, Pergamon Press Inc., New York.

[18] P.W. Bridgman, Effects of high hydrostatic pressure on the plastic properties of metals, Reviews of Modern Physics 17 (1) (1945) 3-14.

[19] http://www.danly-te.com

[20] http://www.wayneboltandnut.thomasregister.com

# CHAPTER 2.

# EXPERIMENTAL ANALYSIS OF THE FRICTION DRILLING PROCESS

## 2.1. Introduction

The mechanical and thermal aspects of friction drilling are studied in this section. The research on the mechanics of the friction drilling process, particularly the measurement of thrust force, torque, and temperature of the tool and workpiece, is lacking and has become the goal of this research. Similar studies have been performed for FSW. Chen and Kovacevic [1] measured the three components of force in FSW of an aluminum alloy. Soundararajan et al. [2] measured the vertical force during FSW for different rotational and traverse speeds of the tool. Song and Kovacevic [3] conducted temperature measurements with thermocouples at various distances from the welding centerline.

Under the constant tool feed rate, the experimentally measured thrust force and torque are analyzed. A non-contact infrared (IR) camera is applied to measure the tool and workpiece temperatures during friction drilling. A thermal finite element model is applied to predict the distance of tool travel to reach the threshold temperature after the initial contact.

The experimental setup and process parameters for friction drilling are first introduced in Sec. 2.2. In Sec. 2.3, the measured thrust force and torque are analyzed. The infrared camera for temperature measurement and its calibration are discussed in Sec. 2.4. The thermal finite element modeling is presented in Sec. 2.5 to predict the tool travel distance for the work-material to reach the 250ºC threshold temperature for infrared temperature measurement.

## 2.2. Experimental setup

### 2.2.1. Machine and workpiece

A three-axis computer numerical controlled vertical machining center, Milacron model Sabre with a 7.5 kW spindle, is used for the friction drilling experiment. The overview of the friction drill test setup is shown in Fig. 2.1(a). As shown in the close-up view in Fig. 2.1(b), the drill is fixed to a specially designed tool holder provided by Unimex Formdrill.

The workpiece is a 1.19 mm thick AISI 1020 cold-rolled carbon steel sheet. As shown in Fig. 2.1, the workpiece is held on top of a Kistler model 9272A piezoelectric drilling dynamometer. The thrust force and torque during drilling are measured. The experiment is carried out at 4000 rpm spindle speed and 165 mm/min constant tool feed speed.

### 2.2.2. Tool

The tool is made of WC in Co matrix. Key geometrical features of the drill are shown in Fig. 2.2. The drill consists of five regions:

1. Center region: The cone-shape center has the angle $\alpha$ and height $h_c$. The angle is usually blunt. The effect of blunting is to generate more force and, therefore, heat at the start of the drilling. The center region, like the web in a twist drill, provides the support in the radial direction for the friction drilling process and keeps the tool from walking at the start of the process.
2. Conical region: This region has a sharper angle than the center region. The drill in this region rubs against the workpiece to generate the friction force and heat and pushes the work-material sideward to shape the bushing. The angle and length of the cone-shape conical region are marked as $\beta$ and $h_n$, respectively.
3. Cylindrical region: This region helps to form the hole and shape of the bushing. The length and diameter of this region are designated as $h_l$ and $d$, respectively.
4. Shoulder region: The shoulder of this region may touch the workpiece to round the entry edge of the hole and bushing.
5. Shank region: This is the area of the tool gripped by the tool holder of the machine.

The first three regions (center, conical, and cylindrical) determine the thrust force and torque as well as the tool and workpiece temperatures during friction drilling. The tool geometry is important to the shape of the bushing and process performance. Dimensions of the friction drill used in this study has $d$ = 7.3 mm, $\alpha$ = 90°, $\beta$ = 36°, $h_c$ = 0.970 mm, $h_n$ = 8.490 mm, and $h_l$ = 8.896 mm.

## 2.3. Thrust force and torque in friction drilling

The measured thrust force and torque in friction drilling AISI 1020 steel are shown in Figs. 2.3(a) and 2.3(b), respectively. Under the constant feed speed, a peak thrust force of 700 N occurs at 2.5 mm of tool travel from the initial contact with the workpiece. This position of maximum thrust force is marked as A. A separate friction drilling test was conducted to stop and move back the tool at position A. The workpiece was sectioned and polished to reveal the deformation shape, as shown in Fig. 2.4(a). The sheet metal workpiece was bent and dented but not perforated. This reveals that the mechanical indentation of the workpiece by the tool tip is the key deformation mechanism at the start of friction drilling. Insufficient heat was generated to soften the work-material due to the low tool peripheral speed at the tip. No discoloration at the indentation of the workpiece was observed to confirm increased workpiece temperature. Low peripheral speed also accounted for the small torque in the beginning of the contact. The torque rapidly rose to 1.5 N-m after the tool reached position A.

The thrust force drops rapidly to 300 N, less than half of the peak value, after the tool moved by another 2 mm to position B, 4.5 mm tool travel from contact. Another separate friction drilling test was performed to stop the tool at position B. The deformation of the workpiece is shown in Fig. 2.4(b). The workpiece is on the verge of penetration by the tool tip. It indicates that, like the mechanics in conventional drilling [4], the center of the drill contributes a majority of the thrust force. Change in color was observed inside the hole due to the increased temperature. The torque increased to about 1.7 N-m at position B.

In the next 5.3 mm, the tool penetrates to position C (9.8 mm tool travel from the start of contact) close to the maximum torque condition. From position B to C, the thrust

force remains at about 300 N and the torque gradually increases to the maximum at 2 N-m. The deformation of the workpiece at tool position C is shown in Fig. 2.4(c). The conical region of the tool has perforated the workpiece and pushed the work-material aside to form a bushing. Rings of discoloration were observed inside and outside the hole, indicating the further increase of workpiece temperature. Between tool position C and D, both the force and torque start to decrease. Position D at 12.7 mm, as shown in Fig. 2.3, marks the end of friction drilling. The complete hole in friction drilling is shown in Fig. 2.4(d). After position D, the force is reduced to almost zero (or even negative) but torque remains high, in the 1.1 to 1.4 N-m range, while the tool retracts to leave the hole in the workpiece.

In summary, Fig. 2.3 illustrates a typical pattern of thrust force and torque for friction drilling at a constant tool feed rate. Partially filtered noise is present throughout the graphs in Fig. 2.3. The high peak force is not desirable since it deforms the sheet workpiece and may shorten the tool life.

## 2.4. Workpiece temperature measurement

A Raytheon Radiance IR camera system was used to measure the tool and workpiece temperature in friction drilling. The camera system was set up to capture temperature from a side view of drilling. The IR camera has an InSb focal plane array detector with a 256 by 256 pixels focal plane array. It is sensitive to thermal radiation wavelength from 3 to 5 μm. The IR imaging capturing was set at 60 frames/s with 0.1 ms integration time. The ND2 filter was used. The minimum detectable temperature by the IR camera system was 250ºC.

Figures 2.5(a) to 2.5(f) show three IR camera images of friction drilling at positions E, F, and D (the end of tool forward movement) and three IR frames when the tool is retracting from the workpiece. The intensity of a pixel in the image corresponds to the tool and workpiece temperature. The brightest spot with the highest intensity in Fig. 2.5(c) indicates the maximum temperature of the workpiece. Figures 2.5(e) and 2.5(f) show the heated tool exiting from the workpiece.

Because the thermal emissivity of the workpiece and tool material are not known, calibration tests are required to find relationship between the IR intensity and a known temperature. In calibration tests, the tool and workpiece were first heated in an oven that was equipped to measure and control temperature. During cooling the oven door was opened momentarily at different temperatures and the IR camera was used to record the thermal radiation intensity of an object (either the workpiece or tool) corresponding to the oven temperature reading. A calibration curve relating the IR intensity to workpiece temperature was generated, as shown in Fig. 2.6. It should be noted that there was enough time during the calibration procedure to change the camera setting to allow measurement of temperatures below 250ºC.

Using the workpiece intensity vs. temperature calibration curve, the maximum workpiece temperature in each IR frame could be obtained. The trendline equation in Fig. 2.6 was used to calculate workpiece temperature from IR intensity. Results are shown in Fig. 2.7. At the start, there is a time interval, $\Delta t$, needed for the workpiece to reach the 250ºC threshold temperature detectable by the IR camera. The tool travel during $\Delta t$ is designated as $\delta$. In the next section, a finite element thermal model is applied to predict $\Delta t$ and $\delta$.

The workpiece temperature gradually increases as the tool moves through the workpiece and displaces the work-material. As the bushing is formed, the workpiece temperature reaches a maximum value of 760°C at 3.2 s from the initial contact. The workpiece temperature then gradually decreases. The peak workpiece temperature is above the crystallization temperature, between 500 to 700°C, of AISI 1020 steel. Metallurgical studies show the grain size of the workpiece is refined near the friction drilled hole.

The tool temperature is difficult to measure since the workpiece material surrounds the tool during friction drilling. In Fig. 2.5(b), as the tool enters to the workpiece, the peak tool temperature is about 580°C. In Fig. 2.5(f), for the retracting tool, the tool is cooled and peak temperature is estimated at 400°C. A more dedicated experimental setup to aim at the tool tip once it just penetrates the workpiece is necessary to acquire a more accurate estimation of tool temperature.

## 2.5. Thermal finite element modeling to predict $\Delta t$ and $\delta$

The heat transfer at the start of the friction drilling process was modeled using the thermal finite element method to predict the time $\Delta t$ and distance $\delta$ of the tool travel for the workpiece to reach 250°C. The ANSYS 7.0 finite element software package and its mesh generator were applied. The finite element mesh, as shown in Fig. 2.8(a), consists of the eight-node, eight degree-of-freedom axisymmetric element to model a disk plate. The finite element mesh includes 4073 nodes. The initial contact and heat generation due to friction drilling occur at the top center of the cylindrical disk. The model is semi-empirical as the experimentally measured torque is used as an input for the heat flux. Deformation of the workpiece during friction drilling is not considered. The thickness of the plate is 1.2 mm, the same as the workpiece. The radius of the disk is 20 mm, large enough not to influence the temperature results near the center of the disk. Properties of the workpiece are assumed to be temperature-independent. The density is 7870 kg/m$^3$, the heat capacity is 486 J/kg-°C, and the thermal conductivity is 51.9 W/m-K. The initial temperature of the workpiece and the surrounding temperature are 25°C. The convection coefficient is set at 40 W/m$^2$-K.

Three time steps, designated as Steps I, II, and III, are used to simulate the heat transfer in friction drilling in the first 0.35 s. As shown in Figs. 2.8(b) to 2.8(d), $A_1$, $A_2$, and $A_3$ are the areas in Steps I, II, and III, respectively. Tool wear is not considered, i.e., a perfectly sharp tool is used to find the tool-workpiece interface areas.

Step I ranges from 0 to 0.118 s with 0.32 mm tool travel from the start of the tool contact. The interface between a perfectly shaped tool and the workpiece at the 0.32 mm tool travel is marked as $A_1$ in Fig. 2.8(b). $A_1$ represents a conical surface of the tool tip. A heat flux is applied on surface $A_1$ from 0 to 0.118 s. The heat flux, $q$, generated by friction is calculated by:

$$q = \frac{2\pi Tn}{60 A_i} a \tag{1}$$

where

$T$ is the experimentally measured torque,

$n$ is the rotational speed of the drill,

$A_i$ is the area of tool-workpiece interface, and

$a$ is the fraction of frictional energy converted into heat.

In the study, $n$ = 4000 rpm and $a$ = 0.9. The ramp-type heat flux, i.e., linearly increasing from zero heat flux at the start of contact to the $q$ at 0.118 s (end of Step I), is applied on the surface $A_1$. The experimentally measured torque at 0.118 s is used to calculate $q$ for Step I.

Step II ranges from 0.118 to 0.235 s when the tool tip travels from 0.32 to 0.65 mm. As shown in Fig. 2.8(c), the interface surface between the tool tip and the workpiece at the 0.65 mm tool travel is marked as $A_2$. The step-type heat flux, i.e., uniform from 0.118 to 0.235 s, is applied. The torque $T$ at 0.235 s is used to calculate $q$ for Step II.

Step III ranges from 0.235 to 0.35 s. The tool tip travels from 0.65 to 0.97 mm into the workpiece. The step-type heat flux with torque $T$ at 0.35 s is applied.

Results of the maximum surface temperature of the workpiece vs. time obtained from the thermal finite element modeling are shown in Fig. 2.9. The temperature gradually arises from 25 to 500ºC in about 1 s. The temperature reaches 250ºC at $\Delta t$ = 0.075 s and $\delta$ = 0.21 mm. The experimentally measured temperature starting from 250ºC is plotted in Fig. 2.9. Beyond 250ºC, the trend of temperature rising obtained from experiment and simulation match. This validates the finite element estimation of $\Delta t$ and $\delta$.

## 2.6. Conclusions

Experimental analysis of the friction drilling process identified different drilling stages in the process. The center region of the tool generated a peak in thrust force early in the friction drilling process, causing large workpiece deflection. Temperature increased rapidly in this stage. As the tool penetrated further, thrust force decreased in the softened work-material. The conical region of the tool engaged the workpiece to force work-material radially to form the bushing. As the work-material encompassed the conical region of the tool, thrust force stabilized to a near constant value and torque and

workpiece temperature reached maximum values. In the final stage, thrust force, torque, and temperature all tapered as the cylindrical region of the tool contacted the workpiece.

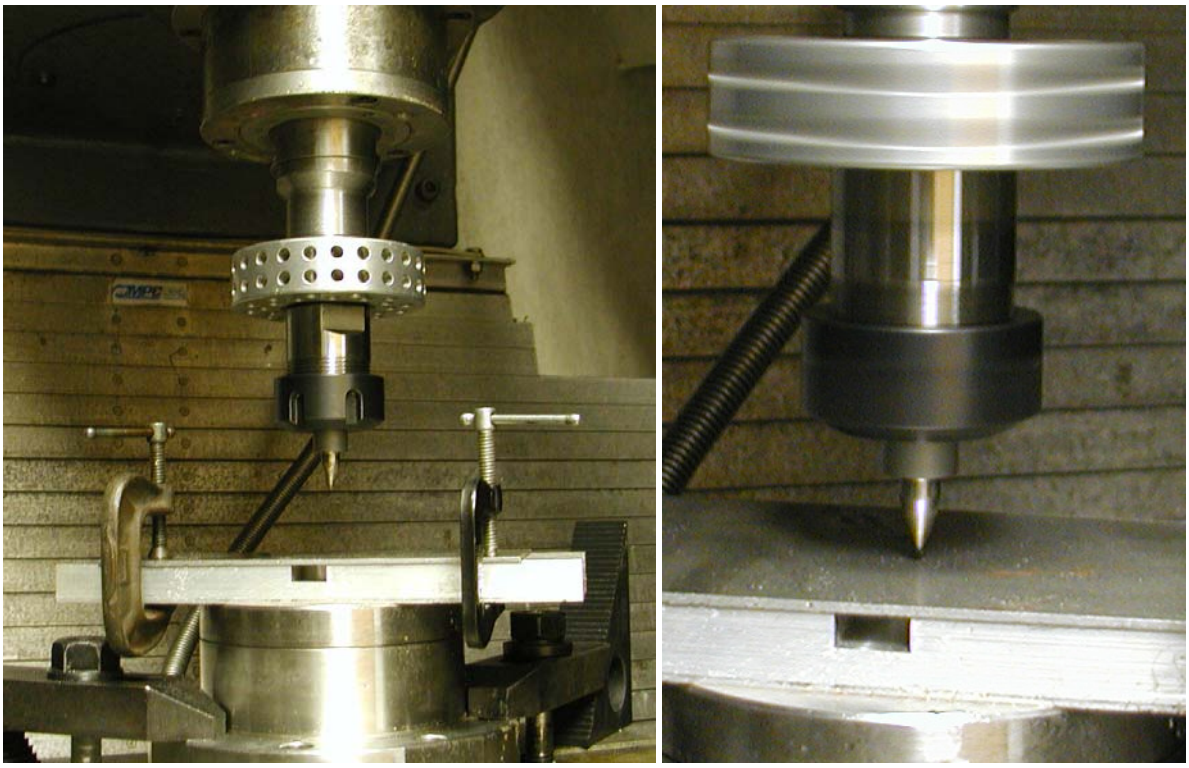

(a) (b)

Figure 2.1. Experimental setup in friction drilling: (a) overview and (b) close-up view of the spinning tool contacting the workpiece.

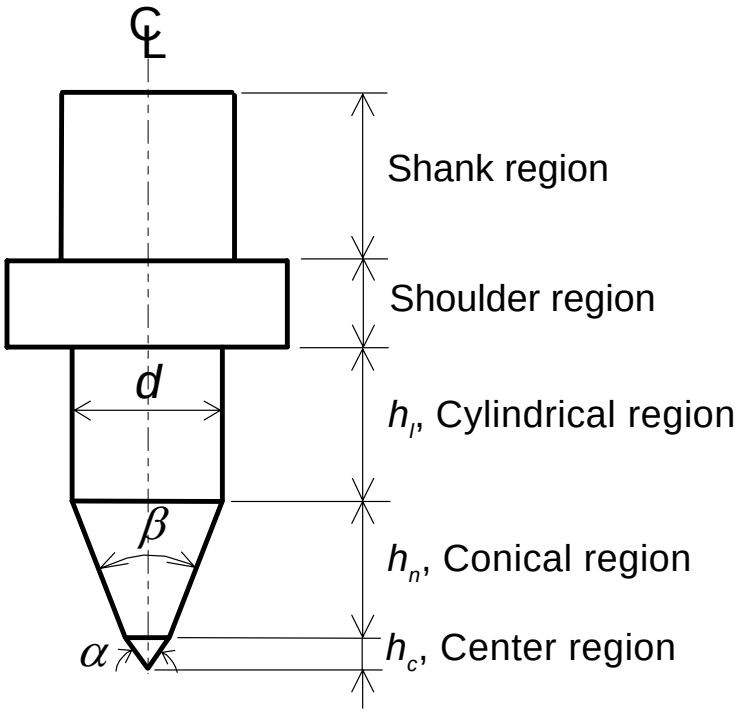


Figure 2.2. Key dimensions of the friction drilling tool.

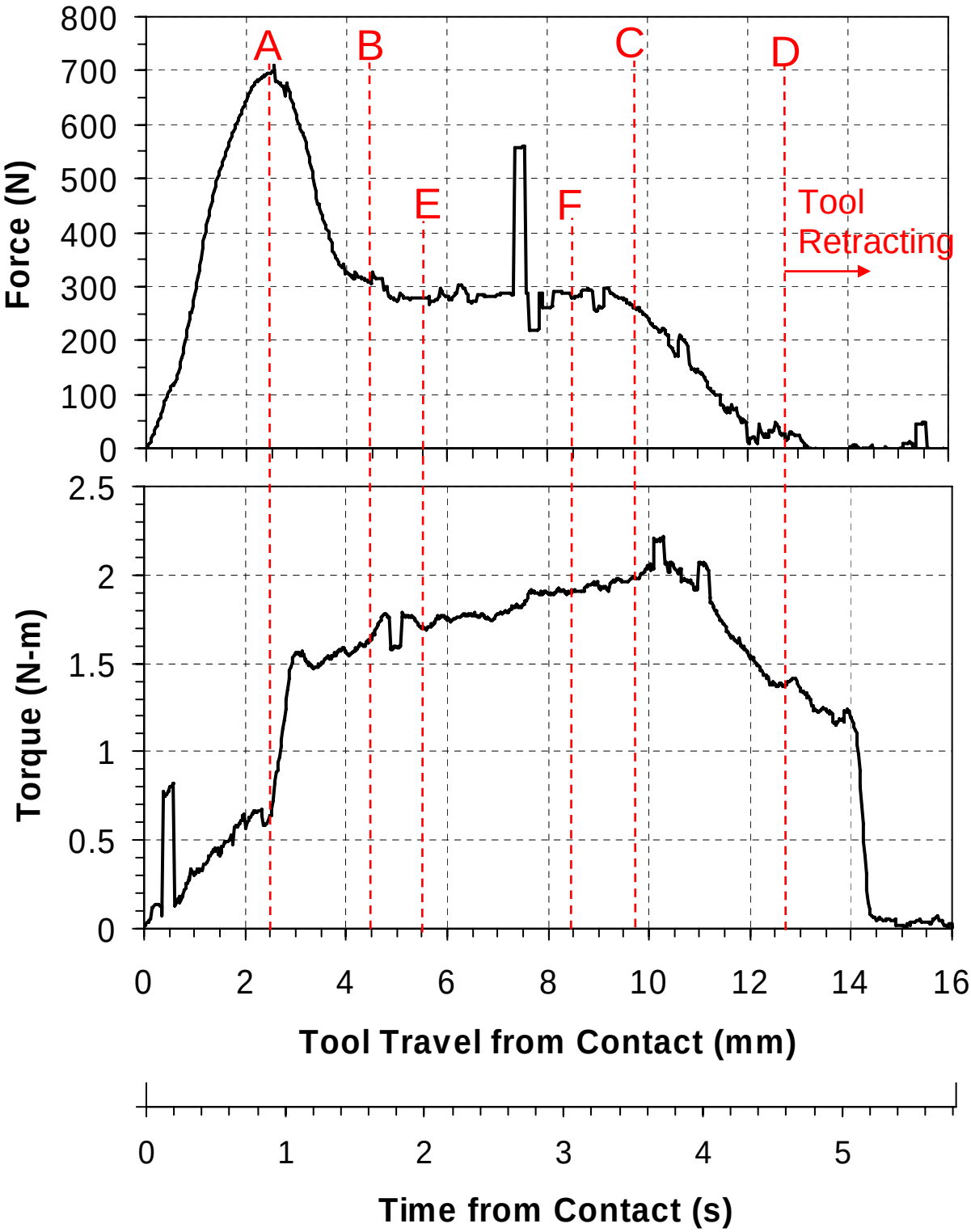


Figure 2.3. Thrust force and torque in friction drilling of AISI 1020 carbon steel sheet.

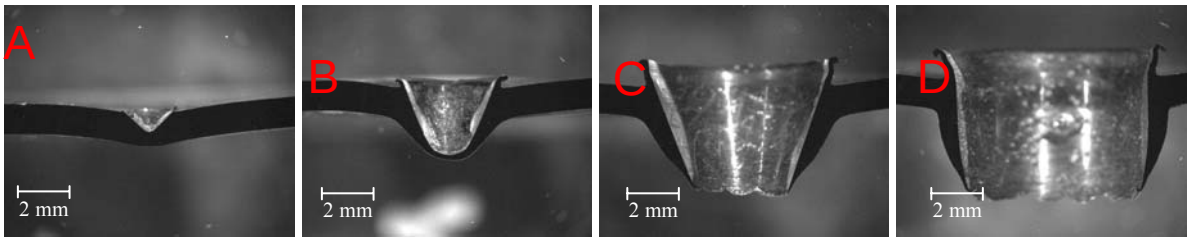


(a) (b) (c) (d)

Figure 2.4. Cross sectional view of deformation of the workpiece in friction drilling at positions (a) A, (b) B, (c) C, and (d) D in Fig. 2.3.

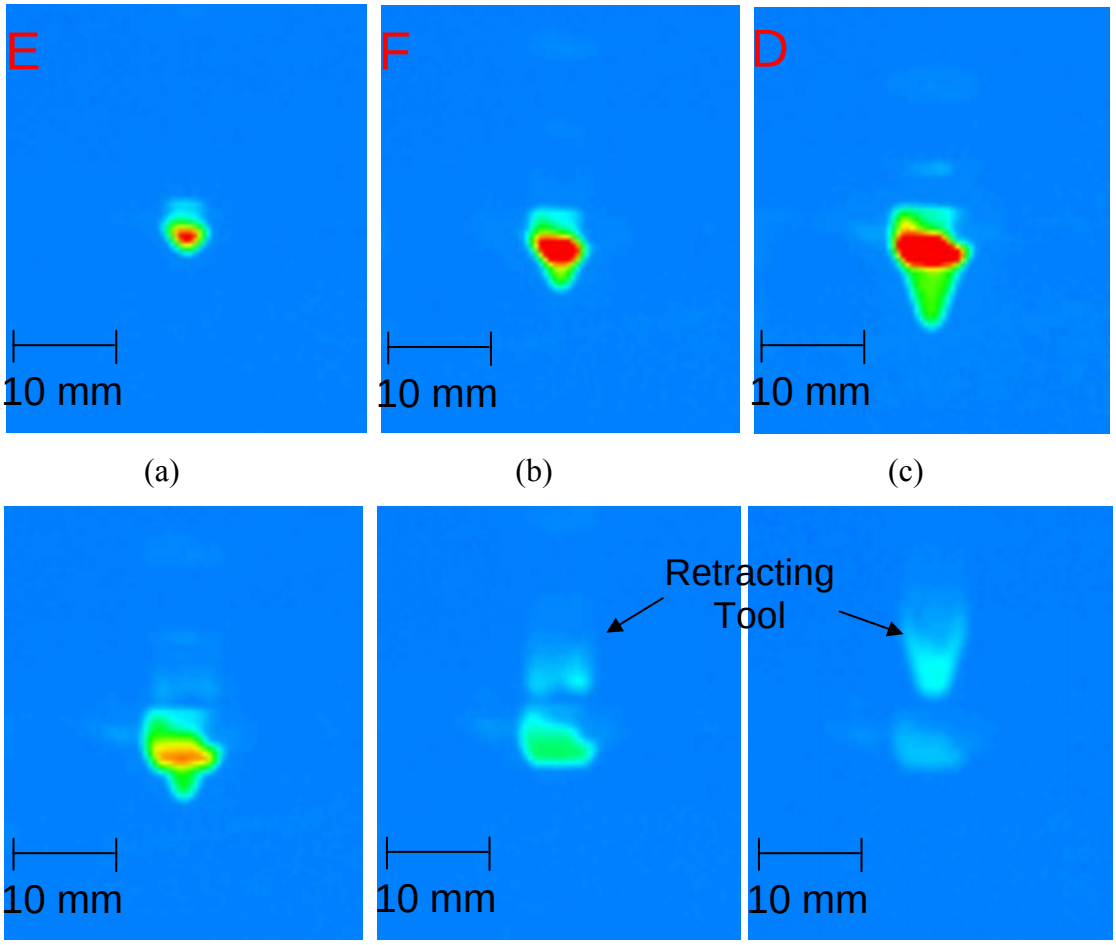


(a) (b) (c)

(d) (e) (f)

Figure 2.5. Infrared camera pictures of friction drilling: (a) 2 s, (b) 3 s, (c) 5 s, (d) 8.5 s, (e) 10 s, and (f) 12 s from the contact of the tool and workpiece.

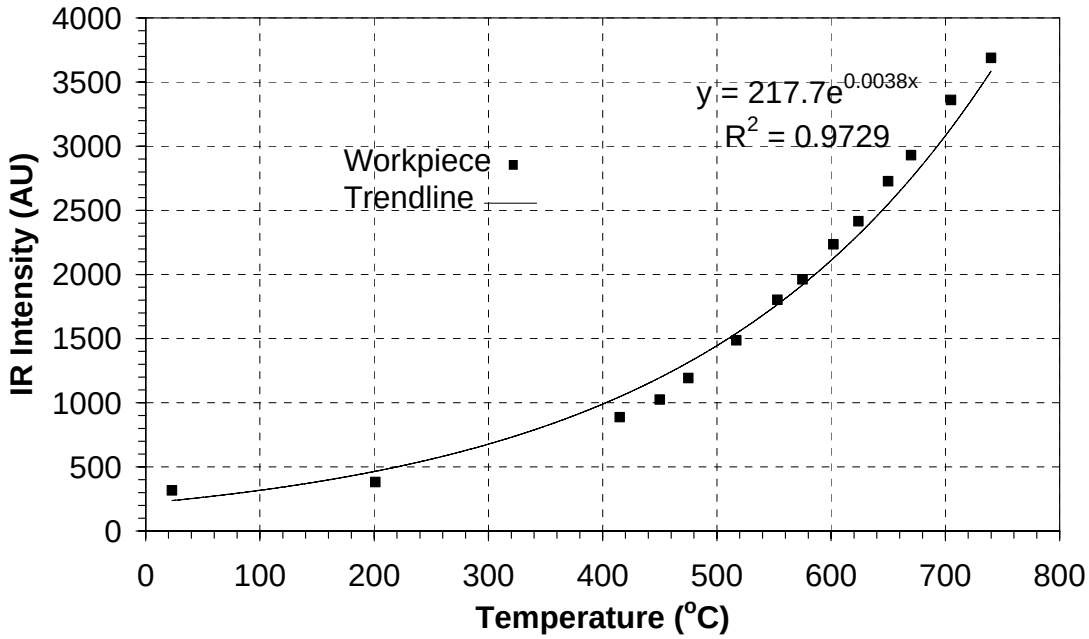


Figure 2.6. Calibration curve relating the IR intensity to workpiece temperature

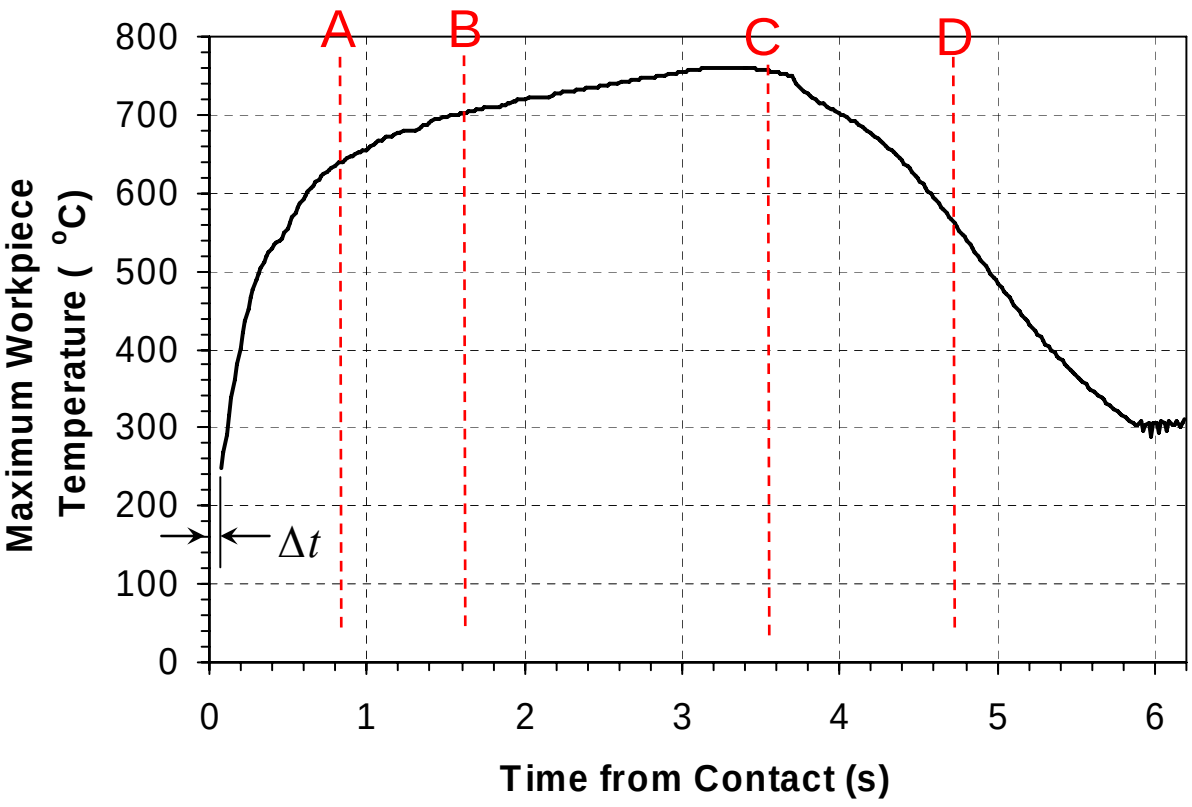


Figure 2.7. Maximum workpiece temperature and the minimum temperature detectable by the infrared camera.

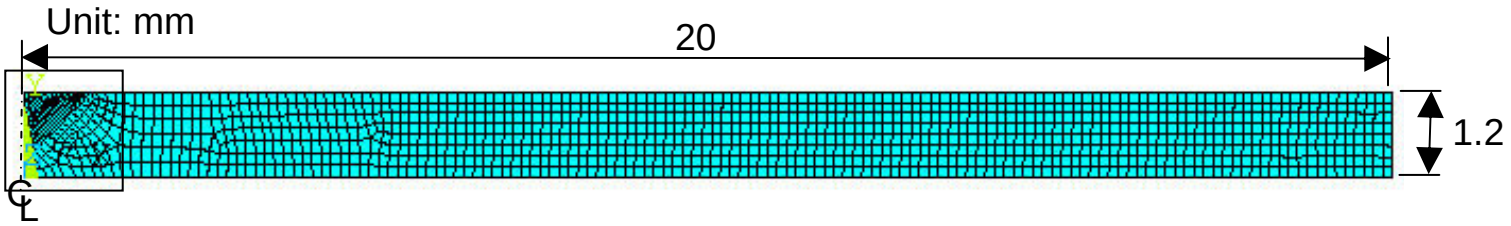


(a) Initial mesh

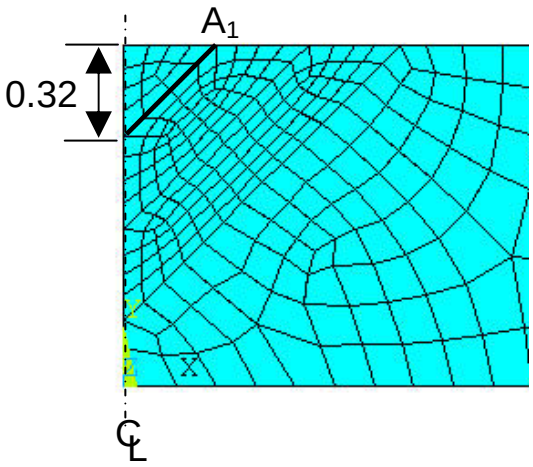


(b) Time Step I

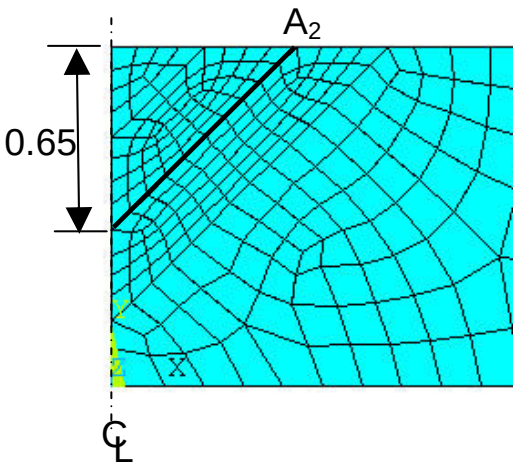


(c) Time Step II

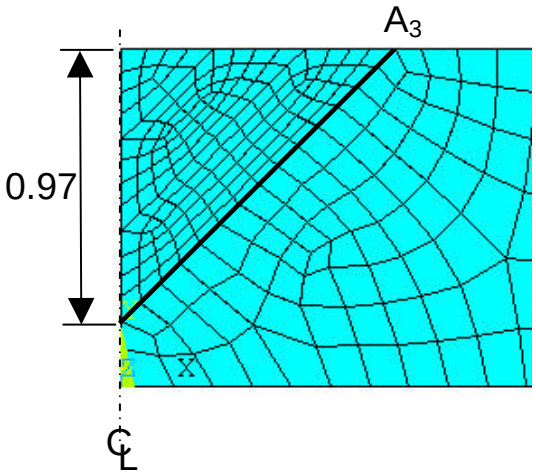


(d) Time Step III

Figure 2.8. The axisymmetric finite element mesh and the thermal model at three time steps.

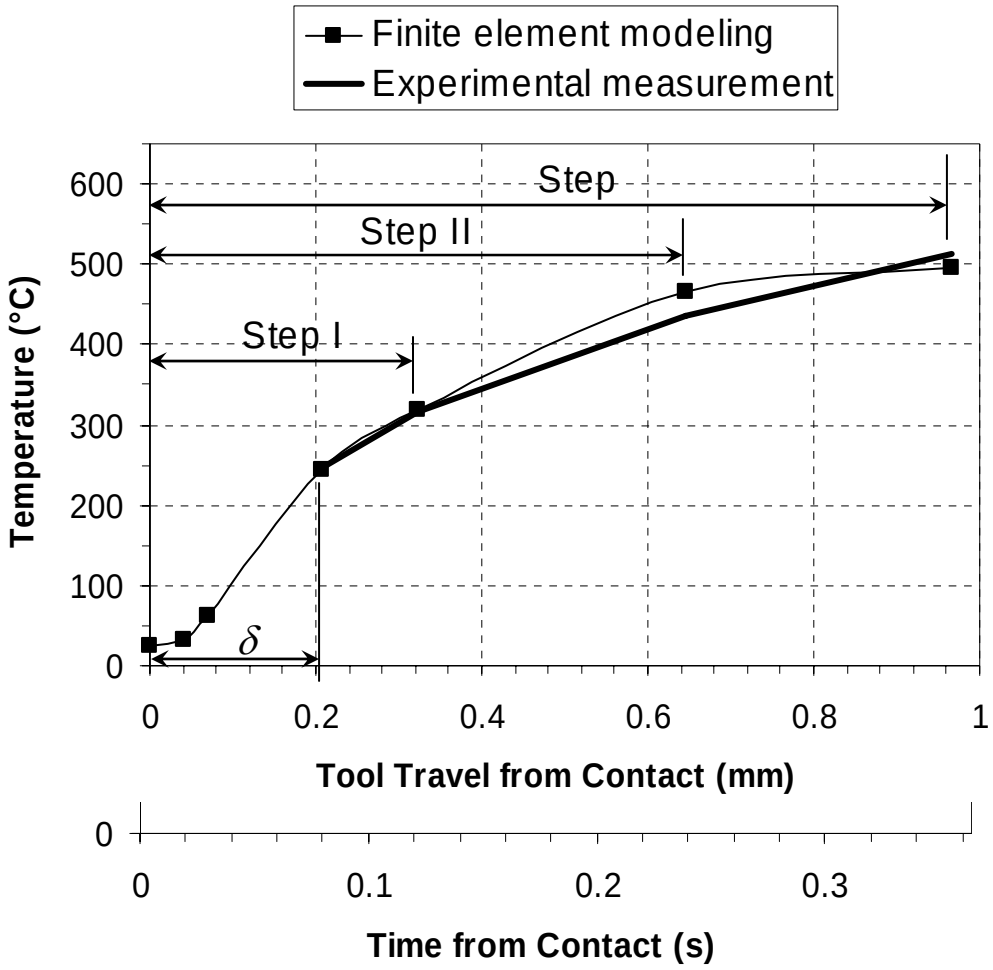


Figure 2.9. Comparison between the experimental and thermal modeling temperature.

## References


[1] C. Chen and R. Kovacevic, Thermomechanical modeling and force analysis of friction stir welding by the finite element method, Proc. Instn Mech. Engrs 218 (C) (2004) 509-519.

[2] V. Soundararajan, S. Zekovic, and R. Kovacevic, Thermo-mechanical model with adaptive boundary conditions for friction stir welding of Al 6061, International Journal of Machine Tools & Manufacture 45 (2005) 1577-1587.

[3] M. Song and R. Kovacevic, Numerical and experimental study of the heat transfer process in friction stir welding, Proc. Instn Mech. Engrs 217 (B) (2003) 73-85.

[4] J.S. Strenkowski, C.C. Hsieh, and A.J. Shih, An Analytical Finite Element Technique for Predicting Thrust Force and Torque in Drilling, International Journal of Machine Tools and Manufacture 44 (2004) 1413-1421.

# CHAPTER 3.

# MICROSTRUCTURAL ALTERATIONS ASSOCIATED WITH FRICTION DRILLING OF STEEL, ALUMINUM, AND TITANIUM

## 3.1. Introduction

High temperature and strain in friction drilling change material properties and microstructures. These consequences, although often unwanted in machining, are both unavoidable and important to the quality of friction drilled holes. The development of microstructures is affected by the material flow and heating that occurs during friction drilling.

Previous research has been conducted to characterize effect of FSW on microstructure and material properties. Reis et al. [1] studied the effects of FSW on microstructure and hardening in an aluminum alloy. Guerra et al. [2] presented results of flow patterns in FSW with a surface tracer. Fonda et al. [3] studied the development of grain structure and texture around the FSW tool. Other researchers have reported microstructural changes caused by FSW for steel [4] and titanium [5]. However, no study has been conducted to investigate the changes to microstructures and material properties of the work-material which is subjected to the large deformation and high temperature in friction drilling.

The present work focuses on the microstructural alterations and subsurface micro-indentation hardness changes produced as a result of the friction drilling process of AISI 1020 and 4130 steel, Al 5052, and commercially pure (CP) titanium. Effects of temperature and plastic strain in friction drilling are investigated.

## 3.2. Experimental setup

### 3.2.1. Materials

The tool used was a proprietary Co-bonded WC product supplied by Formdrill. The tool geometry is important to the shape of the bushing and process performance. The friction drill used in this experiment has an outer diameter of 5.3 mm and the height of the conical region is 6.35 mm.

The four workpiece materials chosen were AISI 4130 and 1020 steel, aluminum alloy 5052-H32, and Grade 2 CP titanium. The AISI 1020 steel was selected as the baseline. This was used in the experiments described in Chapter 2. The AISI 4130 steel, with added alloying elements and different material properties, was chosen for comparison. The aluminum alloy 5052-H32, which is used in the automotive industry, was suggested for this study due to potential applications with friction drilling. Grade 2 CP titanium was chosen because of its increased use in industry and high temperatures (>1000°C) were measured in friction drilling of this material due to its low thermal conductivity. The thickness and mechanical and thermal properties of the work-materials used in this study are listed in Table 3.1. Table 3.2 summarizes the chemical composition of the steel and aluminum alloy work-materials.

### 3.2.2. Drilling parameters

A Vetrax vertical mill was used for friction drilling tests. The thrust force could be more accurately maintained constant with manual operation than using a constant feed rate in a conventional CNC machine, which generates high peak force as described by Miller et al. [6] in Chapter 2. This method helped to minimize denting the sheet metal workpiece and to improve the bushing quality. The fixturing and instrumentation for drilling is the same as in Chapter 2.

The spindle speeds used for sheet material of AISI 4130 steel, 1020 steel, CP Ti, and Al 5052 were 2800, 2800, 1000, and 3600 rpm, respectively. These were determined experimentally to enable the penetration and forming of the hole. For titanium, with low thermal conductivity, most of the frictional heat is retained in the tool-workpiece interface. The effect of frictional heating is relatively prominent. This causes excessive temperatures in the workpiece and results in undesired material damage and improper

bushing formation. For the aluminum alloy, the thermal conductivity is high. A large portion of the frictional heat is transferred into the workpiece and the effect of friction heating is relatively small. Low temperature causes insufficient increase in ductility and softening, resulting in high thrust force, denting of the workpiece, and improper bushing formation. These effects dictated the selection of low and high spindle speed for titanium and aluminum, respectively. These settings, while satisfactory for the present studies, do not necessarily represent the optimal drilling conditions that might be employed in a production environment.

A specimen of each workpiece material was prepared for examination. A friction drilled hole was cut from the workpiece sheet metal. Each was mounted in a metallographic mount by epoxy potting, then rough ground to the hole cross-section, and then polished with progressively finer diamond compounds. This preparation facilitated examination by optical microscopy and hardness testing by a Buehler microhardness tester. The Knoop indenter under 0.245 N load was used for micro-hardness indentation tests. The elongated impressions of the Knoop hardness test enables closer spacing within the deformed regions. After optical microscopy and hardness testing, the specimens were chemically etched for microstructural observation. Chemical etchants were applied to reveal the grain boundary and observe the large plastic deformation of work-material, particularly the surface layer, on friction drilled holes [7].

### 3.3. Microstructure observations and discussion

Figures 3.1(a)–(d) shows low magnification, optical views of the polished cross-sections of the four work-materials. Differences in the material displacement are evident as is the shape of bushing, bore surface quality, and denting of workpiece. Table 3.3 summarizes macroscopic measurements of holes and shape of bushings that were produced by friction drilling. The steels had relatively smooth bore finishes, as shown in Figs. 3.1(a) and (b). But the aluminum (Fig. 3.1(c)) and titanium (Fig. 3.1(d)) holes show severe tearing and scoring on the hole surface. The light colored deposit in the titanium hole is residue from the drilling lubricant. Bubbles apparent in Fig. 3.1 exist in the mounting epoxy and are not relevant in the cross-section samples. The photomicrographs

that follow show planes of polish parallel to the cross-sectional view as shown in Fig. 3.1 or from a top view parallel to the original sheet. Since non-ferrous work-materials responded differently to friction drilling than the steels, these will be discussed in separate sections.

### 3.3.1. AISI 1020 and 4130 steels

Friction drilled holes in AISI 1020 and 4130 steel were relatively uniform in shape and exhibited a smooth bore surface finish. No material transfer was noticed for friction drilling of these ductile materials. Figure 3.2(a) shows box A in Fig. 3.1(a), the subsurface microstructure adjacent to the hole bore in AISI 1020 steel. A region of relatively fine-grained, equi-axed grains extend approximately 60 μm radially from the hole surface, marked by J. These grains appear to be 1 μm or less in diameter. Inside this subsurface region, a larger region of elongated grains is visible.

Figure 3.2(b) shows a hole in AISI 1020 steel, but with the plane of polish parallel to the plane of the sheet in the bushing, as shown by line B-B in Fig. 3.1(a). It shows the similar, microstructurally deformed area, marked by K, and a surface texture that suggests the tool rotational direction (the surface was frictionally sheared from the left to the right in the photomicrograph).

Knoop microindentation (the indentation load was 0.245 N) subsurface hardness profiles comparing the AISI 1020 with that of AISI 4130 steel is shown in Fig. 3.3. The base material hardness is marked by the dashed red lines. The zone of high hardness due to the severe plastic deformation for AISI 1020 appears to extend 1200 μm below the surface, while that for AISI 4130 drops off more steeply at about 100 μm below the surface. The AISI 4130, as expected, has higher hardness values. Hardening also occurred on the upset portion of the boss region, indicated as box C in Fig. 3.1(a). Figure 3.4 shows the microstructural texturing in this zone on AISI 1020 steel. The indentation hardness of this upset region was 3.01 GPa, but that of the drawn out tip at the bottom end of the hole was less, about 2.29 GPa. Both hardness values in the boss region are higher than that of the sheet well away from the hole (about 1.46 GPa).

The microstructure of the AISI 4130 steel adjacent to the hole, marked as line D-D in Fig. 3.1(b), is shown in Fig. 3.5. Compared to the same region of AISI 1020 in Fig.

3.2(b), the highly-strained, white-etching surface layers and overlapping surface texture are evident in the bore of the drilled hole of AISI 4130 steel. Surface tractions and localized shear strains apparently produced a fine series of parallel lamellae. The serrated appearance of the cross-section is suggestive of ductile tearing.

### 3.3.2. 5052 Al

Damage to the interior surface of the friction-drilled hole in Al 5052 sheet is evident in Fig. 3.6. Severe scoring and plastic deformation with surface delamination are present. Figure 3.7(a), marked as box E on the cross-section in Fig. 3.1(c), exhibits thin platelets of aluminum that were removed, leaving some regions with microcracking below the deformed layers. The tendency of aluminum adhering to metalworking and machining tools is commonly known [8]. The tremendous pressure and the high temperature generated by the process will ‘‘weld’’ the two active surfaces together. If the bonding energy of the ‘‘weld’’ is stronger than the cohesive energy of the workpiece materials, then workpiece adhesion may be formed on the tool [9]. This is once more demonstrated in the case of friction drilling.

Figure 3.7(b) shows microstructure of the area in the bushing with the cross-section parallel to the plane of the sheet, marked as line F-F in Fig. 3.1(c). Compared with the white-etching layers seen in AISI 4130 steel in Fig. 3.5, Fig. 3.7(b) shows much less obvious development of a discontinuous zone of near-surface deformation adjacent to the bore surface.

### 3.3.3. CP Ti

CP titanium was the most difficult of the four materials to friction drill. The shape of the bushing in friction drilled CP titanium, as shown in Fig. 3.1(d), is short and thick, compared with bushings of other work-materials in Fig. 3.1. This is also evident in the quantitatively measured bushing height and diameter summarized in Table 3.3. It was necessary to reduce the tool rotational speed and introduce a commercial lubricant (Form Drill™ FD-KSO-2) to enable the hole and bushing to be formed properly. Despite the use of reduced speeds and drilling lubricant, the internal surface of friction drilled CP titanium holes, as shown in Fig. 3.8, was damaged to an even greater extent than that of

aluminum (Fig. 3.6). Close-up views of two areas along the hole, marked by boxes G and H in Fig. 3.1(d), are shown in Figs. 3.9(a) and 3.9(b), respectively. The wall consisted of either layers or localized pockets of severely deformed work-material.

Figure 3.10 shows the cross-sectional view parallel to the titanium sheet, marked by line I-I in Fig. 3.1(d), of the friction drilled hole in the bushing. The flow of material from left to right and a cluster of cracks, marked by L and about 20 μm long, can be identified near the tip of the large crack of the torn surface layer (about 50 μm thick). This cluster of cracks is likely generated by the stress concentration at the interface of delaminating surface layers. Another cluster of very fine micro-cracks, marked by M and about 5 to 8 μm long, occurs at the interface between the deformed surface layer and the base material. These cracks could be induced possibly by thermal stress due to the high temperature gradient on the Ti surface layers during friction drilling.

Figure 3.11 compares the subsurface Knoop hardness versus depth profiles of the aluminum and titanium sheet. The base material hardness is marked by the dashed red lines. For titanium, the highly-deformed swirled regions, like those shown in Fig. 3.9 had Knoop micro-indentation hardness values ranging from about 2.6 to 3.5 GPa, while the granular regions just below the swirled region had hardness values of about 2.2 GPa. For aluminum the reduction of hardness is gradual and shallow (less than 100 μm) into the workpiece.

## 3.4. Conclusions

Friction drilling of sheet metal results in a highly-sheared microstructure in the vicinity of the hole bores and in the material extruded above and below the plane of the original sheet stock. The grain boundaries were reoriented according to flow of work-material into the extrusions. The shear deformation zone, marked by reduction in grain size, was more distinct in the steel materials.

A region of increased hardness near the hole wall was noticable in all materials, caused by strain hardening and grain size reduction. The hardening of the hole wall implies a stronger connection can be formed with a friction drilled hole. For the AISI 4130 steel and 5052 aluminum points of softened material underneath the shear

deformation zone were observed, believed to be from thermal effects. Large strain and temperature experienced by the work-material caused changes in hardness, although the contribution of each is difficult to quantify.

Friction drilled holes in the steel materials had a smooth, polished surface finish. Hole surfaces in aluminum and titanium were damaged and cracked for different reasons. The softer aluminum forms strong intermetallic bonds with the tool material and adheres to the tool, causing tearing and cracks inside the work-material. The low thermal conductivity of the titanium workpiece caused the heat to localize in a thin surface layer on the inside wall of the hole. The titanium exhibited a molten state from excessive temperature in this surface layer, resulting in severe damage and tearing, which compromised the surface quality of the hole.

Recrystallization of the work-material was not observed because of the short time period of high temperature. There is no direct microstructural evidence for melting of work-material in friction drilling. It is entirely possible, however, that a very small amount of melting occurred at some thin surface regions.

Table 3.1. Materials used in friction drilling studies

| Material | Sheet thickness (mm) | Knoop hardness (0.245 N load) (GPa) | Thermal conductivity (W/m-K)* | Heat capacity (J/kg-K)** | Density ($kg/m^3$)*** |
|---|---|---|---|---|---|
| AISI 1020 steel | 1.56 | 1.46 | 50.2 | 481 | 7850 |
| AISI 4130 steel | 1.43 | 3.11 | 41.2 | 477 | 7845**** |
| Al 5052 | 1.62 | 0.60 | 138 | 880 | 2657 |
| Commercially pure Ti | 1.59 | 1.80 | 16.4 | 519 | 4540 |
| WC/Co (tool) | -- | 18.4 | 84 | 240 | 15000 |

*Values at room temperature from [10]
**Values at room temperature from [11]
***Values at room temperature from [12]
****Values at room temperature from [13]

Table 3.2. Composition of as received sheet metal by wt. % [14]

| Element | AISI 1020 steel | AISI 4130 steel | Al 5052-H32 |
|---|---|---|---|
| Al | | | 95.7-97.7 |
| C | 0.17-0.23 | 0.28-0.33 | |
| Cr | | 0.8-1.1 | 0.15-0.35 |
| Cu | | | Max 0.1 |
| Fe | 99.08-99.53 | 97.3-98.22 | Max 0.4 |
| Mg | | | 2.2-2.8 |
| Mn | 0.3-0.6 | 0.4-0.6 | Max 0.1 |
| Si | | 0.15-0.35 | Max 0.25 |
| Zn | | | Max 0.1 |
| P | Max 0.04 | Max 0.035 | |
| S | Max 0.05 | Max 0.04 | |
| Mo | | 0.15-0.25 | |

Table 3.3. Macroscopic measurements of hole characteristics

| Material | Hole diameter (mm) | Avg. boss extruded height above the sheet (mm) | Avg. bushing height below the sheet (mm) | Diameter of the base of the bushing (mm) |
|---|---|---|---|---|
| AISI 1020 Steel | 5.22 | 0.38 | 2.96 | 4.83 |
| AISI 4130 Steel | 5.28 | 0.51 | 4.12 | 5.28 |
| Al 5052 | 5.24 | 0.42 | 4.14 | 5.30 |
| CP Ti | 5.19 | 0.32 | 2.83 | 4.87 |

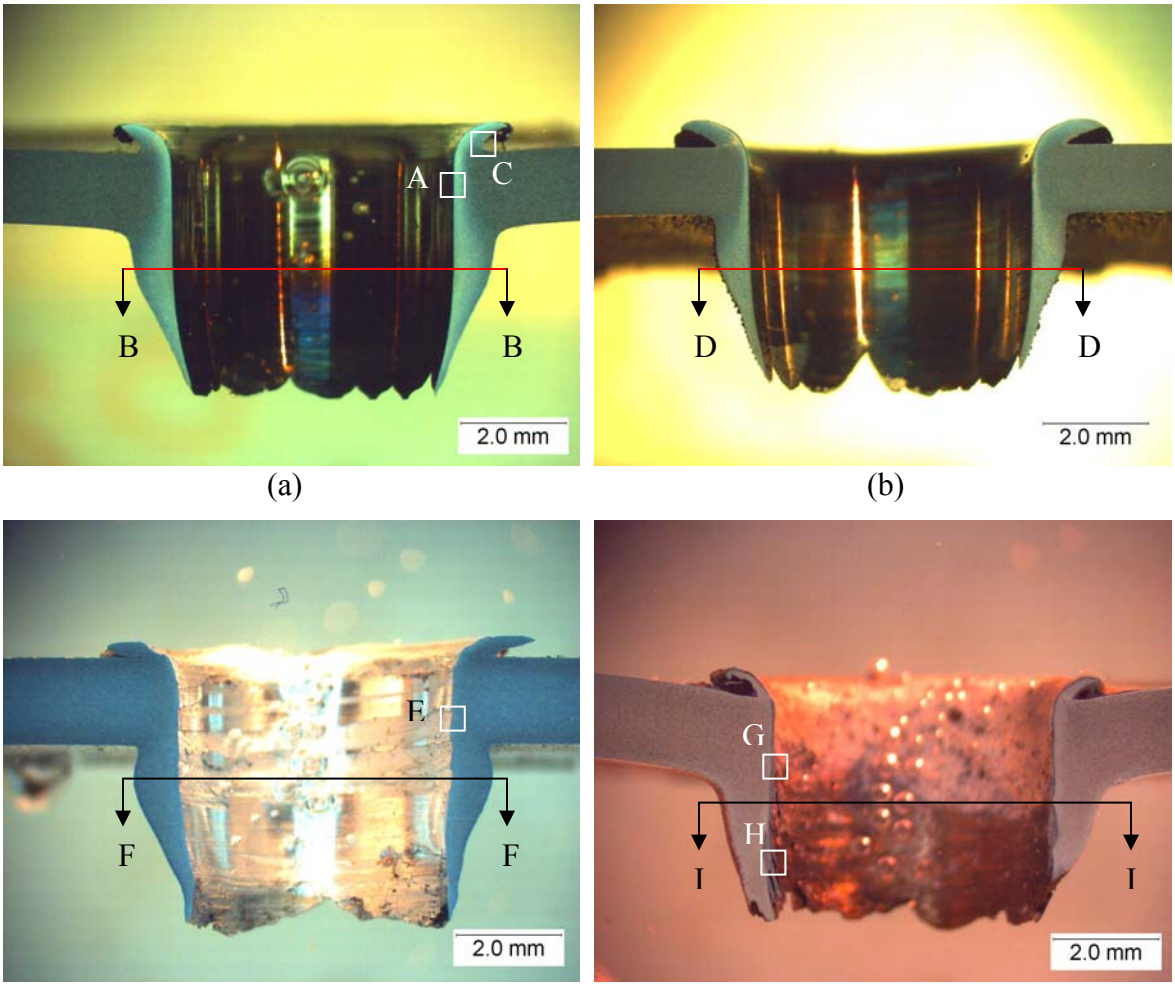


(a) (b)

(c) (d)

Figure 3.1. Cross-sections of friction-drilled holes in: (a) AISI 1020 steel, (b) AISI 4130 steel, (c) Al 5052, and (d) CP Ti. (Bubbles in (a), (c), and (d) are the mounting medium and should be ignored.)

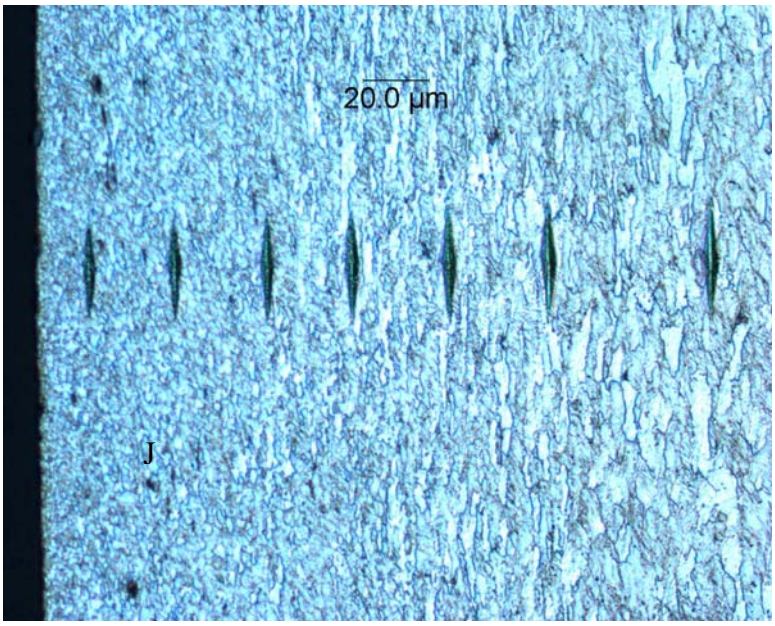


(a)

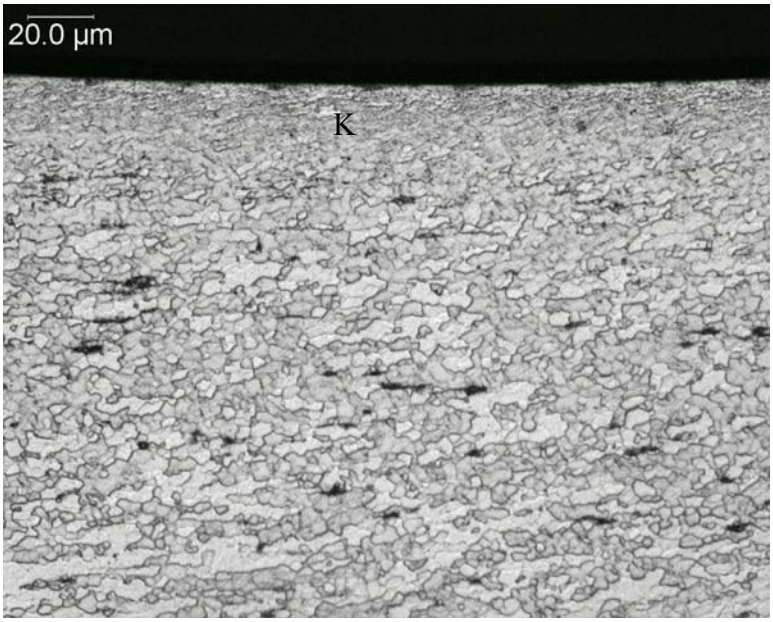


(b)

Figure 3.2. (a) Close-up view of box A in Fig. 3.1(a), shear deformation zone adjacent to the cylindrical portion of the hole in AISI 1020 steel showing a row of Knoop hardness impressions (etched in 2% nital) and (b) cross-sectional view of line B-B in Fig. 3.1(a) (same etchant as in Fig. 3.2(a)).

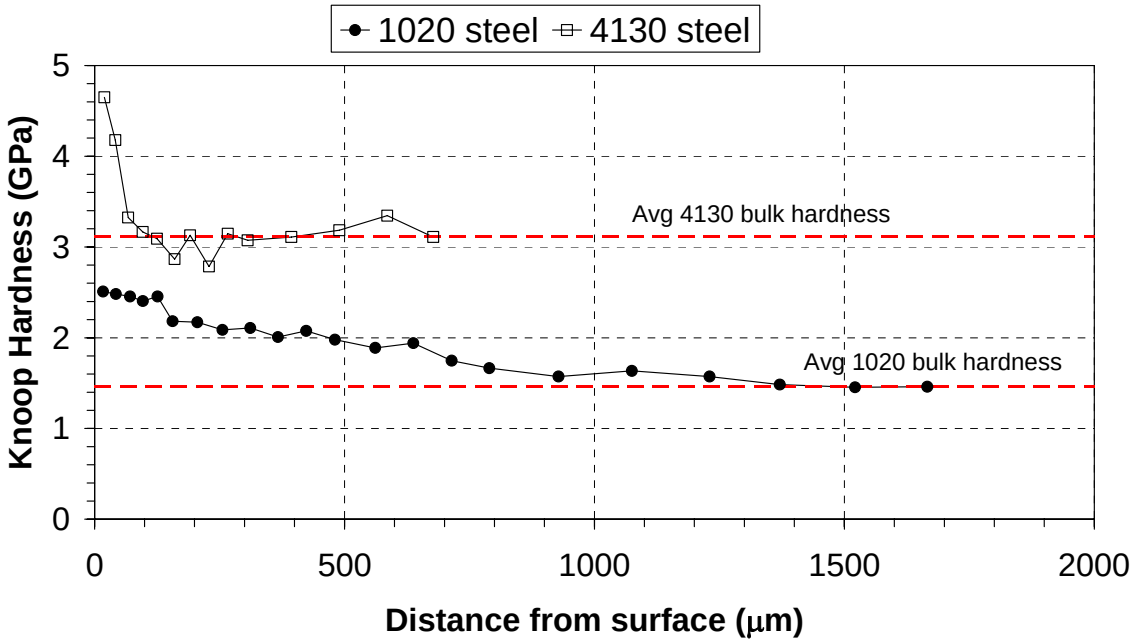


Figure 3.3. Microindentation hardness profiles of subsurface in friction drilled AISI 1020 and 4130 steel workpiece (0.245 N force used).

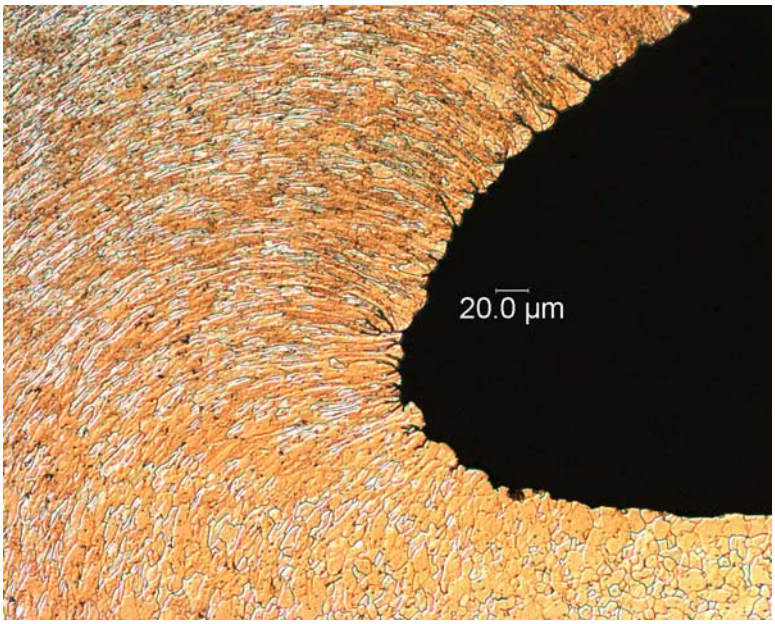


Figure 3.4. Close-up of box C in the boss region of AISI 1020 in Fig. 3.1(a) showing extreme plastic flow in the region underneath the lip of upset material at the tool-entry side.

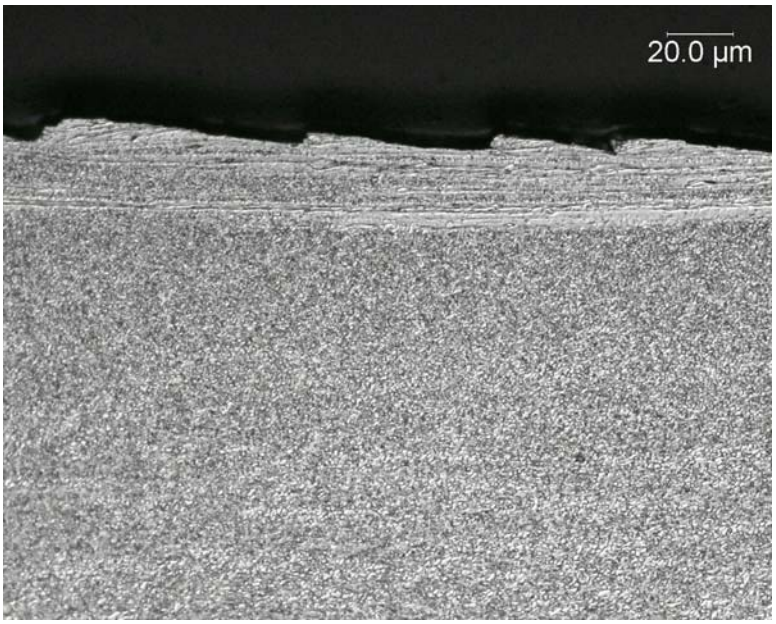


Figure 3.5. Cross-sectional view of line D-D of the bushing of AISI 4130 in Fig. 3.1(b), microstructure of the near-hole area showing a row of overlapping zones of high strain (2% nital etchant).

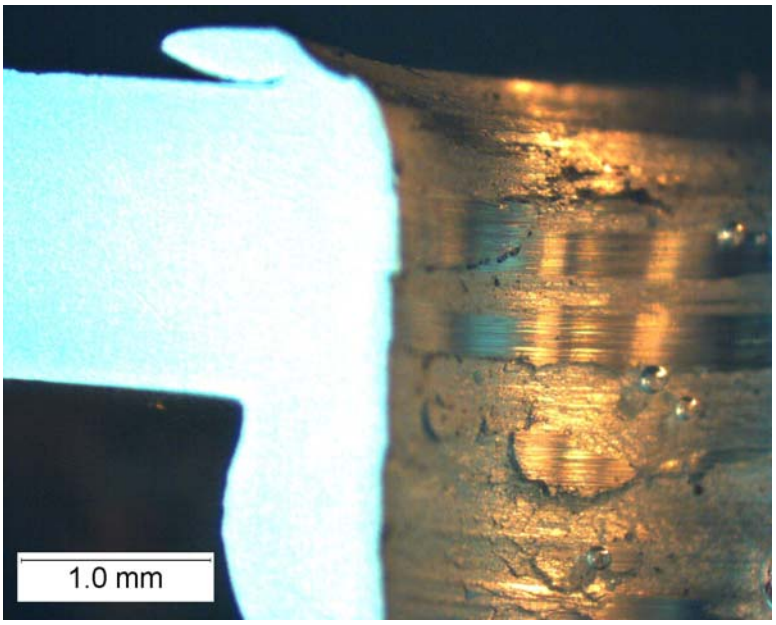


Figure 3.6. Image of the inside of the hole in the Al 5052 sheet showing extensive plastic deformation, delamination, uplift, abrasion, and scored features.

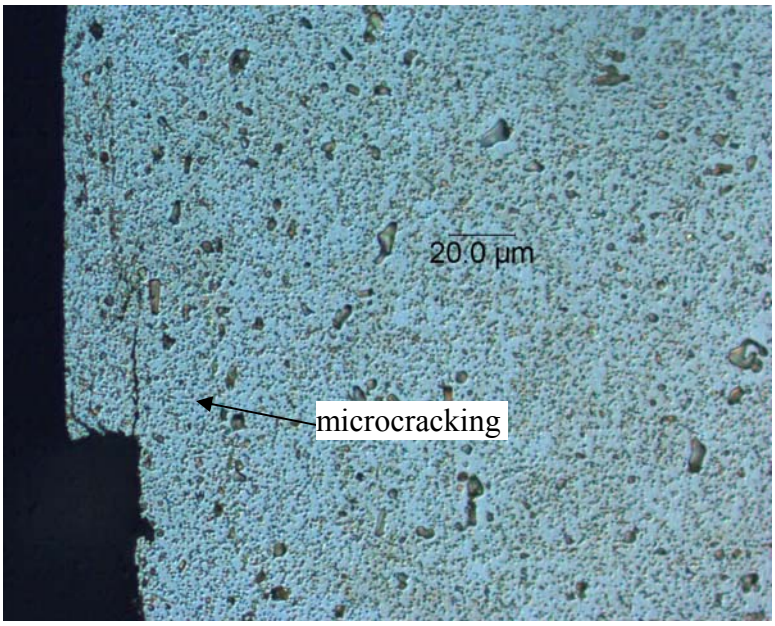


(a)

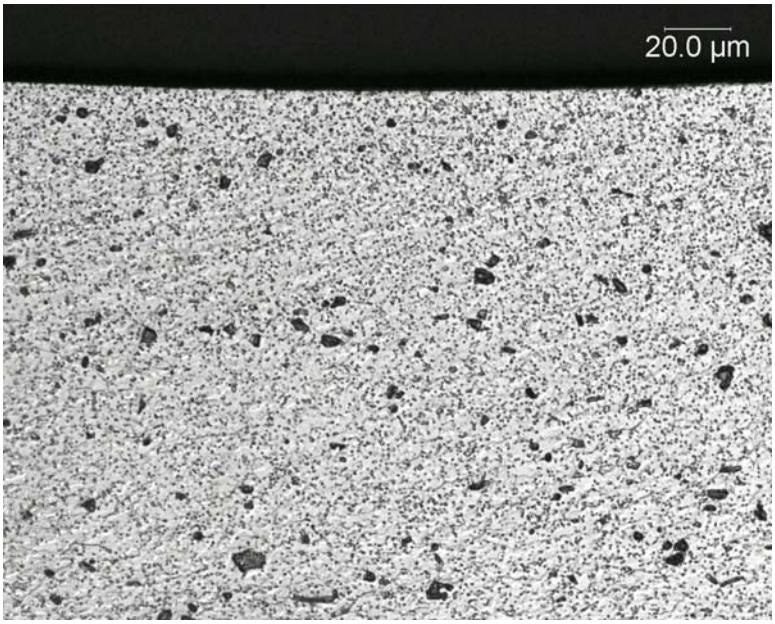


(b)

Figure 3.7. (a) Close-up view of box E in Fig. 3.1(c), microstructure of Al 5052 showing a fine crack parallel to the hole wall above a region where a section of wall material was torn free; and (b) cross-sectional view of line F-F in Fig. 3.1(c), microstructure showing very subtle evidence for shear from right to left, but showing no clear boundary between highly-deformed material and the underlying grain structure. (Keller's etch)

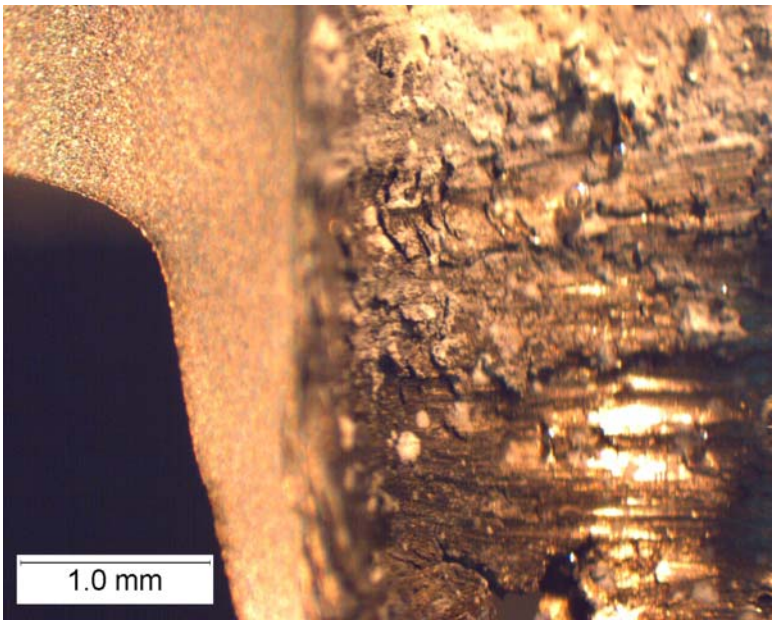


Figure 3.8. Severe plastic deformation and tearing damage in the interior of the hole produced on friction drilled CP Ti sheet.

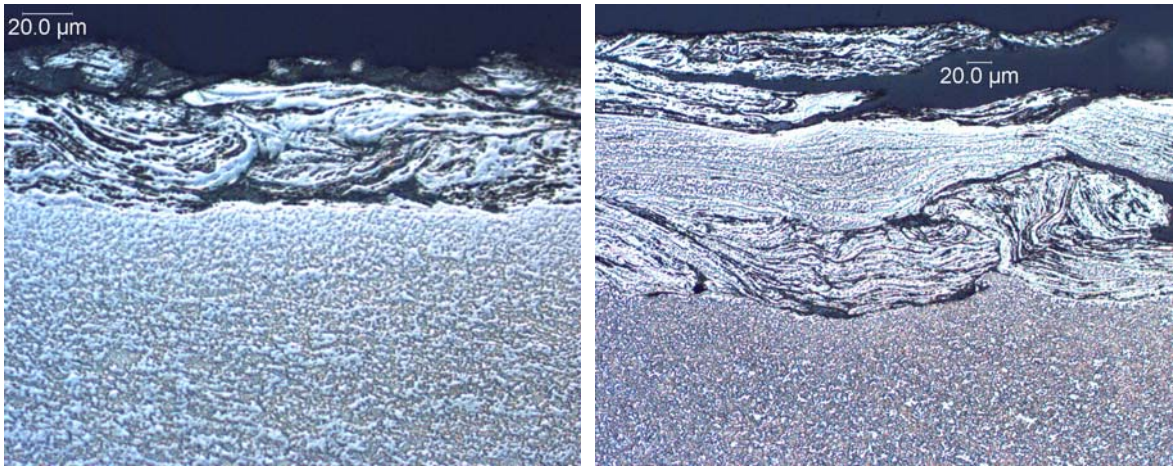


(a) (b)

Figure 3.9. Areas of intense shear and swirling of the Ti sheet material adjacent to the hole surface: (a) box G in Fig. 3.1(d) near the center of the hole length and (b) thicker overlapping layers of severe deformation near the exit end of the bushing in box H in Fig. 3.1(d).

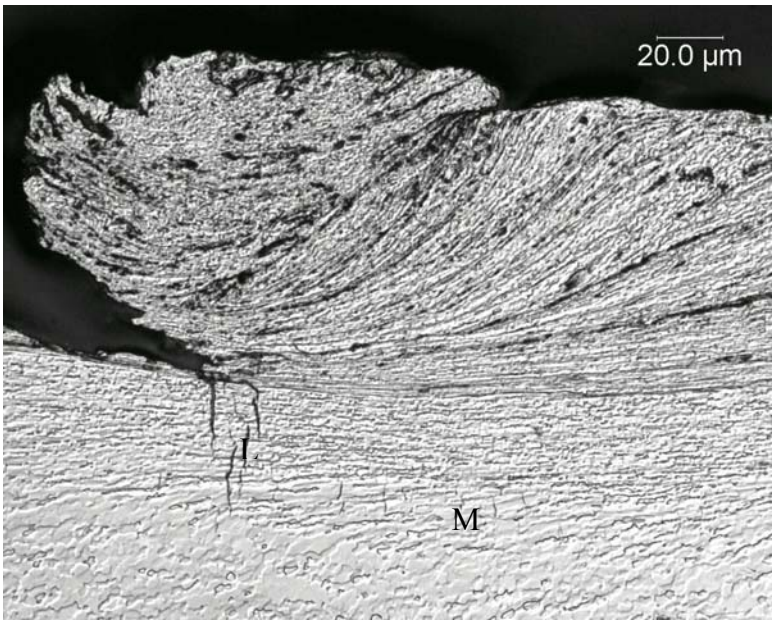


Figure 3.10. Cross-sectional view of line I-I in Fig. 3.1(d), showing swirl of deformed Ti on the surface of the hole, cracks extending from the surface inward, and smaller cracks within the grains below the high-strain surface layers.

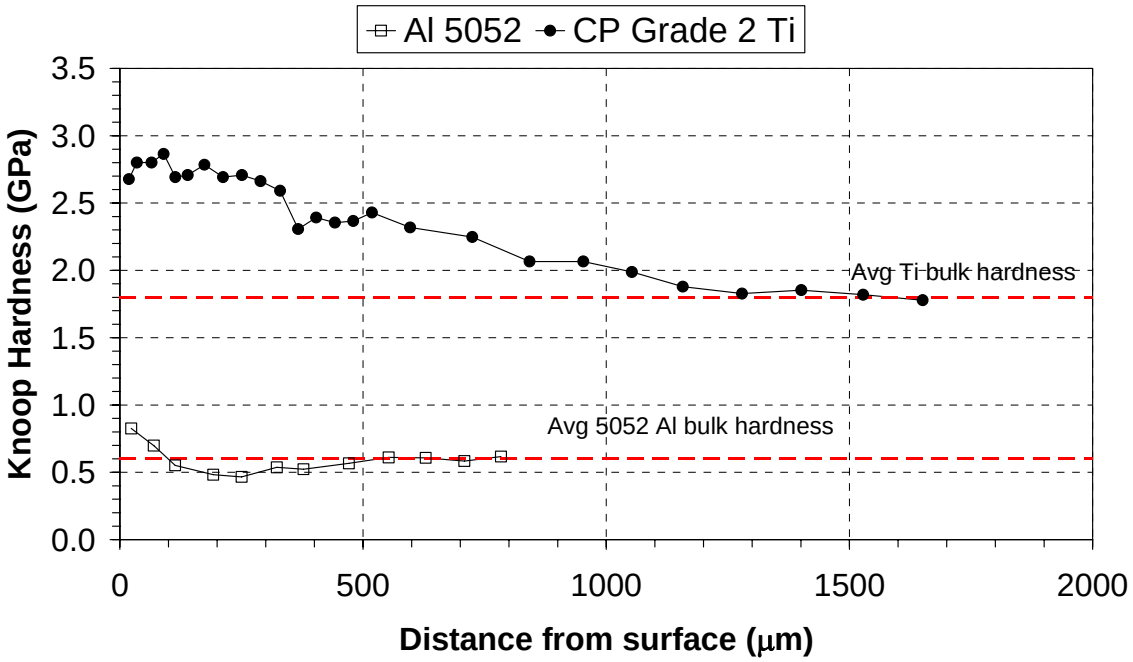


Figure 3.11. Knoop micro-indentation subsurface hardness profile of the friction drilled bore for Al 5052 and CP Ti (0.245 N force used).

## References


[1] M. Reis, R. Louro, P.J. Morais, L. Santos, and H. Gouveia, Microstructural Characterisation of 5083 Al Alloy Joints Friction Stir Welded, Materials Science Forum 514-516 (2006) 510-515.

[2] M. Guerra, C. Schmidt, J.C. McClure, L.E. Murr, and A.C. Nunes, Flow patterns during friction stir welding, Materials Characterization 49 (2003) 95-101.

[3] R.W. Fonda, J.F. Bingert, and K.J. Colligan, Development of grain structure during friction stir welding, Scripta Materialia 51 (2004) 243-248.

[4] T.J. Lienert, W.L. Stellwag Jr., B.B. Grimmett, and R.W. Warke, Friction Stir Welding Studies on Mild Steel, Supplement to the Welding Journal (2003) 1-9.

[5] W.B. Lee, C.Y. Lee, W.S. Chang, Y.M. Yeon, and S.B. Jung, Microstructural investigation of friction stir welded pure titanium, Materials Letters 59 (2005) 3315-3318.

[6] S.F. Miller, H. Wang, R. Li, and A.J. Shih, Experimental and Numerical Analysis of the Friction Drilling Process, ASME Journal of Manufacturing Science and Engineering (accepted) (2004).

[7] Anon, Atlas of Microstructures of Industrial Alloys, Metals Handbook, 8th ed., Vol. 7, ASM International, Materials Park, OH, 1972, p 341-342.

[8] N. Sato, O. Terada, and H. Suzuki, Adhesion of aluminum to WC-Co cemented carbide tools, Journal of the Japan Society of Powder and Powder Metallurgy 44 (4) (1997) 365-368.

[9] Y. Li, T.L. Ngai, W. Xia, Y. Long, and D. Zhang, A study of aluminum bronze adhesion on tools during turning, Journal of Materials Processing Technology 138 (2003) 479-483.

[10] Y.S. Touloukian, R.W. Powell, C.Y. Ho, and P.G. Klemens, Thermal Conductivity; Metallic Elements and Alloys, Thermophysical Properties of Matter, Vol. 1, IFI/Plenum Data Corp., New York, NY, 1970.

[11] Y.S. Touloukian and E.H. Buyco, Specific Heat; Metallic Elements and Alloys, Thermophysical Properties of Matter, Vol. 4, IFI/Plenum Data Corp., New York, NY, 1970.

[12] E.A. Avallone and T. Baumeister III, Marks' Standard Handbook for Mechanical Engineers, 9th ed., McGraw-Hill Book Company, Inc., New York, NY, 1987.

[13] S. Hoyt, Metals Properties, ASME Handbook, 1st ed., McGraw-Hill Book Company, Inc., New York, NY, 1954.

[14] Anon, Metals Handbook, Desk Ed.; 2nd Ed., ASM International, Materials Park, OH, 1998.

# CHAPTER 4.

# FRICTION DRILLING OF CAST METALS

## 4.1. Introduction

Reference [1] has reviewed the technology and principles of the friction drilling process. The process is typically applied to ductile sheet metal, but there is a lack of research in friction drilling of brittle cast metals. For brittle cast metals, the bushing generated by friction drilling exhibits cracks or petal formation. This problem is illustrated in Figs. 4.1 and 4.2. For brittle metals, the deformation of material and petal formation, i.e., fracture in the bushing or lip, is similar to that in the plate perforation or hole flanging using a conical tool [2,3]. Petal formation generates a bushing with limited surface area and load carrying capability for thread fastening.

Figures 4.1(a) and (b) illustrate stages in friction drilling of brittle and ductile metal workpiece, respectively. First, the tool comes into initial contact with the workpiece. Next, at the main thrust stage, the tool penetrates the workpiece and high axial force is encountered. The friction force on the contact surface produces heat and softens the work-material. Then, in the material separation stage, the tool penetrates through the workpiece and makes a hole. The difference in the brittle and ductile workpiece can be seen as the brittle work-material begins to fracture (Fig. 4.1(a)) and the ductile work-material encompasses the tool (Fig. 4.1(b)). Finally, the tool retracts and leaves a hole with a bushing on the workpiece. Pictures of friction drilled bushing using a 5.3 mm diameter carbide tool on the brittle cast aluminum 380 alloy, denoted as Al380 hereafter, and the ductile cold-rolled AISI 1020 carbon steel are shown in Figs. 4.2(a) and 4.2(b), respectively, for comparison. For Al380, due to the fracture or peeling in bushing forming process during friction drilling, much of the work-material is improperly displaced and does not form a bushing with the desired shape or added thickness to the

hole for thread. In comparison, the AISI 1020 workpiece in Fig. 4.2(b) has a smooth, cylindrical bushing shape with sufficient length.

Cast metal materials are widely used for industrial, particularly automotive, applications. Ideally, the friction drilling process can generate a hole in the casting. The self-threading fastener [4] can then be applied to join other devices to the casting using friction drilled holes. This approach can simplify the casting mold design and the subsequent assembly process. The goal of this research is to overcome the poor bushing shape due to the material fracture in friction drilling.

The ratio of workpiece thickness, $t$, to tool diameter, $d$, is an important parameter in friction drilling. The $t$ and $d$ are marked in Figs. 4.1 and 4.3, respectively. A high $t/d$ represents that a relatively larger portion of material is displaced and contributed to the bushing forming. In this experiment for cast metals, the $t/d$ is 0.75. This is high compared to the 0.16 of the AISI 1020 steel in Chapter 2 [1]. In this study, high $t/d$ friction drilling of cast metals is performed.

The experimental setup and procedure are first introduced in this chapter. Thrust force and torque for friction drilling experiments are analyzed. The energy, average power, and peak power required to drill each hole are calculated and analyzed. Finally, the bushing shape and quality are observed and evaluated.

## 4.2. Experimental setup and procedure

A Mori-Seiki TV-30 CNC vertical machining center was used for the friction drilling of Al380 with workpiece pre-heating. For high spindle speed test, a Milacron Saber CNC vertical machining center was used. The drilling setups in both machines were the same. Overview of the setup in Mori-Seiki TV-30 is shown in Fig. 4.4. The workpiece was held in a vise on top of a Kistler model 9272A piezoelectric drilling dynamometer, used to measure the axial thrust force and torque during drilling. The tool was held by a standard collet tool holder. Figure 4.3 shows key dimensions of a friction drilling tool. The tool used in this study has $d$ = 5.3 mm, $\alpha$ = 90°, $\beta$ = 36°, $h_c$ = 0.940 mm, $h_n$ = 5.518 mm, and $h_l$ = 7.043 mm. The tool material is tungsten carbide in cobalt matrix.

Two materials experimented in this friction drilling study are 4.0 mm thick die cast Al380 and magnesium AZ91D alloy, denoted as MgAZ91D. Al380 is the aluminum-silicon-copper alloy. MgAZ91D is a light-weight magnesium-aluminum-zinc alloy. Table 4.1 shows material properties of these materials relevant to friction drilling, compared to properties for AISI 1020 steel, which is used in the previous friction drilling tests in Chapter 2 [1]. Materials with higher strength should require more thrust force to be penetrated. Elongation at break is an indicator of the work-material machinability and can be correlated to the quality of bushing. The low elongation at break of cast metals suggests the high likelihood of fracture and petal formation. Thermal properties provide information on how the work-material responds to the frictional heating at tool-workpiece interface. The heat transfers away from the interface region quickly for high thermal conductivity workpiece, which, in turn, reduces the workpiece temperature and ductility for bushing formation. Melting temperature of the workpiece material is also important. The maximum temperature generated in friction drilling was noticed to be about 1/2 to 2/3 of the workpiece melting temperature by infrared camera [1].

Two ideas, the pre-heating of workpiece to elevated temperature and the high spindle speed friction drilling, were hypothesized. It is well known that, at elevated temperature the cast metal has increased plasticity, which can make the work-material conform to the tool and less likely to fracture during friction drilling. For magnesium alloy, the exothermic oxidation at elevated temperature is a problem. The cast MgAZ91D ignited inside the oven during heating. Therefore, friction drilling of MgAZ91D at elevated temperature was not performed in this study. In another effort to increase the temperature and plasticity in work-material, high spindle speed tests, greater than 5500 rpm, were conducted for both materials. It has been shown in friction stir welding that more heat is generated at higher rotational speed of the tool [5,6]. The effect of spindle speed in friction drilling is studied.

Table 4.2 shows the test matrix. Four sets of experiment, marked as Exps. I-IV, were conducted to study the effect of workpiece temperature and feed rate on friction drilling of Al380. The spindle speed remained constant at 5500 rpm. The highest workpiece temperature of Al380 was limited to 300ºC. Above this temperature, severe surface oxidization and bubble formation were observed in the workpiece. At 300ºC, the

highest feed rate at 406 mm/min was utilized in Exp. IV. The feed rate was varied according to workpiece temperature as described in Table 4.2.

To achieve the elevated temperature in Exps. I-IV, the Al380 workpiece was first heated in an oven to slightly beyond 300ºC. The workpiece was then removed from the oven and placed in the vise. Then, as shown in Fig. 4.4, a contact thermocouple (Omega Model KMQIN-062G-6) with 1.5 mm diameter was placed in a small hole on the workpiece to predict the temperature at the friction drilling location. The thermocouple reading was monitored as the workpiece cooled. The workpiece cooling was quick at first, but became more gradual as temperature decreased. As the temperature at point D cooled down and reached the targeted 300, 200, and 100ºC values, a hole was drilled at point D. Estimated error in workpiece temperature was estimated to be $\pm 5^{o}$C.

The workpiece used in this study, as shown by the top and bottom views in Fig. 4.5, has a symmetrical shape relative to the center line. Temperatures at two points, marked as T and D in Fig. 4.5, should be about the same, assuming the thermal transport in the workpiece is symmetric relative to the center line. Point T is the thermocouple location for temperature measurement. Point D is the center of the friction drilled hole. These two points have the same distance, $l$, to the center line, as shown in Fig. 4.5. The temperature at location D was predicted by the thermocouple at point T.

High spindle speed drilling tests, Exp. V for Al380 and Exp. IV for MgAZ91D, were performed at room temperature workpiece under the same feed rate of 254 mm/min. Four spindle speeds experimented were 3000, 7000, 11000, and 15000 rpm.

For every test in Exps. I-VI, the thrust force and torque were measured and bushing quality was examined. The sampling rate was 750 samples per second. The measured data was filtered using a moving average.

### 4.3. Thrust force and torque

The measured thrust force and torque of Exps. I-IV for friction drilling of Al380 at 25, 100, 200, and 300ºC are shown in Fig. 4.6. The horizontal axis represents the time and distance of tool travel from the initial contact between tool and workpiece. The time to penetrate the workpiece varies depending on the feed rate. The shape of the thrust

force vs. time is different from that of the high and narrow peak at the start of contact in friction drilling of steel sheet metal as presented in Chapter 2. For friction drilling of cast metal with high $t/d$, the thrust force increases at a slower rate to a peak value, about 3 mm tool travel from the start of contact. At this tool location, the frictional heating becomes more effective to raise the workpiece temperature and soften the work-material (4 mm thick). From the peak, the thrust force reduces at an almost constant rate until the tool penetrates the workpiece and the thrust force reaches a value close to zero.

The general trend for torque, which rises and falls at a slow rate, is different from that of thrust force but similar to that of torque in friction drilling of AISI 1020 steel (Chapter 2). The contact area on the peripheral of the tool determines the torque, which usually peaks after the tool has penetrated the workpiece. As shown in Fig. 4.6, the peak of torque occurs at about 6 to 8 mm from the start of contact, much later than the peak of thrust force. The distance of tool travel to generate a hole with a bushing is about 11 mm from the start of contact.

The benefit of high feed rate to reduce cycle time in friction hole drilling of pre-heated workpiece is demonstrated. For the 254, 305, 356, and 406 mm/min feed rate, the time for hole generation is about 2.5, 2.0, 1.8, and 1.6 s, respectively.

In Fig. 4.6 secondary peaks in thrust force and torque can be seen. After penetration, the shoulder of the tool, which is marked in Fig. 4.3, contacted the back-extruded work-material. It pushed in and flattened the face of the workpiece, as shown later in the cross-section view of drilled holes. The contact of tool shoulder and workpiece created the secondary peak of thrust force and torque after the tool penetration of workpiece. Fig. 4.6 shows that peak values of this thrust force and torque could be large, even higher than the thrust force and torque in penetration, due to the large shoulder area of the tool used in this study. If a tool without shoulder is used, no secondary peak of the thrust force and torque is expected. In this case, a small bushing will be formed by the back extrusion of the work-material at the entry of the friction drilled hole.

Effects of workpiece temperature and feed rate on peak thrust force and torque were analyzed. In Exp. I, at 25, 100, 200, and 300ºC workpiece temperatures, the peak thrust forces are 1900, 1500, 1000, and 700 N and the torques are 2.0, 1.7, 1.3, and 1.0 N-m,

respectively. The benefit of high workpiece temperature to reduce the thrust force and torque is identified. Lower peak forces and torques mean that higher feed rate can be applied at high workpiece temperature. From Exps. I to IV, under the same 300ºC workpiece temperature, the feed rate of 254, 305, 356, and 406 mm/min generate peak thrust force of 700, 700, 800, and 1100 N and peak torque of 1.0, 1.4, 1.2, and 1.7 N-m, respectively. The rapid increases of thrust force and torque show the limitation of high feed rate in practical friction drilling of pre-heated workpiece.

Large variation or noise of the torque was noticed. This is due to the material adhesion from the Al380 workpiece to the tool. Aluminum is known to have a high affinity for the tool [7]. A layer of build-up aluminum alloy transfered to the tool surface. Filing and sanding processes were applied to clean the tool after each hole was drilled to remove the build-up work-material and to ensure the consistent tool surface quality and repeatable thrust force and torque measurements. The tool tip is usually clean without the adhesion of work-material. The low surface speed at the tool tip indicates that the speed and temperature are key factors in the adhesion of aluminum alloy on the tool surface. This observation suggests further investigations of material transfer and adhesion and possibly of using a tool coating to alleviate this problem.

The effect of spindle speed on the thrust force and torque in friction drilling of room temperature Al380 and MgAZ91D under the same feed rate, 254 mm/min, is shown in Fig. 4.7. At 3000, 7000, 11000, and 15000 rpm spindle speeds, the peak thrust forces are 3300, 2000, 1500, and 1200 N for Al380 and 2700, 1800, 1000, and 800 N for MgAZ91D, respectively. All tests show the MgAZ91D has slightly lower peak thrust force than that of Al380. At the low, 3000 rpm, spindle speed the thrust force and torque are very high. High peak torque of Al380 and MgAZ91D at 5 and 3 N-m, respectively, can be seen at 3000 rpm. Benefits of decreasing thrust force and torque from 3000 to 7000 rpm spindle speed are very obvious. This demonstrates a threshold tool speed for friction drilling. In Sec. 4.4, the energy and power for friction drilling can further validate this observation quantitatively. The increased spindle speed reduces the torques to about 1 to 2 N-m and 0.5 to 1.5 N-m for Al380 and MgAZ91D, respectively, at high spindle speeds. High variation of torque at high spindle speeds can be observed. This is due to the adhesion of work-materials to the tool at high speed.

## 4.4. Energy and power in friction drilling

The analysis of power and energy in friction drilling provides the basic information for the machine requirements, such as the selection of the spindle and design of the fixture for workholding. Most of the energy converts into heat and transfers to the workpiece and tool.

Over the time $\Delta T$ from the start of tool-workpiece contact to penetration of the hole, the energy $E$ required for friction drilling can be expressed as:

$$E = \int_0^{\Delta t} Fvdt + \int_0^{\Delta t} T\omega dt \tag{1}$$

where $\Delta t$ is the time duration of drilling, $F$ is thrust force, $v$ is tool axial velocity, $t$ is time, $T$ is torque, and $\omega$ is tool rotational speed. The rotational motion contributes to nearly all, over 99%, of the energy consumed in friction drilling.

The average power required to generate a hole by friction drilling is $P_{av}$:

$$P_{av} = E / \Delta t \tag{2}$$

The maximum power delivered in the friction drilling process is $P_{max}$:

$$P_{max} = T_{max}\ \omega \tag{3}$$

where $T_{max}$ is maximum torque. This is assuming that the force term contributing to the maximum power is comparatively small and neglected.

By analyzing the measured thrust force and toque, $E$, $P_{av}$, and $P_{max}$ for each drilling condition can be analyzed.

### 4.4.1. Energy, *E*

The top row in Fig. 4.8 shows the energy $E$ vs. workpiece temperature and spindle speed for friction drilling. In Exps. I-IV, four sets of data points for energy basically overlap each other. This indicates that the energy required to drill a hole is independent

of the feed rate. The workpiece temperature has a significant effect on the energy. As the temperature increased from 25 to 300°C, the energy is reduced in an almost linear trend from 2000 to 1000 J. The high temperature softens the work-material and reduces the energy required for hole drilling.

Results of Exps. V and VI reveal effects of spindle speed and type of work-material. For both Al380 and MgAZ91D, high spindle speed reduces the energy for friction drilling. Consistently, MgAZ91D requires lower energy than Al380. An exponentially decaying $E$ vs. spindle speed is observed, as illustrated in the almost linear trend line of log-scale $E$ vs. spindle speed for both work-materials. Friction hole drilling has to have a sufficiently high spindle speed to make the process effective. Higher spindle speed generates more heat in the tool-workpiece interface, which locally increases the workpiece temperature and enables the effective hole penetration. By increasing the speed from 3000 to 7000 rpm, the energy per hole is reduced from 5200 to 2000 J for Al380. The same significant drop of energy can also be observed in MgAZ91D. In the high spindle speed range, the increase in spindle speed has less noteworthy impact of the energy reduction.

### 4.4.2. Average power, $P_{av}$

The second row in Fig. 4.8 shows the average power $P_{av}$ for friction drilling. Unlike the energy, the feed rate has some effect on $P_{av}$. Under the same workpiece temperature, lower feed rate has lower $P_{av}$. The workpiece temperature also has the close to linear effect on the reduction of average power required for hole drilling. In Exps. I-VI, the highest $P_{av}$, about 880 W occurs at the lowest workpiece temperature (25°C) and slowest feed rate (254 mm/min). This is a high but reasonable number for drilling a 5.3 mm diameter hole in Al380. High temperature at 300°C can help reduce the $P_{av}$ to 480 W. However, at the same 300°C, $P_{av}$ increased to 700 W for drilling at the highest feed rate (406 mm/min). Since the time duration for hole generation is shorter in hole drilling at high feed rate, the energy per hole is about the same under all four feed rate at 300°C workpiece temperature.

In Exps. V and VI, the exponentially decaying $P_{av}$ vs. spindle speed can also be observed for both Al380 and MgAZ91D. Mg AZ91D also has smaller $P_{av}$ than Al380.

### 4.4.3. Peak power, $P_{max}$

The peak power $P_{max}$ in friction drilling is illustrated in the bottom row in Fig. 4.8. The feed rate and workpiece temperature both affect the $P_{max}$. In general, higher $P_{max}$ was observed at higher feed rate. There are exceptions for 305 and 356 mm/min feed rate. A linear trend of reducing $P_{max}$ vs. workpiece temperature can also be identified.

For Al380 and MgAZ91D, the $P_{max}$ decreases consistently as the spindle speed increases. At the lowest spindle speed (3000 rpm), the peak power of 3000 W is quite high for drilling a 5.3 mm hole in Al380. On the contrary, at 15000 rpm, the peak power is only 570 W for Al380 and 460 W for MgAZ91D.

## 4.5. Shape of bushing

The shape of bushing and the depth of the hole are two important but difficult to quantify criteria in evaluation the quality in friction drilling. Qualitative observations of the bushing shape, based on cylindricality, petal formation, depth, and roughness, were made to judge the success of the friction drilled hole in each case.

### 4.5.1. Workpiece heating effect on bushing shape and petal formation

Figure 4.9 shows bushing shape from friction drilling of Al380 at different temperatures. Workpiece temperatures in Figs. 4.9(a)-(d) are 25, 100, 200, and 300ºC, respectively. The view of bushing from bottom of the workpiece and a cross section view of the same hole are shown to reveal and compare different features of the hole and bushing. Petal formation, an undesirable characteristic in friction drilling of cast metals, is marked in Fig. 4.9(a). These petals, as marked in Fig. 4.9, were observed to peel from the workpiece in the radial direction. The petal still has the bright, curved surface like the inside of the bushing. This indicates that the petal was part of the bushing during the early stage of friction hole drilling. As the strain in the bushing reaches a critical value, the bushing fractures along the axial direction and bursts into five to eight petals. Four petals bushing can sometimes be observed. The $t/d$ ratio greatly influences the number of petals. Under the small $t/d$ ratio, more petals can be formed in each busing. This has been observed experimentally.

Accompanying the petals are cracks that extend nearly the length of the bushing at the 25 and 100ºC workpiece, as shown in Figs. 4.9(a) and 4.10(b). At 200ºC, as shown in Fig. 4.9(c), the crack does not extend the whole length of bushing. This shows the petal formation is dependent on the material properties and the benefits of workpiece pre-heating. At 300ºC, as shown in Fig. 4.9(d), there is less obvious cracks and petals. The petal formation and cracking are traits of poor bushing formation due to limited ductility of work-material. The petal formation translates to less added thickness for thread on friction drilled holes. Streaks from the tool, as marked in Fig. 4.9(b), are an indication of workpiece surface damages and the adhesion of work-material to the tool, as discussed in detail in Chapter 3.

As workpiece temperature increases, the bushing formed becomes more cylindrical and has less fracture and radial displacement. This is especially evident in the cross section views. This experiment indicated that drilling at elevated temperature made the workpiece material more ductile and formable, and hence the bushing shape more cylindrical.

No changes in bushing quality were noticed for varying feed rate in the experiment.

### 4.5.2. Spindle speed effect in Al380 and MgAZ91D

Figure 4.10 shows the bushing formed in Al380 and MgAZ91D at 3000, 7000, 11000, and 15000 rpm spindle speed. For Al380 at room temperature (no pre-heating the workpiece), as shown in Fig. 4.10(a), no significant change in bushing shape is noticed by varying the spindle speed. Although the energy and power were reduced at high spindle speed, the bushing shape is still poor at the highest spindle speed. Significant petal formation and cracking are observed in each of the hole. This further distinguished the benefit of workpiece pre-heating to improve the shape of bushing, as discussed in Sec. 4.5.1 and shown in Fig. 4.9.

Spindle speed has a negative effect on the shape of bushing for MgAZ91D. As shown in Fig. 4.10(b), as the spindle speed increases from 3000 to 15000 rpm, the petal formation becomes more apparent. At 3000 rpm, the shape of bushing is ragged, but no petal formation or peeling is noticed. At 7000 rpm, some but not significant petal formation can be seen in the bushing. At 15000 rpm, very extensive petal formation,

similar to the bushing in friction drilled holes of on room temperature Al380. In addition, the layered petal formation in MgAZ91D, as marked in Fig. 4.10(b), can be seen. This is likely due to the sliding of a layer of work-material surrounding the tool during the burst of petals.

## 4.6. Conclusions

For Al380, the shape and quality of bushing were observed to improve at higher workpiece temperature. Less severe cracking and petal formation were observed on bushings formed at elevated workpiece temperature. This study implies that external heating can be beneficial to increase ductility and improve bushing formation on brittle materials. The high spindle speed did not affect the bushing formation for room temperature Al380. For room temperature MgAZ91D, high spindle speed was detrimental on the bushing shape.

The workpiece preheating and high spindle speed was beneficial to reduce the thrust force, torque, energy, and power for friction drilling of brittle cast metals. Higher feed rate and shorter cycle time for hole drilling was feasible with the reduced thrust force and torque.

Table 4.1. Comparison of material properties [9,10].

| | Al380 | MgAZ91D | AISI 1020 carbon steel, cold rolled |
|---|---|---|---|
| Density ($kg/m^3$) | 2710 | 1810 | 7870 |
| Hardness, Brinell ($kgf/mm^2$) | 80 | 63 | 121 |
| Elongation at break (%) | 3 | 3 | 15 |
| Ultimate tensile strength (MPa) | 330 | 230 | 420 |
| Tensile yield strength (MPa) | 165 | 150 | 350 |
| Modulus of elasticity (GPa) | 71 | 45 | 205 |
| Thermal conductivity (W/m-K) | 96.2 | 72.0 | 51.9 |
| Melting point (°C) | 540 - 595 | 470 - 595 | 1430 |

Table 4.2. Test matrix for friction drilling of heated workpiece and high spindle speed tests.

| Exp. | Work material | Feed rate (mm/min) | Spindle speed (rpm) | Workpiece temperature (°C) |
|---|---|---|---|---|
| I | Al380 | 254 | 5500 | 300<br>200<br>100<br>25 (room) |
| II | Al380 | 305 | 5500 | 300<br>200<br>100 |
| III | Al380 | 356 | 5500 | 300<br>200 |
| IV | Al380 | 406 | 5500 | 300 |
| V | Al380 | 254 | 3000<br>7000<br>11000<br>15000 | 25 (room) |
| VI | MgAZ91D | 254 | 3000<br>7000<br>11000<br>15000 | 25 (room) |

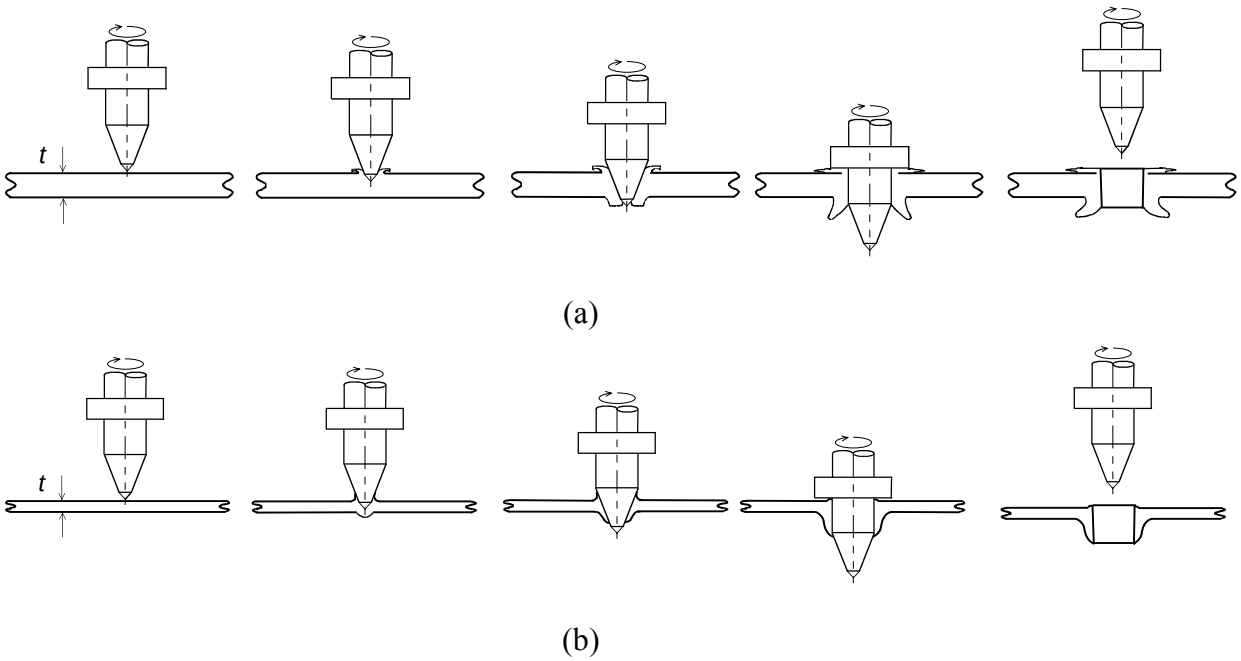


Figure 4.1. Comparison of friction drilling steps in (a) brittle cast metal and (b) ductile sheet metal.

(a) (b)

Figure 4.2. Bushing of friction drilled hole using 5.3 mm diameter tool: (a) cast Al380 at 5500 rpm with petal formation and bushing fraction and (b) AISI 1020 carbon steel at 2500 rpm.

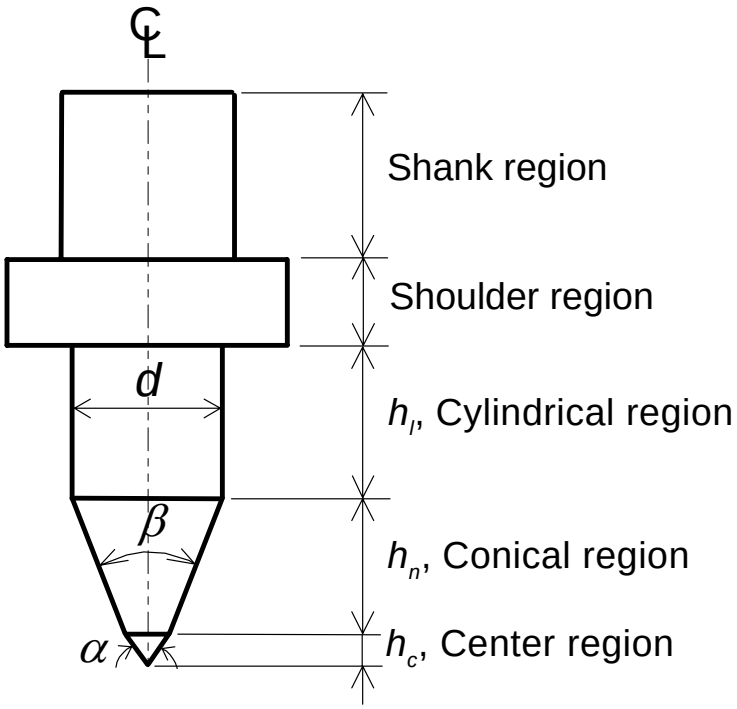


Figure 4.3. Key dimensions of the friction drilling tool.

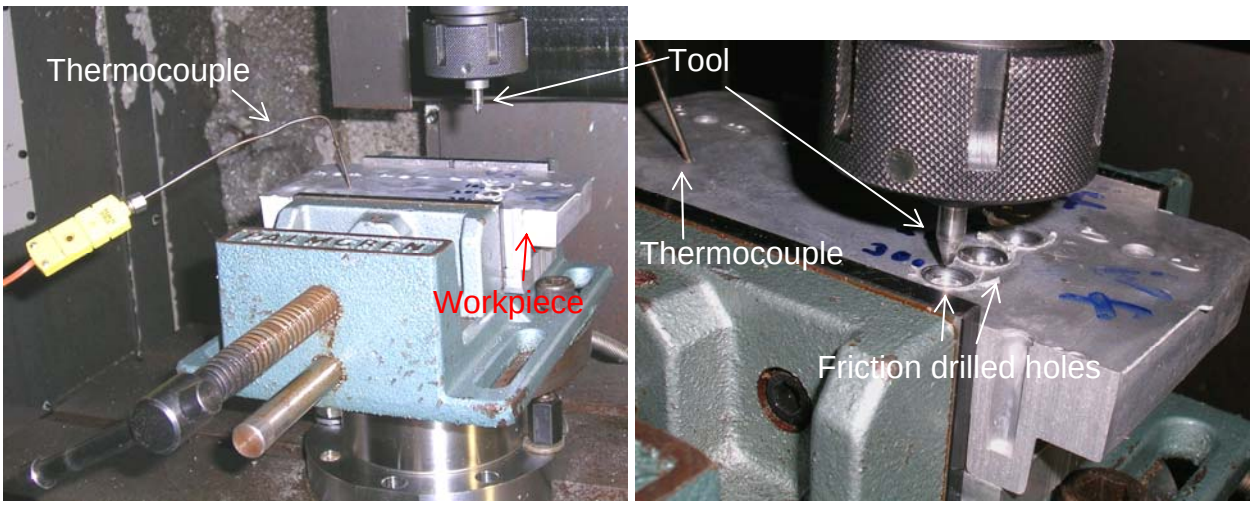


(a) (b)

Figure 4.4. Experimental setup with tool, workpiece, vise, thermocouple, and drilled holes: (a) overview and (b) close-up view.

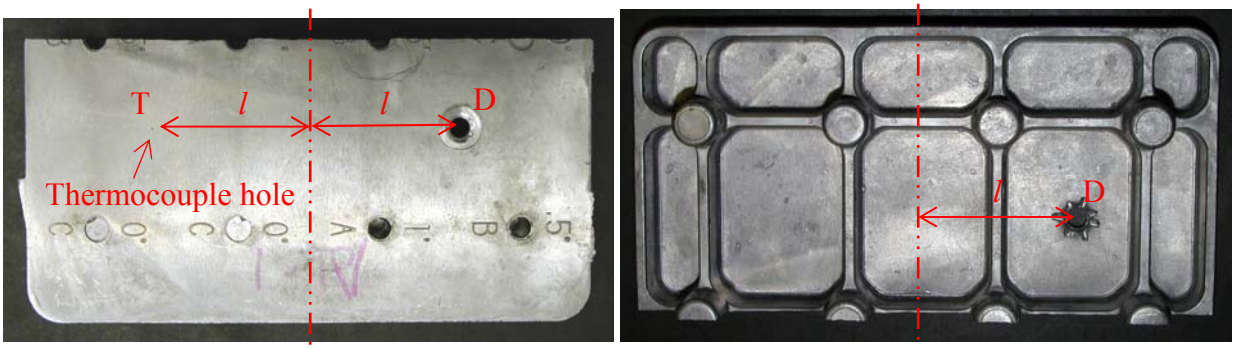


(a) (b)

Figure 4.5. Symmetry shape of the Al380 workpiece: (a) top view and (b) bottom view.

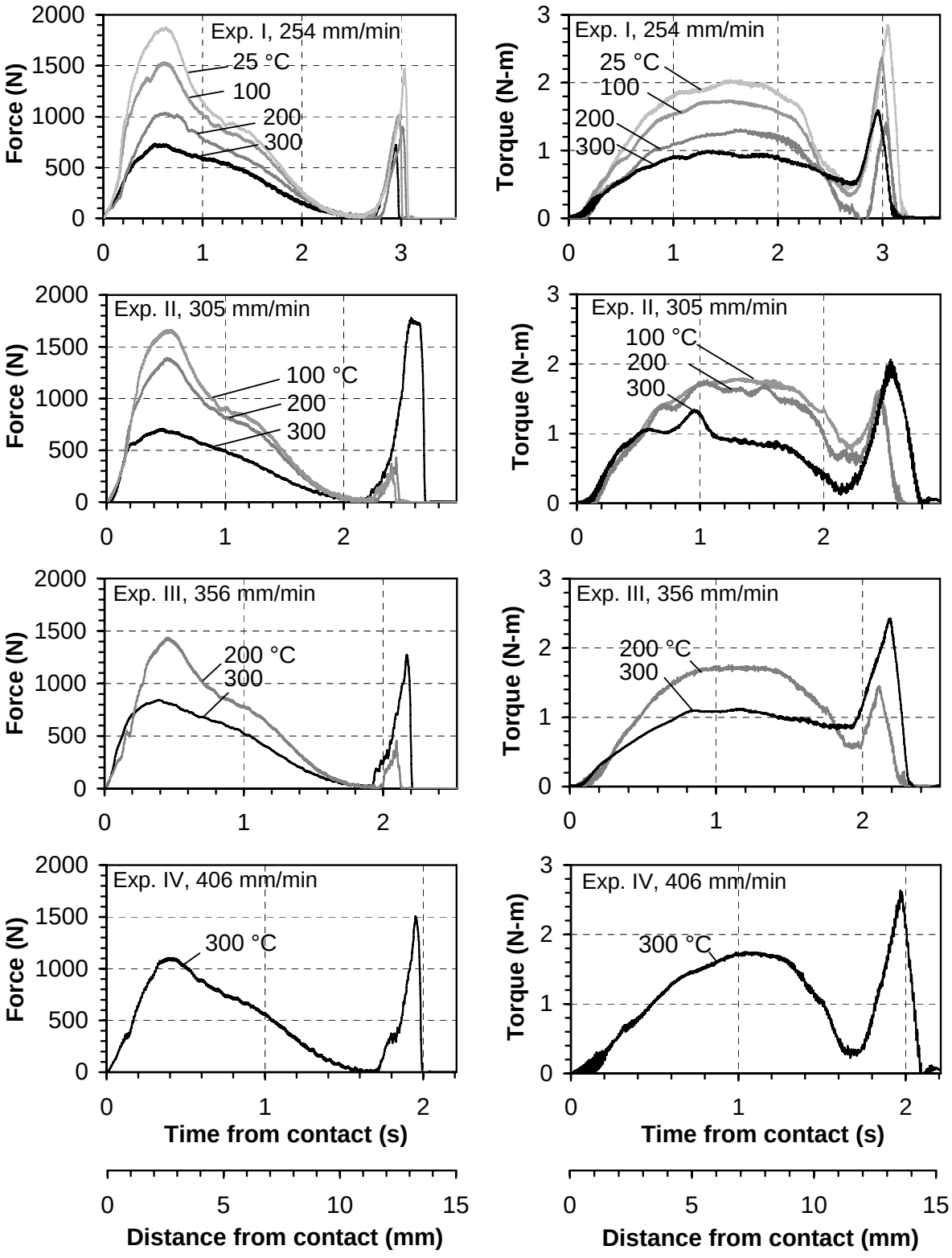


Figure 4.6. Thrust force and torque in friction drilling of cast Al380 workpiece at 5500 rpm in Exps. I-IV.

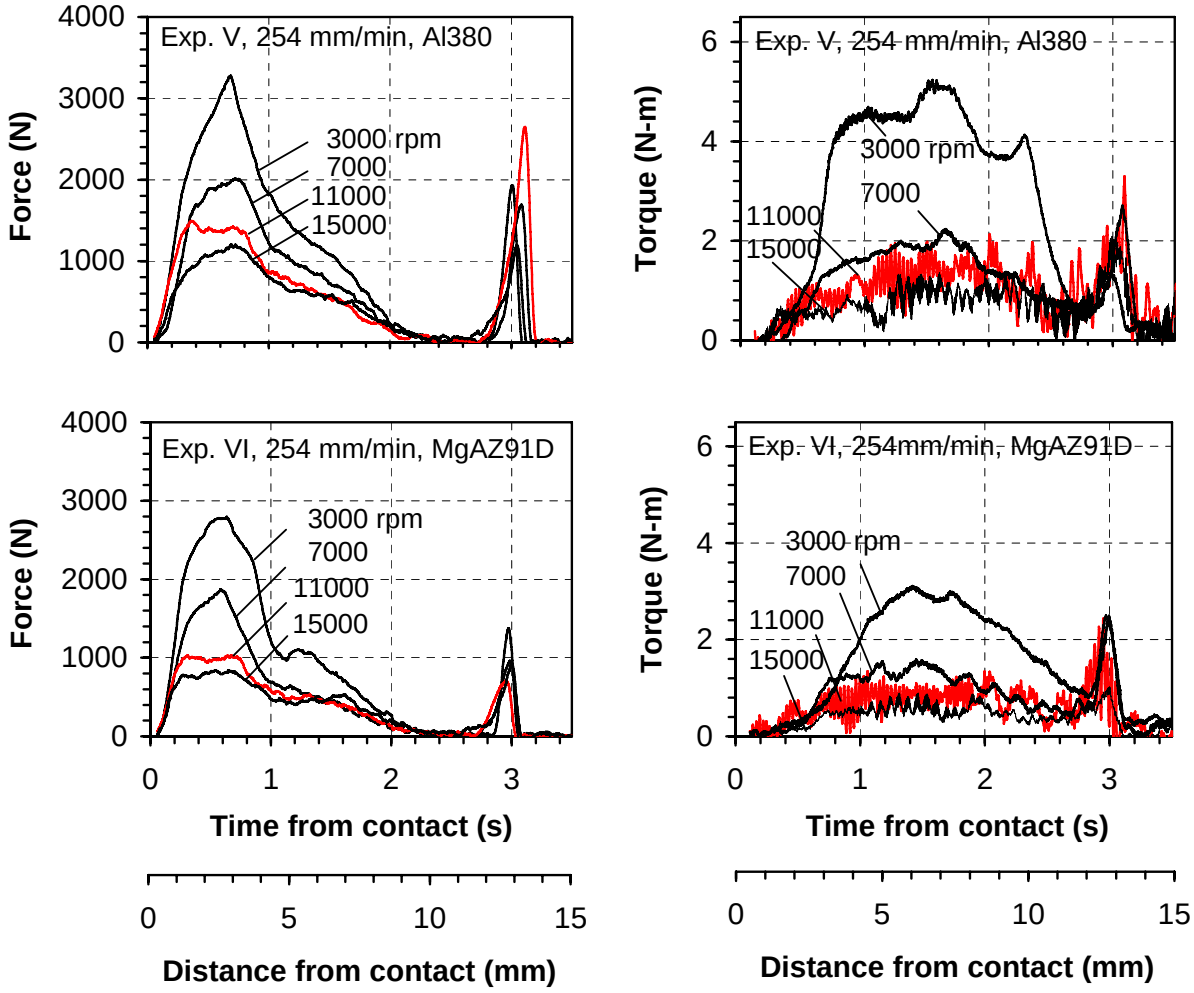


Figure 4.7. Spindle speed effect on the thrust force and torque in friction drilling at 254 mm/min feed rate in Exps. V and VI.

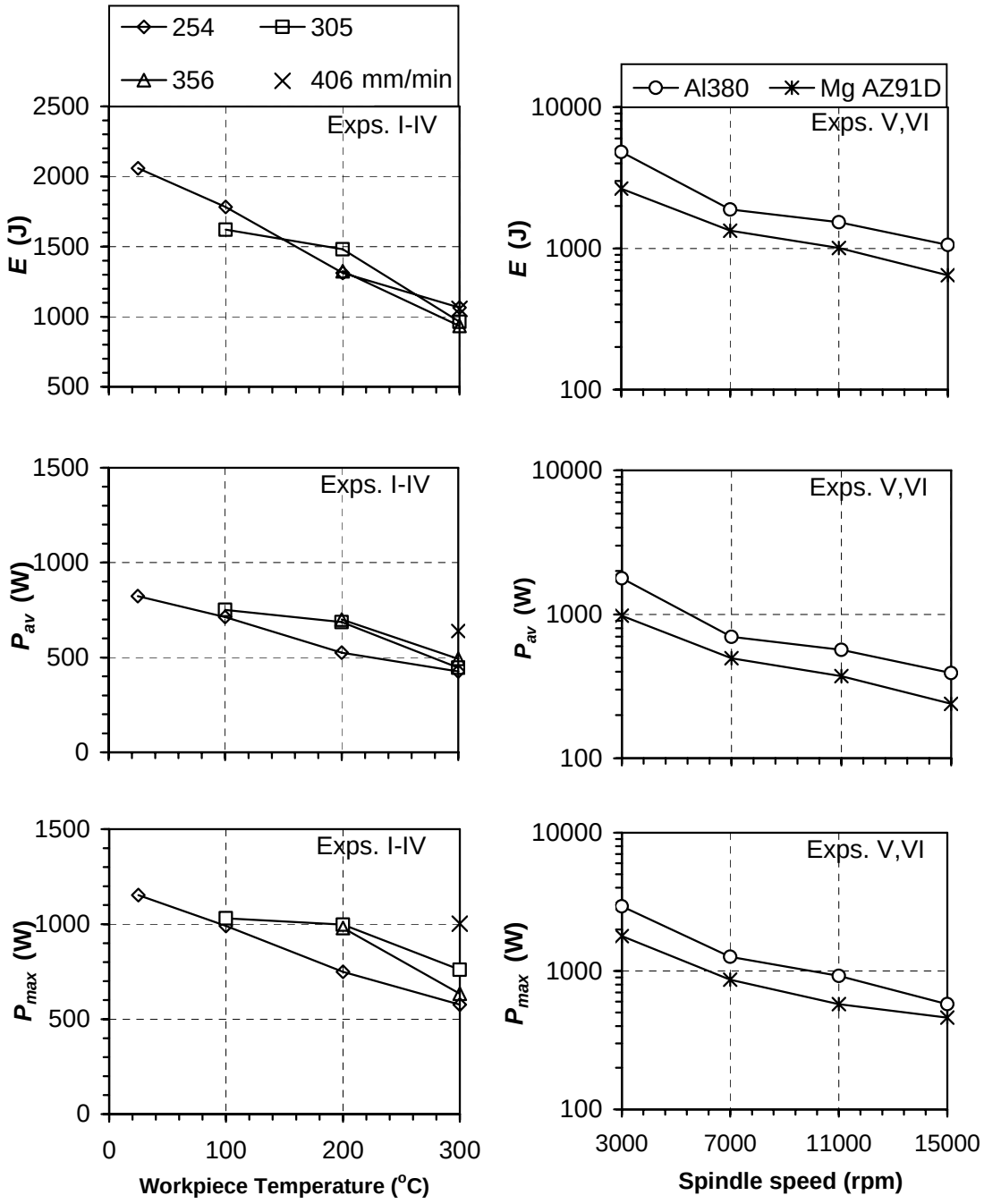


Figure 4.8. Energy and average and peak power in friction drilling, 5500 constant rpm spindle speed in Exps. I-IV and 254 mm/min feed rate in Exps. V and VI.

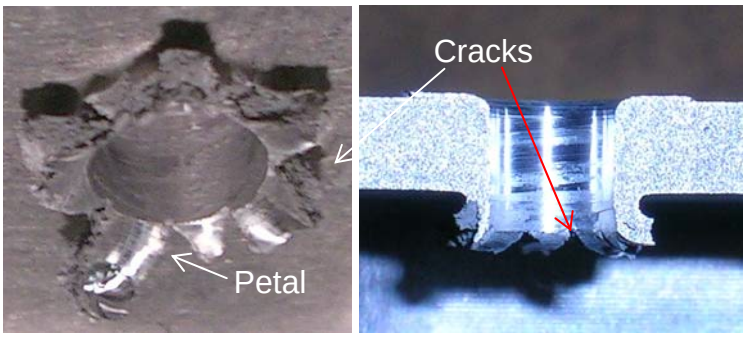


(a) 25°C


(b) 100°C

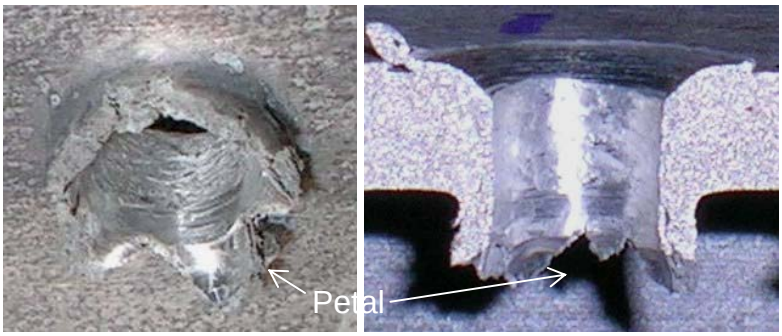


(c) 200°C

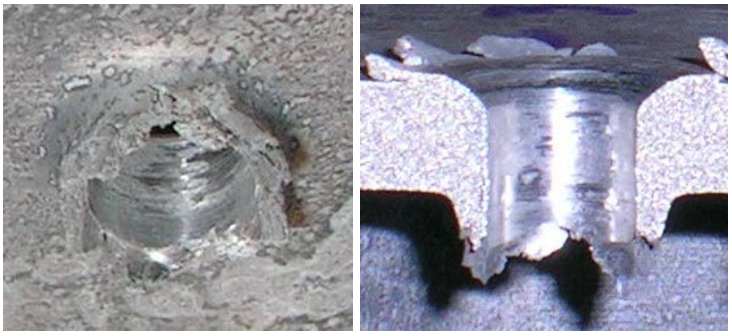

(d) 300°C

Figure 4.9. Bushing and bushing cross section formed in friction drilling of Al380 at 254 mm/min feed rate and 5500 rpm spindle speed in Exp. I.

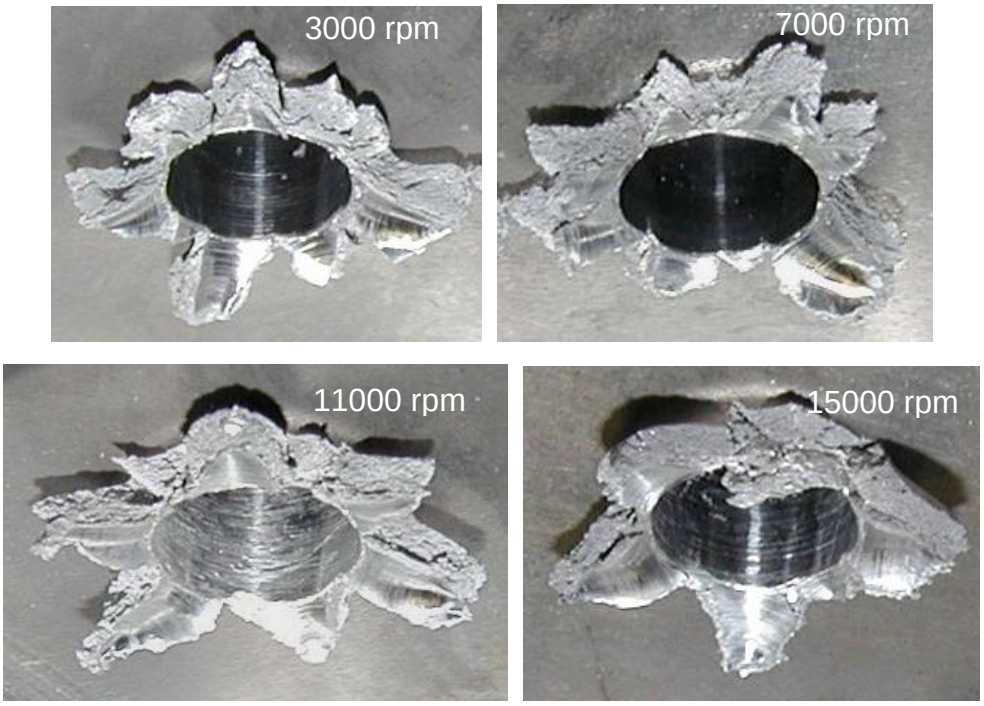


(a) Al380, Exp. V

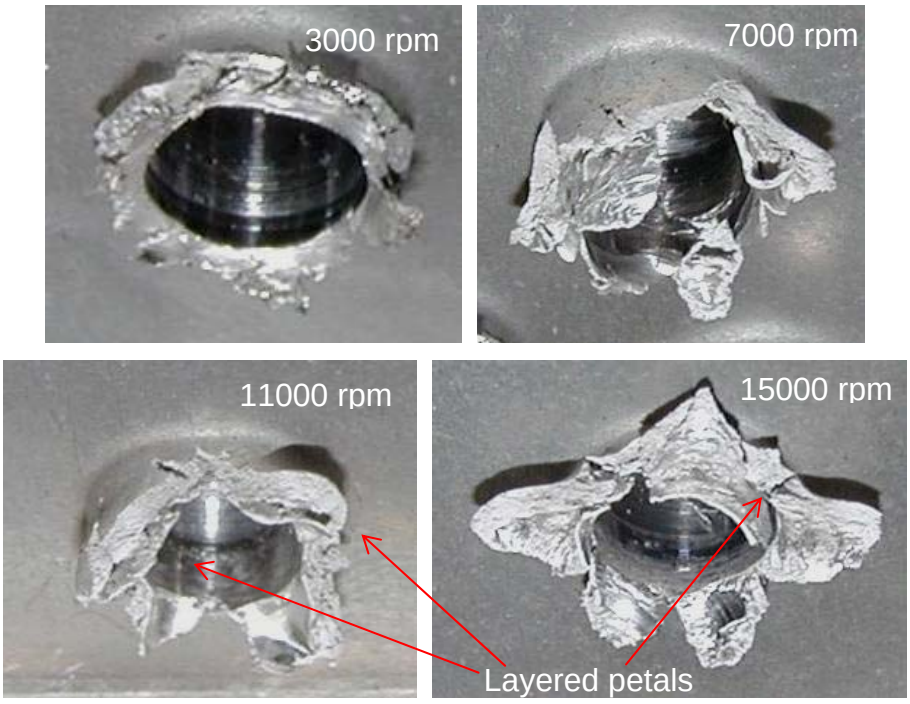


(b) MgAZ91D, Exp. VI

Figure 4.10. Bushing and bushing cross section formed in Exps. V and VI.

## References


[1] S.F. Miller, H. Wang, R. Li, and A.J. Shih, Experimental and numerical analysis of the friction drilling process, ASME Journal of Manufacturing Science and Engineering (accepted) (2004).

[2] W.J. Johnson, N.R. Chitkara, A. H. Ibrahim, and A. K. Dasgupta, Hole flanging and punching of circular plates with conically headed cylindrical punches, Journal of Strain Analysis 8 (1973) 228-241.

[3] N.M. Wang and M.L. Wenner, An analytical and experimental study of stretch flanging, International Journal of Mechanical Science 16 (1974) 135-143.

[4] D.M. Paxton, M.T. Smith, J.A. Carpenter, and P.S. Sklad, Application of thread-forming fasteners (TFFs) in net-shaped holes, FY 2004 Progress Report for Automotive Lightweight Materials, FreedomCAR and Vehicle Technologies Program, U.S. DOE, 2004, pp. 263-266.

[5] H. Schmidt, J. Hattel, and J. Wert, An analytical model for the heat generation in friction stir welding, Modelling and Simulation in Materials Science and Engineering 12 (2004) 143-157.

[6] M. Song, and R. Kovacevic, Thermal modeling of friction stir welding in a moving coordinate system and its validation, International Journal of Machine Tools & Manufacturing 43 (2003) 605-615.

[7] N. Sato, O. Terada, and H. Suzuki, Adhesion of aluminum to WC-Co cemented carbide tools, Journal of the Japan Society of Powder and Powder Metallurgy 44 (4) (1997) 365-368.

[8] S.F. Miller, P. Blau, and A.J. Shih, Microstructural alterations associated with friction drilling of steel, aluminum, and titanium, Journal of Materials Engineering and Performance 14 (5) (2005) 647-653.

[9] Properties and Selection: Irons, Steels, and High Performance Alloys, 1 (10), Metals Handbook, ASM International, 1990.

[10] Properties and Selection: Nonferrous Alloys and Special-Purpose Materials, 2 (10), Metals Handbook, ASM International, 1990.

# CHAPTER 5.

# TOOL WEAR

## 5.1. Introduction

Figure 5.1 shows the stages in friction drilling a ductile metal, square tube workpiece. First, the tool comes into contact with the workpiece. Then, at the main thrust stage, the tool penetrates the workpiece and high axial force is encountered. The friction force on the contact surface produces heat and softens the work-material. Then, in the material separation stage, the tool penetrates the workpiece and makes a hole. The ductile work-material encompasses the tool. Finally, the tool retracts and leaves a hole with a bushing. Cross sections of several holes friction drilled with a 5.3 mm diameter carbide tool in AISI 1015 carbon steel tube are shown in Fig. 5.2.

Tool wear in friction drilling is a concern because it affects the characteristics and tolerances that are achievable. It is promoted by the high temperature and forces generated in the process. Miller et al. [1] have observed high peaks in the experimentally measured thrust force, torque, and temperature. FSW tool wear was characterized by Fernandez and Murr [2] and Liu et al. [3] for threaded steel and WC-Co tools, respectively. A preliminary study of performance of tool wear for coated and uncoated friction drilling tools has been reported [4]; however, there is a lack of additional published research on the wear of friction drilling tools.

The goals of the current research were to quantify the wear and surface degradation of tungsten carbide tools used in friction drilling of steel using changes in tool shape and mass, to characterize worn tool surface features, and to analyze the surface chemistry of the worn tool tip. Thrust force, torque, and hole inside diameters were also measured as the tool wear progressed.

## 5.2. Experimental setup and wear measurements

### 5.2.1. Machine tool and workpiece

A Milacron Sabre 500 vertical machining center was used for the friction drilling tool wear study. Figure 5.3 shows the drilling setup. The workpiece was fixed with blocks across two vices that provided support in the axial direction to minimize workpiece bowing. Holes were drilled from left to right relative to the view in Fig. 5.3. After each hole was drilled, the tool was indexed 7.6 mm to the right automatically. Depending on the length of the square tube workpiece, 70 to 80 holes could be drilled in each side of the square tube. The spindle speed was 2800 rpm and tool feed rate was 254 mm/min. These are common process parameters for friction drilling of low carbon steel [1,5].

Each hole took about 2.3 s to drill. The time between each hole was set to at least 10 s to allow heat dissipation from the tool because of the high temperature in the process. The maximum temperature generated in friction drilling was measured to be about 1/2 to 2/3 of the melting temperature of the carbon steel workpiece [1] by an infrared camera system. Even higher temperatures are expected at the tool-workpiece interface.

The work-material was AISI 1015 carbon steel, which is a low carbon steel similar to the AISI 1020 steel used in friction drilling experiments in Chapter 2 [1]. The workpiece was square tubing with wall thickness of 1.5 mm, width of 19 mm, and average length of 0.6 m. As shown in Fig. 5.4, square tubing was ideal for drilling many holes because it has four usable, well supported sides.

A Kistler model 9272A piezoelectric drilling dynamometer was used to measure the axial thrust force and torque during the drilling process.

### 5.2.2. Tool geometry and tool wear characterization

A picture and an illustration of the key dimensions of the friction drilling tool are shown in Figs. 5.5(a) and (b), respectively. The tool used in this study has $d$ = 5.3 mm, $\alpha$ = 90°, $\beta$ = 36°, $h_c$ = 0.940 mm, $h_n$ = 5.518 mm, and $h_l$ = 7.043 mm. The cylindrical and conical regions have the trilobular cross-sectional shape. The trilobular geometry decreases the contact area, thrust force, and torque in friction drilling. The tool material

was a cobalt-bonded combination of tungsten carbide and titanium carbide of commercial manufacture and was designed for friction drilling (Formdrill™). A notch, as shown in Fig. 5.5, was ground along the axial direction in the shoulder region of the tool as the angular datum for CMM measurement of tool wear.

Throughout the study, measurements of drilling thrust force, torque, tool weight, and tool profile were conducted after drilling hole numbers 1, 2, 3, 4, 5, 10, 50, 100, 200, 500, 1000, and every thousand holes after that. In total, 11000 holes were drilled and the tool was still performing well at the end of the experiment. After drilling the 9000th hole, scanning electron microscopy and light element energy dispersive X-ray analysis were performed on the tool.

One of the key wear measurements is the change of the tool shape, which was measured using a coordinate measuring machine (CMM) (Legend™, Electronic Measuring Devices). A specially designed tool fixture was built to hold the tool in the shoulder region (Fig. 5.6). The tool was positioned in the fixture with the front of the tool shoulder flush with the front face of the fixture, and the slot was in line with a gap machined into the fixture. The CMM incorporates a scanning measurement head with two probes, marked as Probes 1 and 2 in Fig. 5.6(a). Probes 1 and 2 are made of carbide with 1.0 and 0.7 mm diameter ball tips, respectively. The first step in the measurement was to establish the datum using Probe 1. Probe 1 was programmed to measure the back end of the tool and establish three datum surfaces, marked as the axial, radial, and angular datum in Fig. 5.5(c). As shown in Fig. 5.6(b), Probe 1 first came into contact with the back of the tool shoulder region to establish the axial datum. Probe 1 then traced the shank region of the tool to find the radial datum. Finally, Probe 1 touched around the shoulder region to find the position of the slot for angular datum. These three datum planes do not change during the tool wear test and were the references for precision measurement of small change in tool geometry or the tool wear.

After the datum surfaces were established and the relative location between Probes 1 and 2 remained unchanged, Probe 2 was programmed to perform 12 scans, 30° apart from each other in the angular direction, of the conical and center regions of the tool. The path of these scans was along the axial direction. Figure 5.6(c) shows the Probe 2 of CMM scanning the tool for profile measurement. The tool profile was measured eight

consecutive times on the worn tool to determine repeatability of the measurement. After each measurement the tool was repositioned in the fixture. The standard deviation of the eight measurements was calculated for the radial distance at each axial location on the tool, the area under the tool profile curve, and the distance from each point on the curve to the origin.

The CMM was also used to measure hole sizes. The diameters of the 1st, 5000th, and 11000th hole were measured at three depths (0.46, 1.99, and 4.46 mm from the top of the hole).

## 5.3. Results and observations of tool wear

### 5.3.1. Observations of tool wear by optical microscopy

The trilobular geometry of the tool influenced the tool wear and material adhesion from the workpiece to the tool. Figure 5.7 shows optical micrographs of the conical region of the tool after 2, 1000, 5000, and 11000 drilled holes. The lobe apex is in the center of the tool in each micrograph. In the very early stage of tool wear, as shown in Fig. 5.7(a), the only observation that can be made is the adhesion of work-material to the tool. A patch of wear including circular grooves in the conical region occurs on the lobe apex after drilling 1000 holes, as shown in Fig. 5.7(b). At 5000 holes, as shown in Fig. 5.7(c), this patch area has grown significantly. Figure 5.7(d) shows the patch of wear extending around the tool conical region. Circular grooves around the tool peripheral develop in the area intersecting tool conical and cylindrical regions. These grooves are likely due to the abrasive wear.

### 5.3.2. CMM measurements of tool profile and tool wear

Figure 5.8 shows the tool profile of the new tool and the tool used after drilling the first hole. The profile was measured at 30° in the angular direction from the apex of the trilobular lobe. The evidence of material adhesion on the tool is apparent. The horizontal axis represents axial distance from the axial datum and the vertical axis represents radial position of the tool surface. A 0.045 mm thick raised area along the tool profile can be noticed in Fig. 5.8 because a layer of work-material adhered to the tool surface. As the

lobe plows through the workpiece, the work-material builds up on its front side. The tool profiles are a measure of the balance between tool wear and work-material adhesion to the tool. The continual transfer of work-material between the tool and workpiece will explain the fluctuations in thrust force and torque, to be discussed in Sec. 5.3.6. Along the apex of the trilobular lobe, there was no measurable wear or material deposition after drilling the first hole.

The CMM measured tool profiles of the new tool and tool after drilling 5000 and 11000 holes are shown in Fig. 5.9. The measurement trace was along the apex of trilobular lobe. Wear of the tool after drilling 5000 and 11000 holes can be quantified in Fig. 5.9. Large wear occurs at the tool center region.

Wear was quantified at four locations, marked as A, B, C, and D, in Fig. 5.9. Point A is the radial wear of the tool at the cylindrical region. This wear will affect the hole inner diameters. Point B is the area with significant wear at the intersection of the conical and cylindrical regions. The wear at point B is measured as the maximum distance from a point on the profile of the worn tool to the profile of the new tool. Point C indicates the wear in the middle of the tool center region. The wear is measured as the distance from the profile of the worn tool to the straight line of the new tool profile in the center region. Point D is the wear in the axial direction at the tool tip. The average wear at A, B, C, and D for 12 measured tool profiles are shown in Fig. 5.10. Six data points for every 2000 holes after hole number 1000 are used to illustrate the relative change in tool wear at four representative locations on the tool.

Repeatability tests for the eight measurements of the worn tool were conducted for distance from the origin at A, B, C, and D. Standard deviations at the four points were 1.88, 10.9, 22.8, and 8.14 μm, respectively. Repeatability was adequate compared to the amount of wear at each location. The average standard deviation of overall measurement repeatability of all points results for the radial distance at each axial location on the tool, the area under the tool profile curve, and the distance from each point on the curve to the origin were 11.8, 11.4, and 19.7 μm, respectively.

Wear was the smallest at Point A. The wear was negligible before hole number 3000. It steadily increased to 0.02 mm after 11000 holes. After drilling 1000 and 3000 holes, wear was the largest at Point B, an area with large initial tool wear. The optical

micrograph of tool wear in Fig. 5.7(b) confirms such observation of high tool wear at Point B. Starting from hole number 5000, a clear trend emerged showing increasing wear at the tool tip. The wear at Point C is steady throughout the drilling of 11000 holes, reaching 0.22 mm at the end of tool wear test. The wear at Point D, the drill tip, is slow before hole number 5000. The wear rate at Point D increases rapidly after drilling 7000 holes. After drilling 11000 holes, the wear at A, B, C, and D is 0.0256, 0.129, 0.231, and 0.297 mm, respectively. It should be noted that the center region supports the drill and generates the peak force in the process [1]. As shown in the profile in Fig. 5.9 and optical micrograph in Fig. 5.7, shape of the center region was worn from a cone to a funnel shape with concave cross-sectional profile after drilling 5000 and 11000 holes. The drill tip becomes sharper and, as a result, will generate lower peak thrust force in friction drilling. This will be discussed in Sec. 5.3.6.

### 5.3.3. Tool weight

Figure 5.11 shows results of the weight measurements during the tool wear study. The weight ultimately changed from 17.388 g for new tool to 17.299 g after 11000 holes, which indicates a decrease of 0.089 g. After drilling the first hole, the tool weight actually increased to 17.399 g. The increase of 0.011 g was due to material adhesion from the workpiece to the tool. It should be noted that every weight measurement was a balance of the loss due to tool wear and the gain due to work-material transferred to the tool. After drilling 100 holes, the weight of tool started to drop due to tool wear.

The change of tool weight for every 1000 holes is also shown in Fig. 5.11, labeled tool weight loss, scaled with the right Y axis. The general trend was increasing tool weight loss which peaked at 12 mg per 1000 holes from hole number 5000 to 6000. Inexplicably, after this peak the trend changed to decreasing tool weight loss. Change of tool weight was 7 mg per 1000 holes from hole number 10000 to 11000. The decreasing wear rate is likely due to the increase of contact area, as shown in the optical micrographs in Fig. 5.7(d). The increase of work-material deposition to the tool because of changing geometry of the worn tool is also a possible reason. Further study is needed to investigate this phenomenon.

### 5.3.4. Scanning electron microscopy

An SEM image of the tool tip after drilling 9000 holes is shown in Fig. 5.12(a). The tool outer diameter near the bottom of the figure is about 5.3 mm. In the tool tip (center region), the funnel shape and circular grooves can be seen. The conical region has formed a rough, serrated appearance due to the different forms of wear. Lower in Fig. 5.12(a), the cylindrical region can be seen with little evidence of wear or use.

The result of element detection by light element EDS X-ray for new tool and tool after drilling 9000 holes is shown in Figs. 5.12(b) and (c), respectively. It should be noted the relative height or electron count of each element is not directly quantitative. W, C, Ti, and Co, as shown in Fig. 5.12(b), are elements that comprise the WC, TiC, and Co binder of the tool and are expected. Tool elements and deposited elements from the workpiece of C, Fe, and Mn are also present in Fig. 5.12(c), confirming material transfer from the workpiece to the tool. The Co cannot be seen in the graph because of the larger Fe peak. The O is present due to high temperature oxidation in the friction drilling process, and is evidence of oxidation wear. SEM microscopy and the chemical analysis information suggested that a combination of adhesive, oxidative, and abrasive wear contributes to friction drilling tool wear.

### 5.3.5. Hole inner diameters

An important effect of tool wear is the dimensional alteration of friction drilled holes. The hole becomes too small when it cannot be tapped or utilized with the intended M6 fastener for the 5.3 mm diameter hole drilled in this study. The CMM was used to measure inner diameter of hole numbers 1, 5000, and 11000 at three depths, 0.46, 1.99, and 4.46 mm from the top of the hole, for comparison. Figure 5.13 shows the measured hole diameters. A general trend of reducing hole diameter is observed. Near the top of the hole, the diameter was reduced by about 0.09 mm. Almost no change is tool diameter occurred in the middle of the hole (1.99 mm from the top of the hole). Small change in diameter near the top of the hole is because of the lack of wear in the cylindrical region. An important observation in this study is that, even with the tool worn in the center and conical regions, the hole diameter is largely determined by the tool cylindrical region,

which does not exhibit a significant wear. Therefore, the hole diameter in the top of the hole, where connects to the thin workpiece, does not change drastically.

The most notable change in diameter between hole numbers 1 and 11000 is 0.29 mm, which is near the bottom of the bushing at a depth of 4.46 mm. The wear in the tool conical region causes the decrease in hole diameter. The 0.13 mm wear at Point B, as shown in Figs. 5.9 and 5.10, matches well with half of the 0.29 mm diametrical reduction of the hole.

### 5.3.6. Thrust force and torque

The measured thrust force and torque for friction drilled hole numbers 1, 2, 4000, and 11000 are shown in Fig. 5.14. These hole numbers were chosen to demonstrate the effect of tool wear on drilling process. The horizontal axis represents the time and distance of tool travel from the initial contact between tool and workpiece. General shapes of force and torque are similar to those described in Chapter 2 [1]. The secondary peaks in thrust force and torque after hole drilling can be identified. After penetration, the shoulder of the tool, which is marked in Fig. 5.5(b), contacted the back-extruded work-material and created the secondary peak [1]. Maximum peak forces were 1600, 2100, 1700, and 1400 N for holes 1, 2, 4000, and 11000, respectively. After drilling the first hole, the force increased significantly in the second and following holes. This is likely due to the adhesion of work-material on the tool, as shown in Figs. 5.7(a) and 5.8, which increased the size of the tool and changed the frictional contact interaction between the tool and workpiece. The first hole was drilled with carbide tool sliding on steel workpiece. Every hole after that was a combination of carbide tool, transferred steel work-material, and possibly an oxide layer sliding on steel workpiece. No clear trend on the effect of tool wear in torque can be seen. The reason for this is thought to be the varying frictional contact condition from hole to hole.

The peak thrust force decreased at later stages of tool wear, as shown in Fig. 5.15. This surprising observation was credited to the change of tool tip geometry, as shown in Fig. 5.9 after drilling 11000 holes. The worn tool tip is sharp with the concave cross-sectional shape in the center region. This self-sharpening tool tip in friction drilling and the reduction in peak thrust force was an interesting phenomenon caused by the tool wear

in friction drilling. The peak thrust force was the lowest at the end of the 11000 hole test. At about 5000 holes, the peak thrust force became smaller than that of the first hole.

### 5.4. Friction drilling tool wear mechanisms

Microscopy of the tool surface, augmented by energy dispersive X-ray analysis, suggest that adhesive, oxidative, and abrasive wear all occur to some extent during friction drilling; however, it is difficult to determine their proportional contributions [6]. They are described in their proposed order of importance; namely,

- Adhesive wear. In friction drilling, most material transfer is observed to be from the workpiece to the tool. Work-material adhesion to the tool during machining is a familiar phenomenon [7]. Due to the high temperature of the process, the Co matrix in the tool material will soften, be removed from the tool, and lose hard WC particles embedded in the matrix. Adhesive wear arises from the strong adhesive forces created whenever atoms come into intimate contact. When these adhesive forces are greater than the shear strength of either bulk material, a break is likely within one of the materials [8].
- Oxidative wear. Oxygen was detected on the tool by EDS X-ray. High temperature increases potential for oxidation in normal atmospheric air. Oxidative wear is a form of corrosive wear in which reaction with oxygen produces an oxide layer on the surface of the tool. The removal rate and wear of the oxide layer are important to determine the contribution of oxidative wear.
- Abrasive wear. The circular grooves in the tool conical and center regions suggested abrasive wear. This is the form of wear which occurs when the hard particles of WC, that were dislodged due to adhesive wear, slide on the surface of the tool and plough grooves into it. This is the three-body wear with the three bodies being the tool, workpiece, and dislodged WC particles.

## 5.5. Conclusions

The wear of a friction drilling tool was minimal after producing 11000 holes in a low carbon steel workpiece. The hard carbide tool proved to be durable compared to previous estimates of 5000-10000 holes. Precise measurements of tool dimensions indicated that the wear was concentrated at the tool center region and at the intersection between the conical and cylindrical regions. The tool tip self-sharpened during friction drilling, which reduced the thrust force as tool wear progressed. The torque did not display any obvious changes at different stages of tool wear.

Adhesive, oxidative, and abrasive wear all occur to some extent during friction drilling; however, it is difficult to determine their proportional contributions. The relative influence of these wear modes, especially those associated with diffusion wear, may change as the tool continues to wear out.

The current results suggest further investigation. Additional investigation of tool wear rates and mechanisms is needed for larger numbers of tools, and with larger numbers of holes drilled in order to establish ultimate tool failure modes. The tribological aspects of changing frictional contact conditions due to transfer of work-material to the tool need clarification. Diffusion wear is thought to occur from chemical reactions in the contact zone between the tool and the workpiece, especially at elevated temperatures, but no direct evidence for this phenomenon was found in this study.

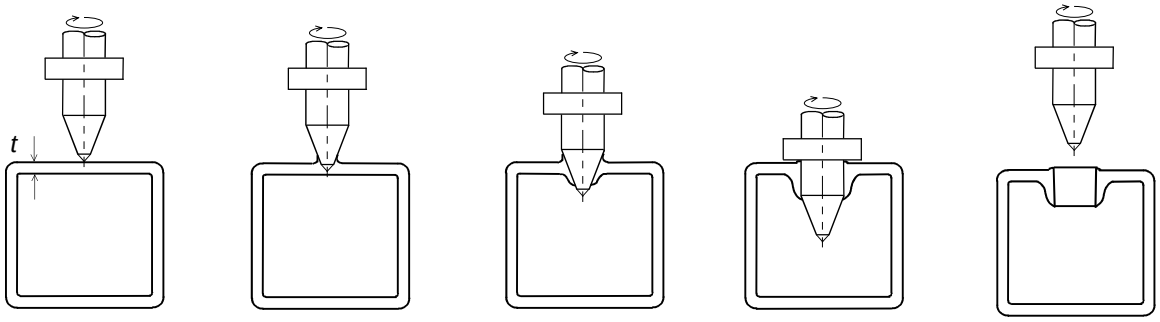


Figure 5.1. Stages of friction drilling in a square steel tube.

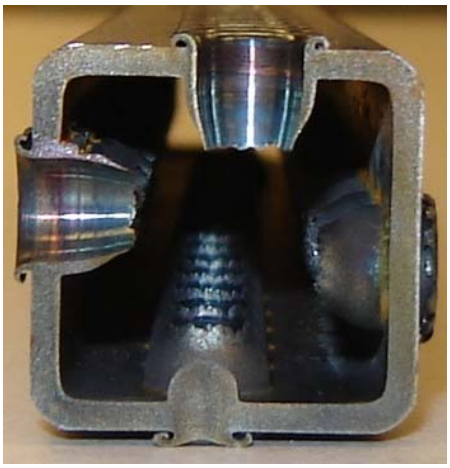

Figure 5.2. Cross section of friction drill holes in AISI 1015 steel tube.

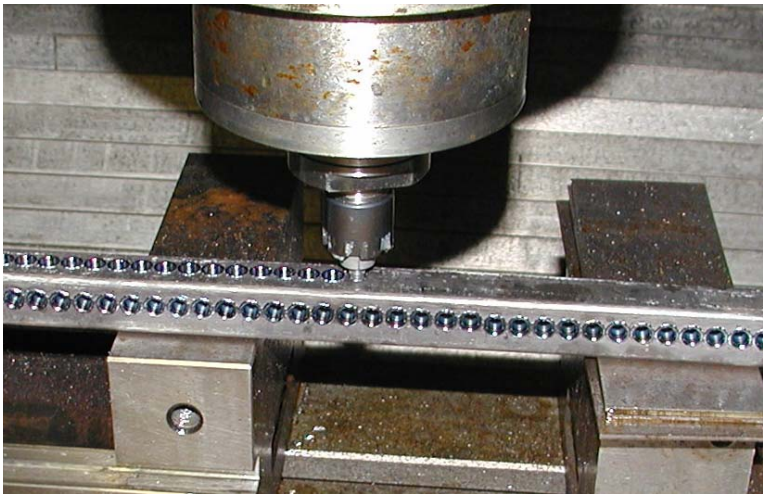

Figure 5.3. Setup for friction drilling of carbon steel square tube.

Figure 5.4. Close up view of square tube workpiece after friction drilling tool wear test.

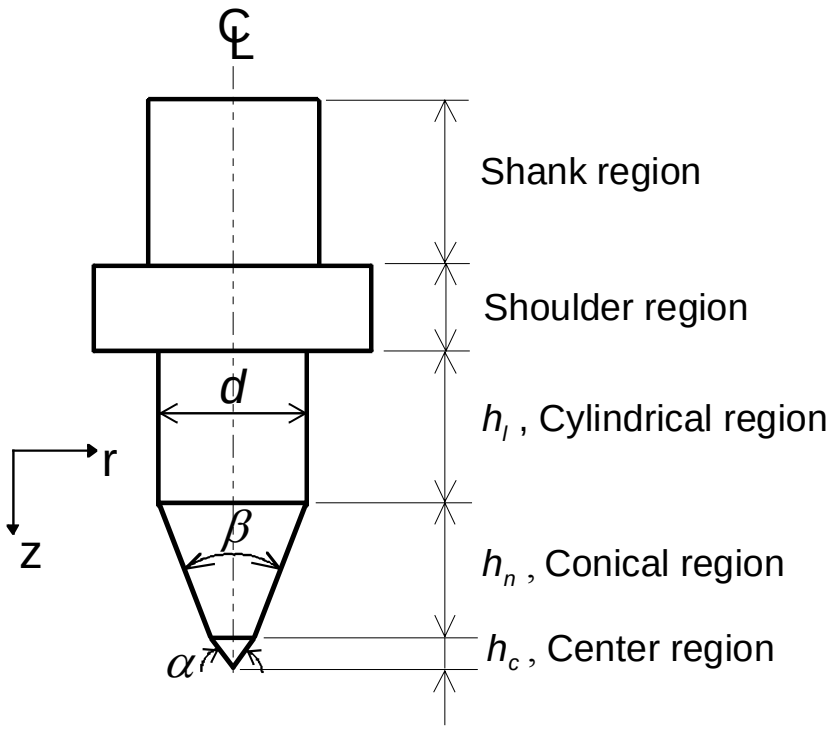


(a) (b)

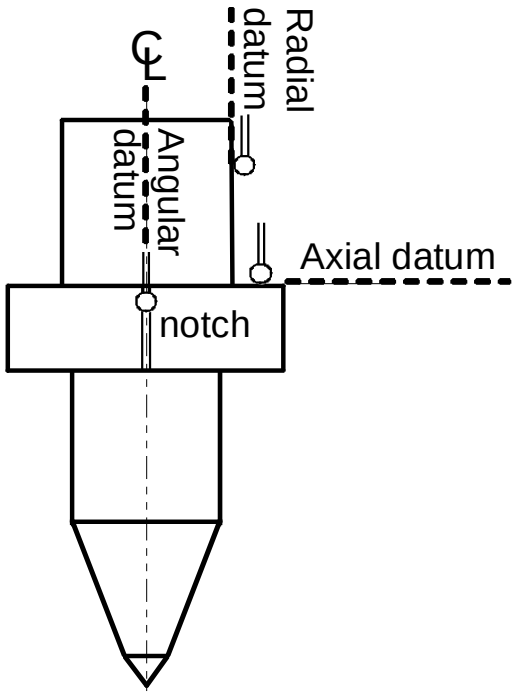


(c)

Figure 5.5. Friction drill tool: (a) picture of the tool, (b) illustration of regions in the tool and key dimensional parameters, and (c) three reference datum for CMM measurement.

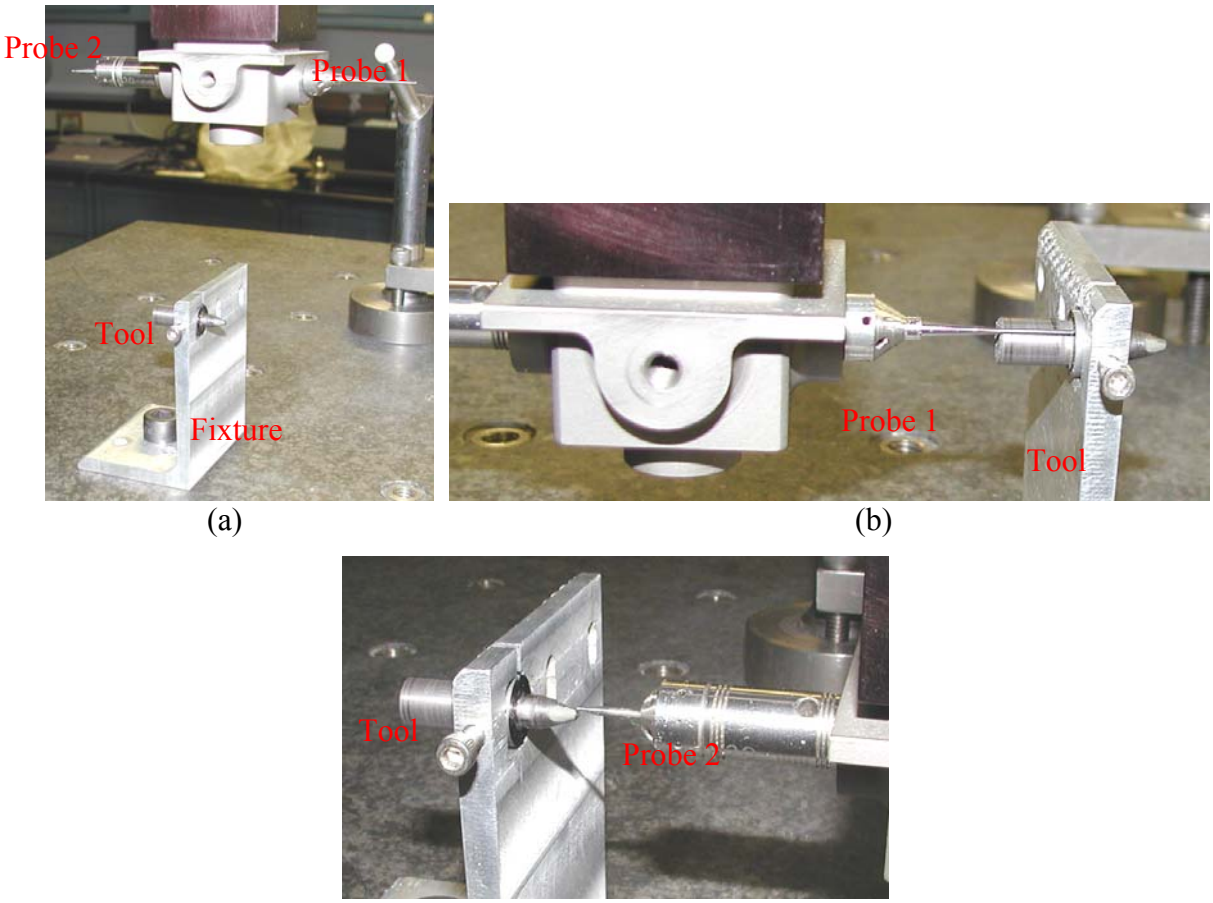


Figure 5.6. CMM for tool wear measurement: (a) tool, tool holder, and CMM scanning head with probes 1 and 2, (b) probe 1 measuring the axial datum, and (c) probe 2 performing axial scanning of the tool conical region.

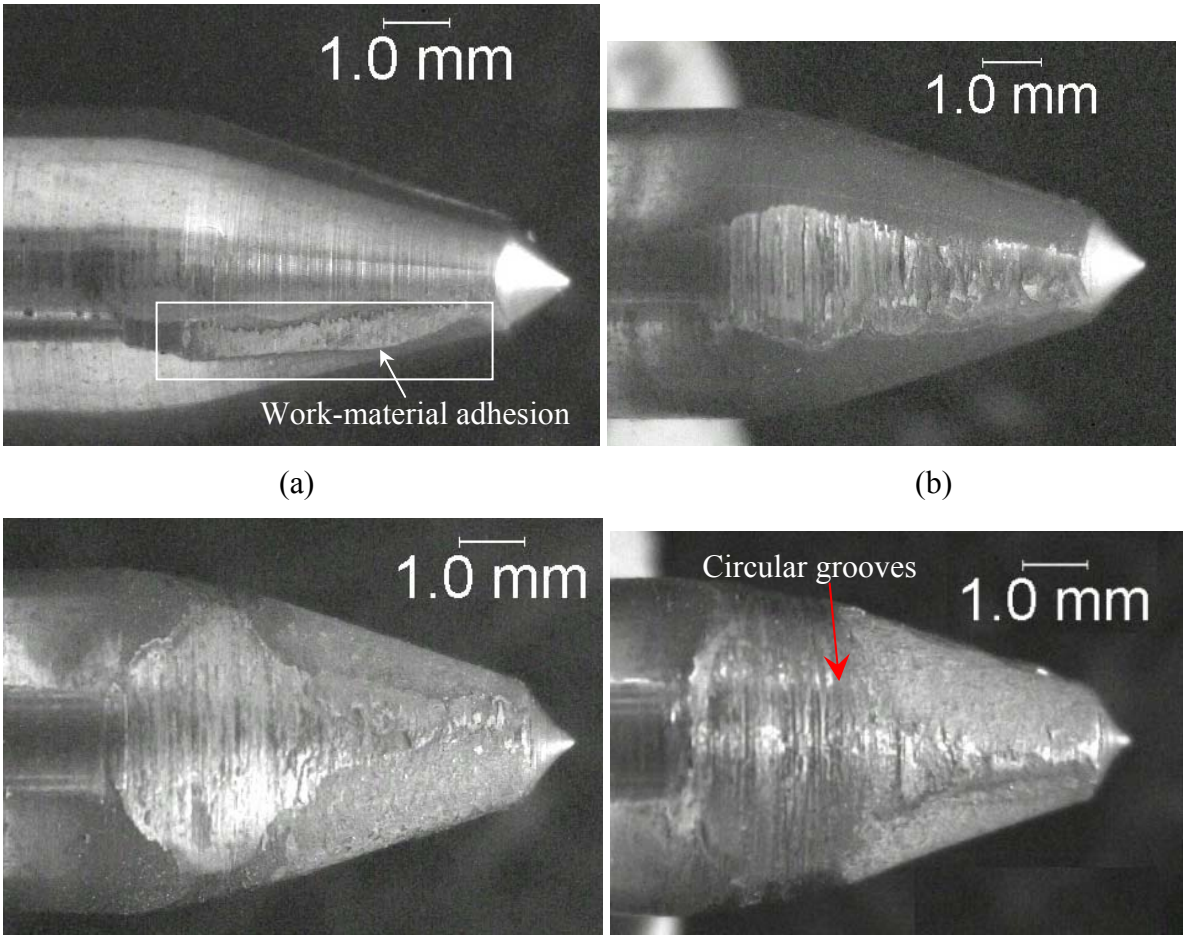


Figure 5.7. Optical micrographs of friction drilling tool after: (a) 2, (b) 1000, (c) 5000, and (d) 11000 holes.

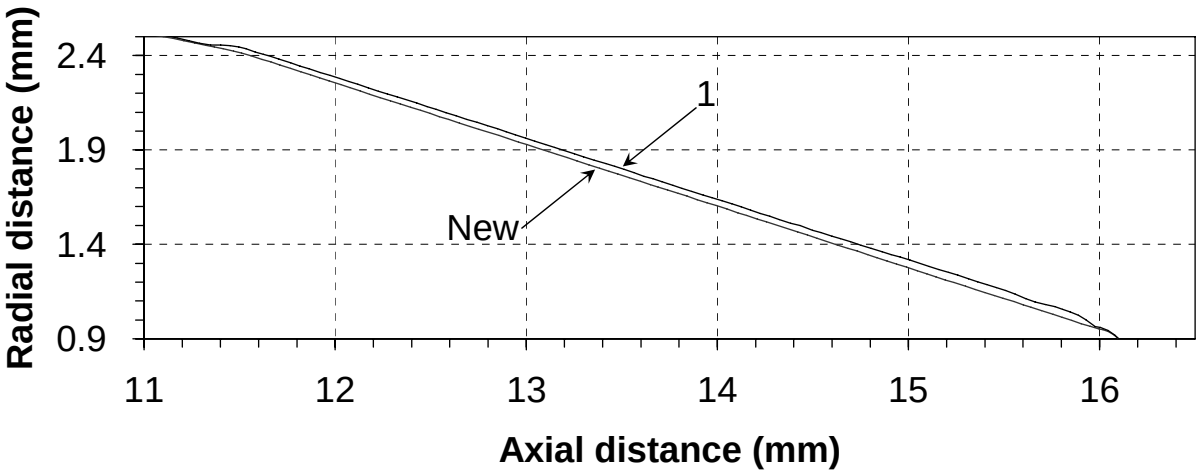


Figure 5.8. CMM profiles of unused tool and after drilling one hole showing buildup of work-material on the tool.

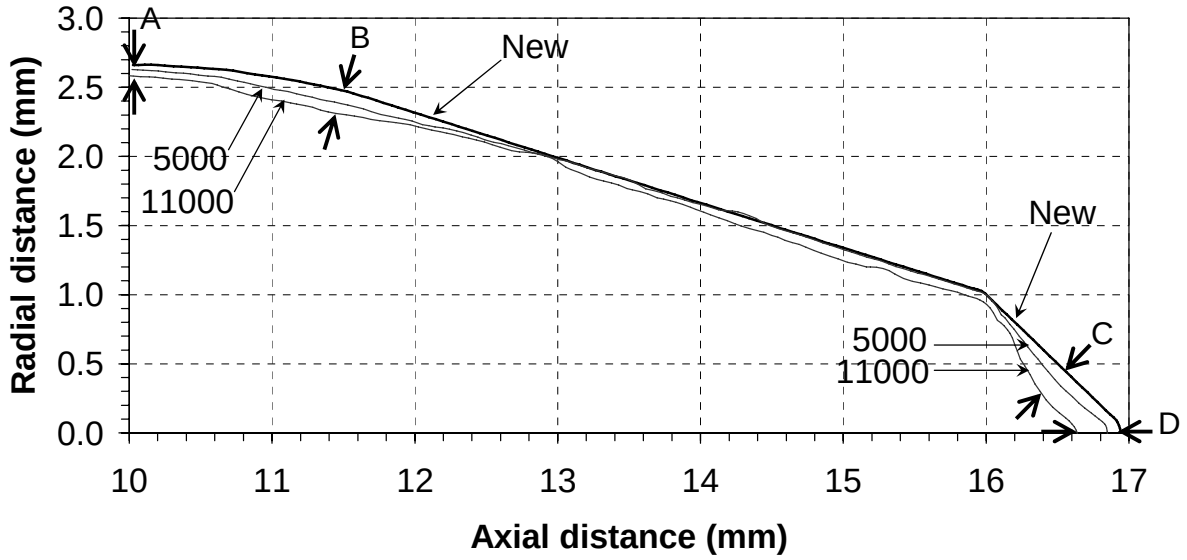


Figure 5.9. Comparison of CMM measured profiles on the lobe apex of the new tool and tool after drilling 5000 and 11000 holes.

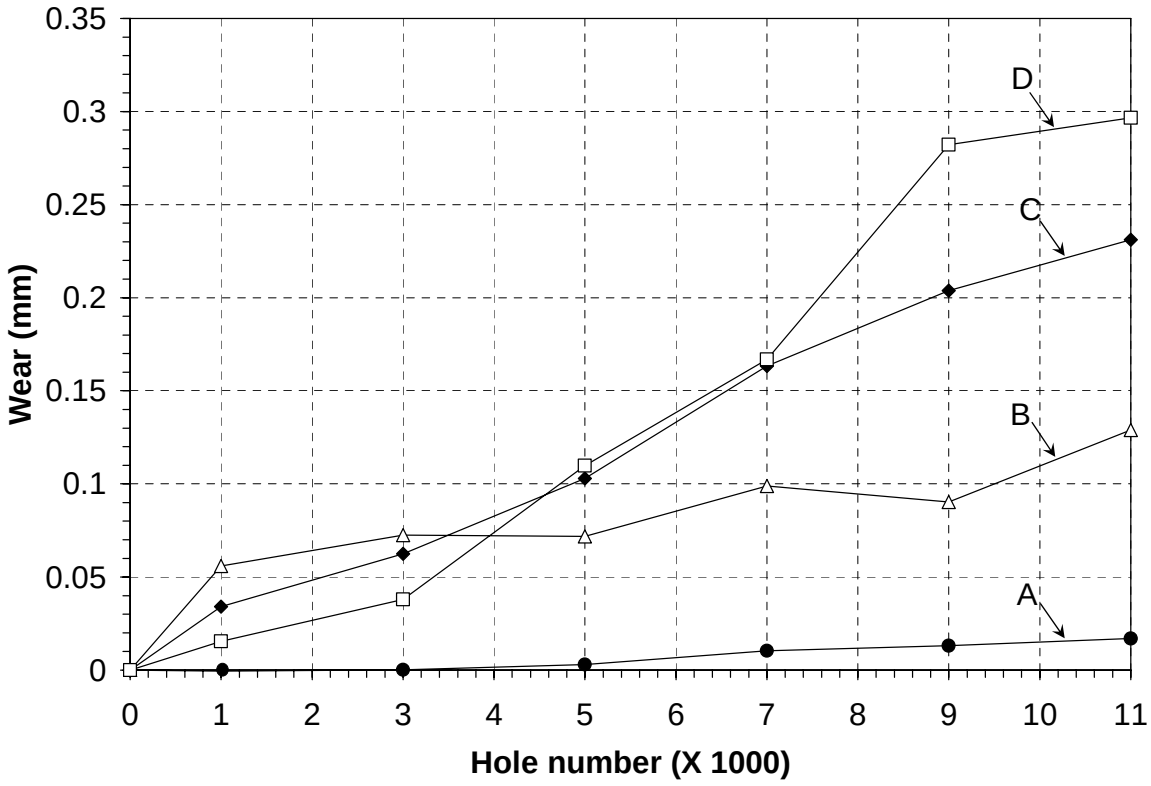


Figure 5.10. Tool wear at A, B, C, and D in Fig. 5.9.

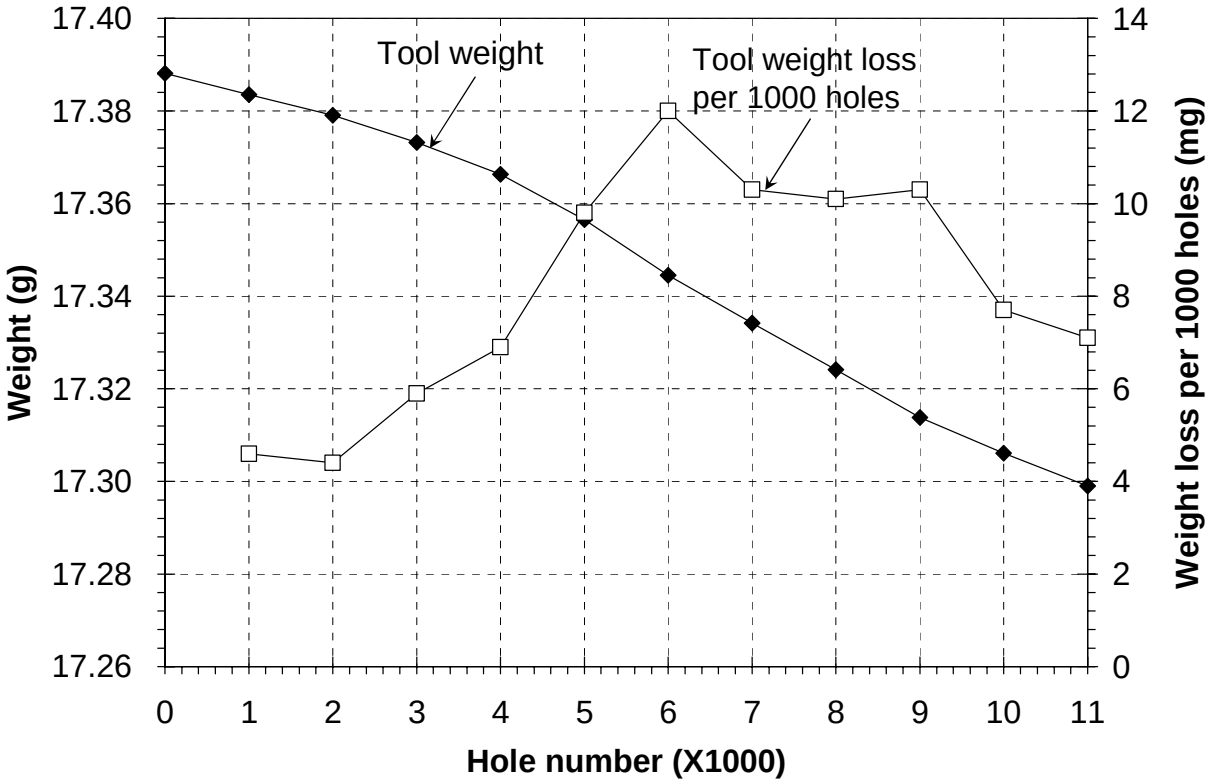


Figure 5.11. Tool weight and weight loss at different stages of tool wear.

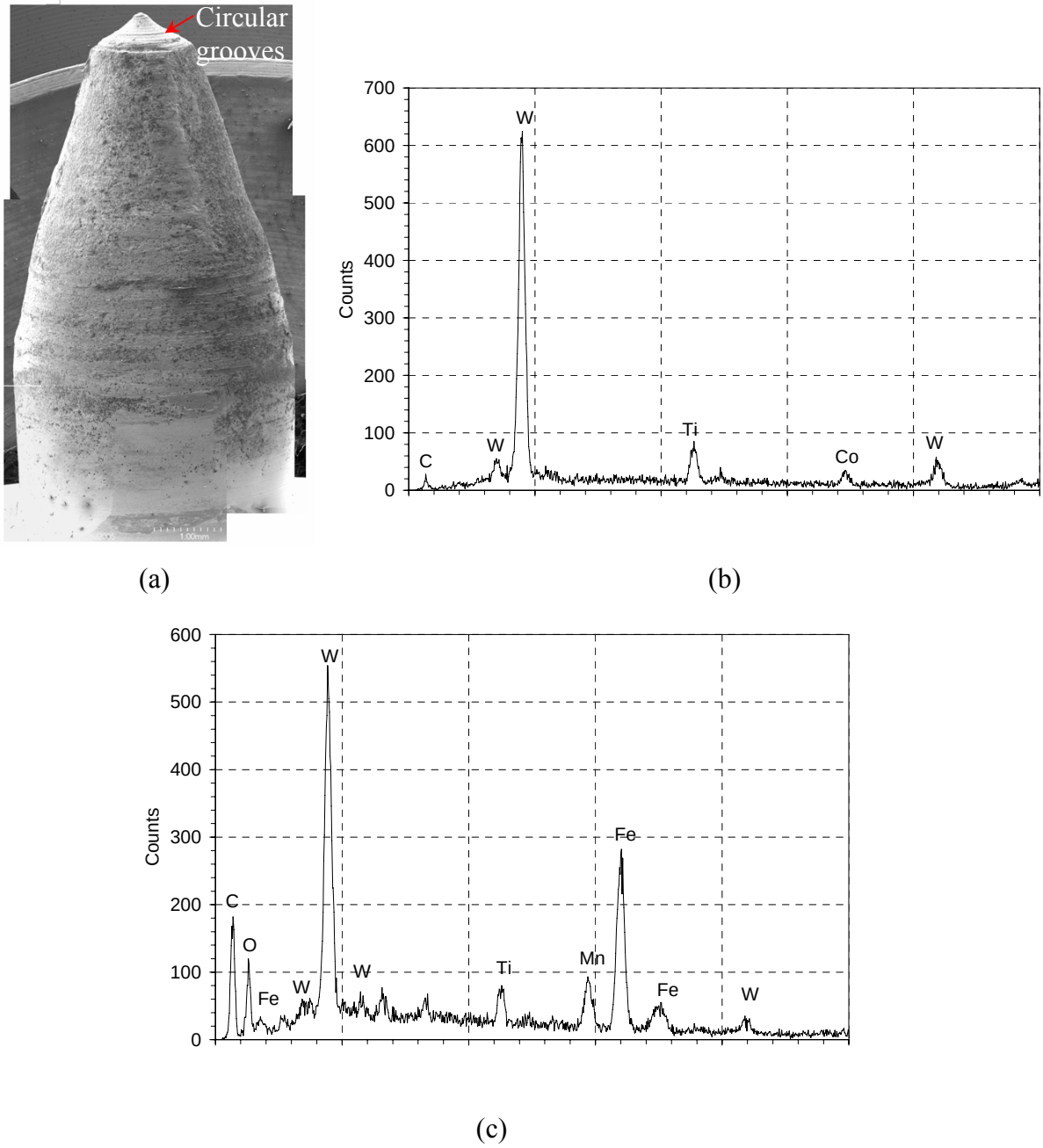


Figure 5.12. SEM characterization of friction drilling tool: (a) SEM micrograph of the tool center and conical regions and EDS analysis of elemental composition of the tool surface for (b) new tool and (c) tool after 9000 drilled holes.

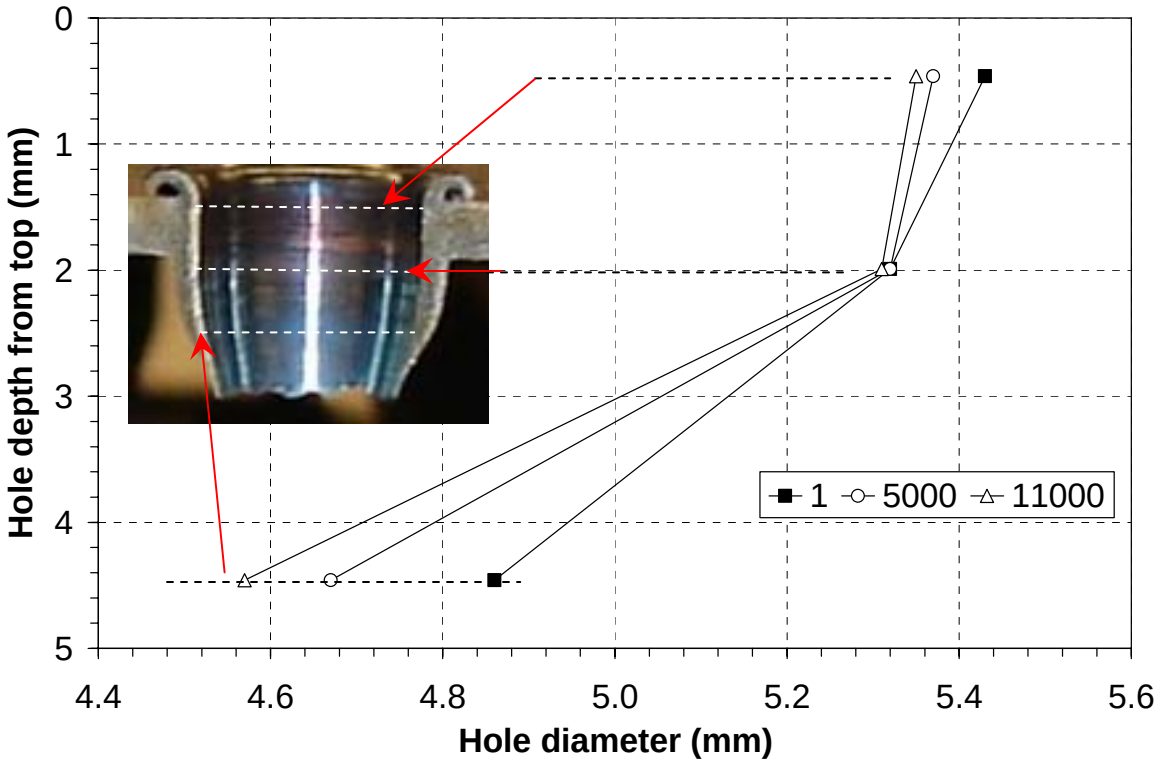


Figure 5.13. Hole diameter at hole depths of 0.46, 1.99, and 4.46 mm for hole numbers 1, 5000, and 11000.

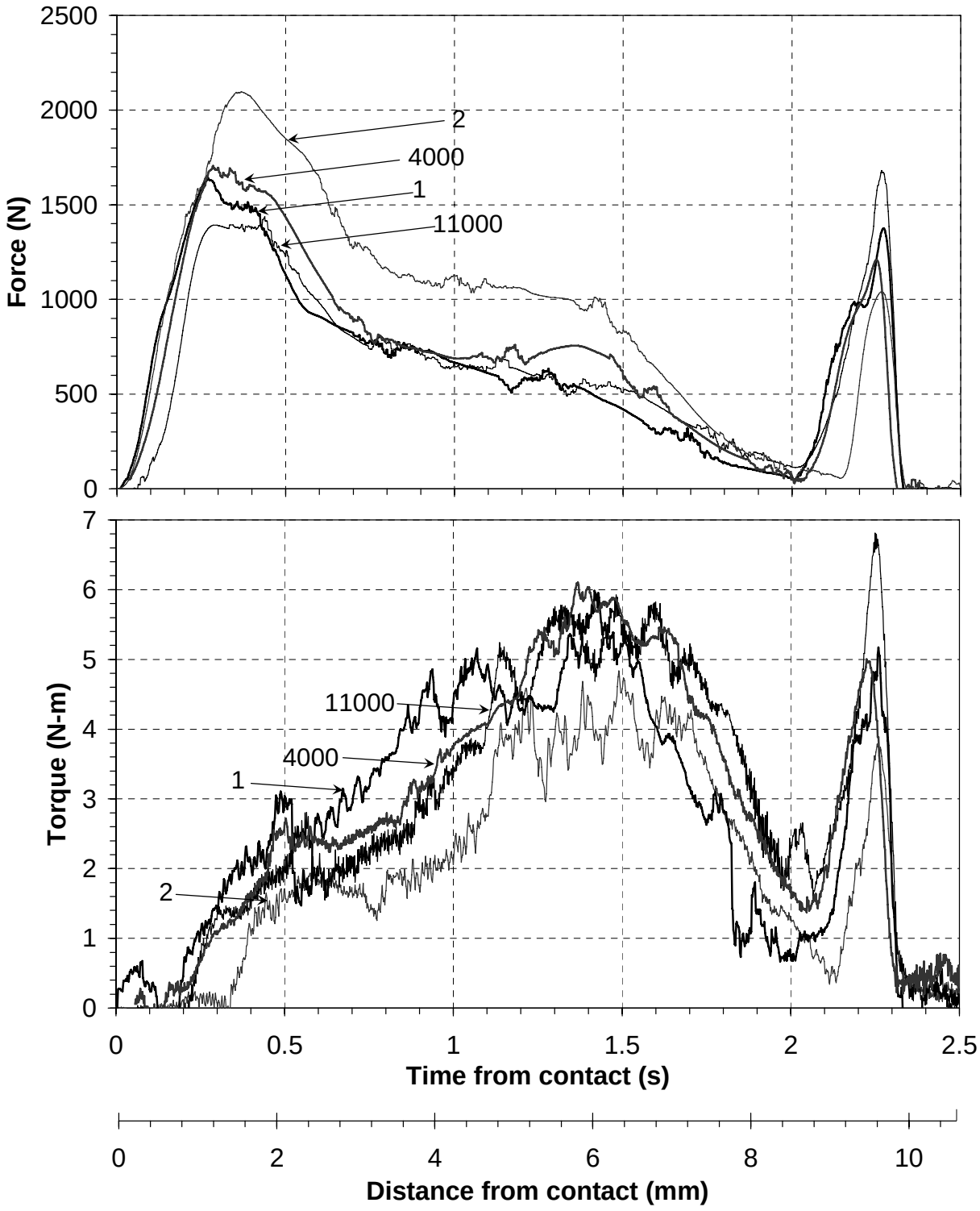


Figure 5.14. Thrust force and torque of hole numbers 1, 2, 4000, and 11000.

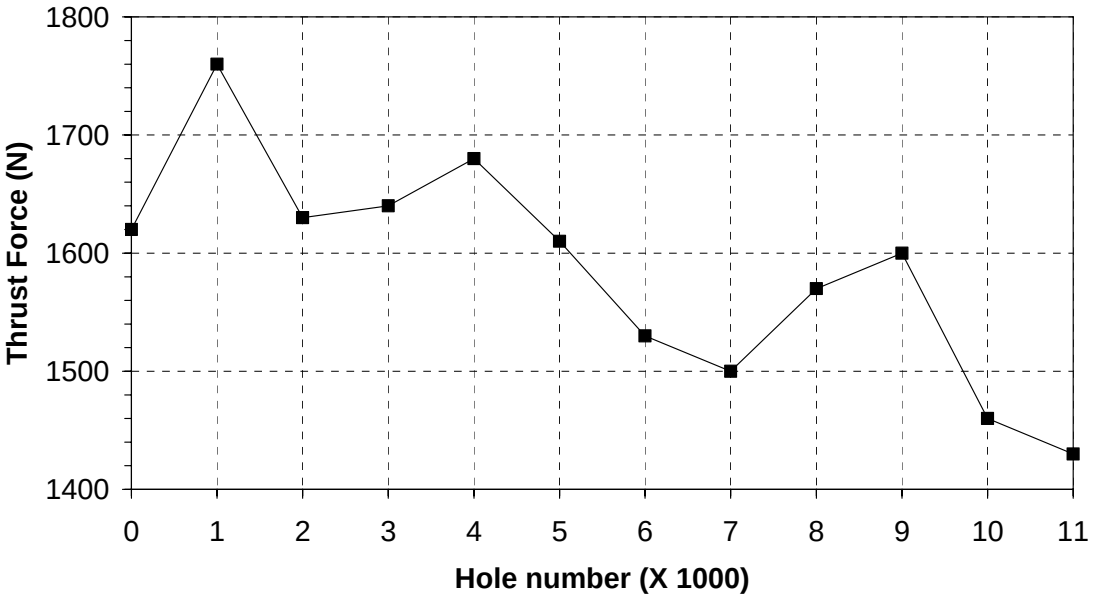


Figure 5.15. Peak thrust force at different stages of tool wear.

## References


[1] S.F. Miller, H. Wang, R. Li, and A.J. Shih, Experimental and numerical analysis of the friction drilling process, Journal of Manufacturing Science and Engineering (accepted) (2004).

[2] G.J. Fernandez and L.E. Murr, Characterization of tool wear and weld optimization in the friction-stir welding of cast aluminum 359+20% SiC metal-matrix composite, Materials Characterization 52 (2004) 65-75.

[3] H.J. Liu, J.C. Feng, H. Fujii, and K. Nogi, Wear characteristics of a WC-Co tool in friction stir welding of AC4A+30 vol% SiCp composite, International Journal of Machine Tools & Manufacture 45 (2005) 1635-1639.

[4] M. Kerkhofs, M.V. Stappen, M. D'Olieslaeger, C. Quaeyhaegens, and L.M. Stals, The performance of (Ti,Al)N-coated flowdrills, Surface and Coatings Technology 69/69 (1994) 741-746.

[5] S.F. Miller, P. Blau, and A.J. Shih, Microstructural alterations associated with friction drilling of steel, aluminum, and titanium, Journal of Materials Engineering and Performance 14 (5) (2005) 647-653.

[6] B. Bhushan, Modern Tribology Handbook: Principles of Tribology, vol. 1, CRC Press, Boca Raton, Florida, 2001.

[7] N. Sato, O. Terada, and H. Suzuki, Adhesion of aluminum to WC-Co cemented carbide tools, Journal of the Japan Society of Powder and Powder Metallurgy 44 (4) (1997) 365-368.

[8] E. Rabinowicz, Friction and Wear of Materials, John Wiley and Sons Inc., NY, 1965.

# CHAPTER 6.

# ANALYTICAL AND FINITE ELEMENT MODELING OF THE FRICTION DRILLING PROCESS

## 6.1. Introduction

Figure 6.1 shows the cross-sectional pictures of the deformed workpiece and tool at four stages in friction drilling a hole on 1.6 mm thick aluminum 6061. In Stage 1, the conical tool comes into contact with the workpiece. In Stage 2, the tool is close to penetrate the workpiece. The thrust force is typically at its peak and the back extrusion of work-material can be seen at this stage. Stage 3 shows the ductile work-material encompasses the tool tip. The extrusion of material sideward to form a bushing can be identified. This is the tool location with the maximum torque in drilling. As the tool penetrates the workpiece in Stage 4, the bushing of the 5.3 mm diameter hole is formed. Some work-material is back extruded at the entry of the hole.

The analytical model for thrust force and torque is developed to predict the thrust force and torque generated during the friction drilling process based on the pressure and area of contact between the tool and workpiece. The high temperature in friction drilling changes material properties. The force model applies the experimentally measured temperature to predict the yield stress and contact pressure between the tool and workpiece and to calculate the thrust force and torque.

The work-material deformation is severe and both the tool and workpiece temperatures are high in friction drilling [1]. Modeling is a necessary tool to understand the material flow, temperatures, stresses, and strains, which are difficult to measure experimentally during friction drilling. The analytical model model is simple but not able to provide detailed analysis of the work-material deformation. This can be overcome by using the thermo-mechanical FEM for modeling the high temperature, large strain, and

large deformation of the work-material in friction drilling. This research effort is still lacking and becomes the goal of this study.

FEM has been applied to simulate friction stir welding (FSW), a process similar in concept to friction drilling. In FSW a rotating tool is used to generate frictional heat and stir the work-material around the tool to join two parts. The only significant difference is that friction drilling displaces work-material to form a specific shape, while FSW mixes and welds work-material. Spot friction welding (SFW) or friction stir spot welding (FSSW) is a FSW process to join two sheet metals in one spot [2]. This process is very similar to the friction drilling. Both processes have the rotating tool feeding in the axial direction. There is a lack of research in modeling of friction drilling process. However, extensive research in FEM modeling of FSW, SFW, and FSSW are available and become the base of this study.

Research in modeling of FSW has been reviewed by Chao et al. [3], Schmidt and Hattel [4], and Soundararajan et al. [5]. Modeling of SFW has been conducted by Awang et al. [6] and Kakarla et al. [7] used the ABAQUS/Explicit FEM code. The modeling of SFW is expanded in this research to investigate the friction drilling process.

In this study the ABAQUS/Explicit finite element code was developed to simulate the thermo-mechanical response in friction drilling. The 3D model was chosen because the 2D axisymmetric model was unable to simulate work-material flow in the rotational direction. Modeling results will show significant flow in the rotational direction, particularly close to the contact area with the tool. The explicit method was well-suited to solve high-deformation events that require many small increments to obtain an accurate solution [8]. In this study, three FEM techniques, adaptive meshing, element deletion, and mass scaling, were required to enable convergence and completion of the simulation, due to the large work-material deformation in friction drilling. Adaptive meshing and element deletion by plastic strain criterion were necessary to maintain the mesh quality of the workpiece with large deformation. Mass scaling is applied to increase computer efficiency of the explicit method. The material deformation between the high speed rotating tool and workpiece was modeled using the explicit FEM method. The friction heat generation and heat partition were implemented. A coupled thermo-

mechanical analysis was performed with temperature-dependent thermal and mechanical properties of the work-material.

In the next section, the analytical model is first described and compared to experimental results. Then, the finite element simulation of the friction drilling process is introduced. Next, the experimental setup and validation by comparison of theoretical and experimental thrust force, torque, and temperature is presented. Finally, FEM analysis outputs and conclusions are discussed.

## 6.2. Review of friction modeling

A wide range of coefficients of friction by Coulomb's friction law have been applied in FSW and SFW modeling. The coefficient of friction as high as 2.0 has been used in analytical modeling of FSW [9], taken from previously experimentally measured values. Soundararajan et al. [5] in FEM modeling of FSW assumed the coefficient of friction ranging from 0.4–0.5 based on surface temperature and contact between tool and workpiece. Schmidt and Hattel [4] and Buffa et al. [10] in FEM modeling of FSW had constant coefficient of friction of 0.3 and 0.46, respectively. In SFW FEM modeling by Awang et al. [6], the coefficient of friction was temperature dependent and ranging from 0–0.62. This model extrapolated between the published value of 0.62 from Serway [11] and 0 at the work-material melting temperature. Chao et al. [3] in FEM modeling of FSW used an inverse method for friction to match experimental and modeling results for temperature, similar to the method in this study.

In this study, the Coulomb friction model was applied. This is not the best friction model for friction drilling. However, a comprehensive friction model and associated input for machining and friction drilling are lacking.

## 6.3. Analytical thrust force and torque modeling

A model, based on the pressure and contact area between the tool and workpiece, is established to predict the thrust force and torque in friction drilling. Two elemental

shapes used to model the contact area, as shown in Fig. 6.2, are the tapered cylinder and straight cylinder.

As shown in Fig. 6.2(a), the shape of tapered cylinder is defined by three parameters: two heights, $h_1$ and $h_2$, and an angle, $\theta$. This angle $\theta$ can be either $\alpha$ or $\beta$, depending on the center or conical contact region of the tool (Fig. 5.5(b)). A uniform pressure $p$, which can be estimated by the yield stress of the rigid-plastic work-material at a given temperature, is acting on the surface. Two coefficients of friction, $\mu$ and $\mu_a$, are defined to calculate forces in the radial and axial directions. In the radial direction, the workpiece is sliding on the fast rotating tool surface at surface speed of 1530 mm/s without lubricant. As investigated by friction stir welding [12], this results in a relatively high $\mu$. In the axial direction, the tool is penetrating the workpiece at very slow speed of 4 mm/s. The $\mu_a$ is expected to be lower than $\mu$.

Equations for thrust force and toque in the tapered cylinder area (Fig. 6.2(a)) with an inclusion angle $\theta$ can be derived as:

$$F = \int_{h_1}^{h_2} p \sin\frac{\theta}{2} dA + \int_{h_1}^{h_2} \mu_a p \cos\frac{\theta}{2} dA = \pi p (h_2^2 - h_1^2) \tan^2\frac{\theta}{2} + \mu_a p \pi (h_2^2 - h_1^2) \tan\frac{\theta}{2} \quad (1)$$

$$T = \int_{h_1}^{h_2} \mu p r dA = \frac{2\pi\mu p (h_2^3 - h_1^3) \tan^2\frac{\theta}{2}}{3\cos\frac{\theta}{2}} \quad (2)$$

In the straight cylinder area, the thrust force and torque are:

$$F = 2\pi\mu_a p R h_3 \quad (3)$$

$$T = 2\pi\mu p R^2 h_3 \quad (4)$$

Three assumptions are made to simplify the force model:

1. The tool is perfectly sharp at the tip and all corners. Five parameters that define the perfect tool in Fig. 5.5(b) are $h_c$, $h_n$, $h_l$, $\alpha$, and $\beta$.
2. The deformation of the workpiece is negligible.

3. The coefficients of friction are independent of temperature and speed and do not change during the friction drilling process.
4. No displaced work-material contributes to the force modeling, i.e., only the overlapping area between the tool and undeformed steel sheet is used in the force modeling. This assumption can be justified by the experimental observations that, as shown in Fig. 6.3, a blue color strip inside the friction drilled holes is always along the region where the tool contacts the original unformed workpiece. The blue color indicates high temperature and more active contact. The work-material, after being displaced by the rotating tool, is hot. It deforms easily and does not create significant resistance to the deformation.

The contact between the double angle friction drilling tool shown in Fig. 5.5(b) and the undeformed workpiece sheet are divided into six stages, as shown in Fig. 6.4. Figure 6.4 shows the geometrical illustrations of different overlapping area between the tool and workpiece during the six stages of friction drilling. The distance of tool travel in the axial direction is designated as $h$.

Stage 1: Only the center region is contacting the workpiece. As shown in Table 6.1, $h_1 = 0$ and $h_2 = h$ for the center region in Stage 1.

Stage 2: Both the center and conical regions are contacting the workpiece. In the center region, $h_1 = 0$ and $h_2 = h_c$, i.e., the whole center region remains inside the workpiece. For the tool and workpiece used in this study, the thickness of the worpiece, $t$, is larger than the height of center region, $h_c$. In the conical region, $h_1 = h_c + h^*$ and $h_2 = h + h^*$, where $h^*$ is an offsetting height, as illustrated in Fig. 6.5, to calculate heights $h_1$ and $h_2$ for the conical region. The $h^*$ can be derived as:

$$h^* = h_c \frac{\tan(\frac{\alpha}{2})}{\tan(\frac{\beta}{2})} - h_c \tag{5}$$

Stage 3: The center region has penetrated through the workpiece and $h_1 = h - t$ and $h_2 = h_c$. In the conical region, $h_1 = h_c + h^*$ and $h_2 = h + h^*$.

Stage 4: Only the conical region with $h_1 = h - t + h^*$ and $h_2 = h + h^*$ is in contact with the workpiece.

Stage 5: Both the conical and cylindrical regions are in contact with the tool. In the conical region, $h_1 = h - t + h^*$ and $h_2 = h_c + h_n + h^*$. In the cylindrical region, $h_3 = h - h_c - h_n$.

Stage 6: Only the cylindrical region is in contact with the workpiece and $h_3 = t$.

In summary, the input of the model includes: 1. tool geometry ($h_c$, $h_n$, $h_l$, $\alpha$, and $\beta$), 2. workpiece geometry ($t$), 3. work-material temperature-dependent stress-strain properties, 4. coefficients of friction ($\mu$ and $\mu_a$) and 5. tool travel from contact ($h$). The output of the model is the thrust force and torque. Effects of the strain-rate, deformation of the workpiece, and tool wear are not considered.

## 6.4. Comparison of analytical modeling results to experimental measurements

The friction drilling experiment conducted in Sec. 2.3 is modeled numerically. The measured maximum workpiece temperature in Fig. 2.6 is used in the temperature-dependent stress-strain relations, obtained from [13], to determine the yield stress at each point in the model. The yield stress is used to represent the pressure $p$. In this study, $\mu$ is set at 2.0, which is adopted from the value in friction stir welding [9]. The high coefficient of friction between the fast rotating tool and the stationary workpiece is reasonable since no lubricant was used. The $\mu_a$ is set at 0.4.

The thickness of the workpiece, $t$, is 1.19 mm. Based on Eq. (5), $h^* = 2.015$ mm. Values for range of tool travel and the $h_1$, $h_2$, and $h_3$ from the tool contact with the workpiece in the six stages are summarized in Table 6.1. Experimental and modeling results of the thrust force and torque are presented in Fig. 6.6. Square symbols represent the model-predicted thrust force and torque. These symbols are connected by lines and

compared to experimental measurements, which are adopted from Fig. 6.6. Ranges of the tool travel in six stages are also marked in Fig. 6.6.

The model predicts that the peak thrust force occurs at about 2 mm tool travel. It is smaller than the experimental measurement (2.5 mm) due to the assumption of no workpiece deformation. Deformation of the workpiece, as shown in Fig 2.4, will delay the tool travel in reaching the peak thrust force. The predicted peak force occurs in Stage 3. The magnitude of peak thrust force is about same, 750 N for the model and 700 N for experiment. The drop of the thrust force to about 300 N at the start of Stage 4 is successfully predicted in the model. The gradual reduction of the thrust force in Stages 5 and 6 is also well predicted.

The model prediction of the torque shows an early rise to 1.6 N-m at 2.3 mm tool travel. The experimental measurement shows the torque reaches the same level at 3 mm. The effect of workpiece deformation delays the tool travel from reaching the peak value until late in Stage 3. The torque is well predicted in Stage 4. In Stage 5, when the tool starts to contact the cylindrical region, the discrepancy of torque becomes more apparent. The variation of coefficient of friction due to temperature and speed are the likely cause for such discrepancy. As the tool penetrates into the workpiece, the peripheral speed between the tool and workpiece gradually increases. In the meantime, the workpiece and tool temperatures rise significantly. Only one coefficient of friction in the radial direction, $\mu$, is used to cover such wide range of contact conditions. More detailed investigations of the tribological phenomenon between the tool and workpiece are required for more accurate prediction of torque in friction drilling. When the tool is retracting (distance from contact from 12.7 to 14.4 mm), the torque is still measurable in the range between 1.1 to 1.4 N-m. This indicates the existence of residual pressure on the tool after the hole is formed. The torque in this stage is not modeled.

## 6.5. FEM modeling

Mathematical formulations of thermal and mechanical modeling are presented in this section.

### 6.5.1. Thermal modeling

The friction and plastic deformation generate heat and elevate the workpiece temperature. The high temperature softens the workpiece and allows material to flow and form the hole and bushing. The governing equation for the thermal model is:

$$\rho c \frac{\partial T}{\partial t} = k\left[\frac{\partial^2 T}{\partial x^2} + \frac{\partial^2 T}{\partial y^2} + \frac{\partial^2 T}{\partial z^2}\right] + G \tag{6}$$

where $\rho$ is the density, $c$ is the specific heat, $k$ is heat conductivity, $T$ is the temperature, $t$ is the time, $G$ is the heat generation rate, and $x$, $y$, and $z$ are spatial coordinate. The $\rho$, $c$, and $k$ are functions of temperature, which is important for accurate thermal modeling. Both $T$ and $G$ are function of $x$, $y$, $z$, and $t$. The heat generation rate, $G$, in friction drilling consist of the heating by the friction between tool and workpiece, $\dot{q}_f$, and heating from irreversible plastic deformation inside the workpiece, $\dot{q}_p$ [6]:

$$G = \dot{q}_f + \dot{q}_p \tag{7}$$

This study assumes that friction between the tool and workpiece follows Coulomb's friction law. The frictional force, $F_f$, is directly proportional to normal force, $F_n$, by the coefficient of friction, $\mu$, i.e., $F_f = \mu F_n$. The frictional heat generation rate, $\dot{q}_f$, is equal to $F_f$ times the surface velocity of the tool, $V$. At the local contact point with tool radius, $R$, $V = 2\pi RN$, where $N$ is the tool rotational speed. The frictional heat generation rate, $\dot{q}_f$, can be formulated as:

$$\dot{q}_f = 2\pi RN\mu F_n \tag{8}$$

The heat generation rate due to plastic deformation, $\dot{q}_p$, is:

$$\dot{q}_p = \eta\sigma\dot{\varepsilon}^{pl} \tag{9}$$

where $\eta$ is the inelastic heat fraction, $\sigma$ is the effective stress, and $\dot{\varepsilon}^{pl}$ is the plastic straining rate. Most of the elastic portion of the energy in large plastic deformation in the workpiece of friction drilling is small. In this study, $\eta$ was set to 0.9 [6].

### 6.5.2. Mechanical response

The ABAQUS/Explicit code integrates the equations of motion explicitly through time. The term "explicit" means the state at the end of an increment is based solely on the displacements, velocities, and accelerations at the beginning of the increment. At the beginning of the increment the program solves for dynamic equilibrium, which states that the nodal mass matrix times the nodal accelerations equals the total nodal forces [14]. The mechanical response is controlled by the differential equation of motion [4], which in the general form for nodal acceleration vector, $\ddot{u}$, is:

$$\ddot{u}_i = \boldsymbol{M}^{-1}\left(\boldsymbol{P} - \boldsymbol{C}\dot{u}_i - \boldsymbol{K}u_i\right) \tag{10}$$

where $\boldsymbol{M}$ is the mass matrix, $\boldsymbol{P}$ is the vector of forces due to mechanical and thermal stresses, $\boldsymbol{C}$ is the viscous damping matrix, $\boldsymbol{K}$ is the stiffness matrix, $u_i$ and $\dot{u}_i$ are the respective nodal displacement and velocity vectors, and $i$ is the time step. The explicit expression for velocity at the new time step can be determined by applying the central difference integration and incorporating Eq. (10):

$$\dot{u}_{i+1/2} = \frac{\Delta t_{i+1} + \Delta t_i}{2}\ddot{u}_i + \dot{u}_{i-1/2} = \frac{\Delta t_{i+1} + \Delta t_i}{2}\boldsymbol{M}^{-1}\left(\boldsymbol{P} - \boldsymbol{C}\dot{u}_i - \boldsymbol{K}u_i\right) + \dot{u}_{i-1/2} \tag{11}$$

## 6.6. Finite element simulation

### 6.6.1. FEM techniques

A major challenge in this research was an accurate FEM model capable to simulate friction drilling. Three FEM modeling techniques, adaptive meshing, element deletion, and mass scaling, were deployed in order to successfully maintain mesh quality and obtain results. The adaptive meshing and element deletion techniques were needed

because large deformation and excessively distorted elements made convergence of the FEM solution difficult.

Large deformation and distortion of elements were inevitable in the friction drilling model. Adaptive meshing made it possible to maintain a high-quality mesh throughout the analysis by allowing the mesh to move independently of the material [6]. Adaptive meshing in ABAQUS does not alter the topology of the mesh. Elements are not created or destroyed. When large deformation is anticipated, the improved mesh quality resulting from adaptive meshing can prevent the divergence problem as a result of severe mesh distortion. In this study, the adaptive meshing was performed for every five increments of the tool. In each adaptive meshing, a new, smoother mesh was created by sweeping iteratively three times over the mesh to adjust the nodal positions and improve the aspect ratio of distorted elements.

Element deletion is essential for material separation in friction drilling. Excessively distorted elements were deactivated. The element deletion allows the work-material to separate and tool to penetrate the workpiece [15]. In this study, the criterion to delete an element is based on the value of the equivalent plastic strain, which was suitable for the high strain-rate deformation in friction drilling [14]. When the equivalent plastic strain exceeds a threshold value in an element, all the stress components were set to zero. An example of element deletion during friction drilling is shown in Fig. 6.7. The dark color represents deleted elements, which does not affect the simulation results and can be removed during or at the end of the simulation.

Mass scaling was employed to improve computational efficiency while retaining the accuracy in high deformation FEM modeling. This technique adjusts the density of the work-material in the FEM model. The presence of small elements and reduced characteristic lengths of elements from deformation results in a smaller time increment of tool travel required for the simulation. Scaling the mass of the small elements throughout the simulation can significantly decrease the computation time [14]. In this study mass scaling was performed every 10 increments to obtain a stable time increment of 0.0001 s tool travel.

### 6.6.2. Model parameters and material properties

Figure 6.8 shows the finite element mesh of the workpiece, boundary conditions, and tool geometrical parameters in friction drilling. As shown in Fig. 6.8(a), the workpiece was 101.6 mm in diameter and 1.59 mm thick. Two opposite points on the workpiece were fixed to simulate the clamping points by two C-clamps in the experiment. The top surface of the workpiece was under free convection with convection coefficient of 30 $W/m^2$-°C and ambient air temperature of 22ºC. The tool rotated at 3000 rpm or 314 rad/s. The tool penetration was modeled with three different constant axial speeds of 2.54, 4.23, and 5.93 mm/s into the workpiece.

For the deformable, sheet metal workpiece, the ABAQUS/Explicit finite element software package and its mesh generator were applied. Eight-node hexagonal elements were used in the finite element mesh to model the workpiece in the shape of a disk plate. The initial finite element mesh in Figs. 6.8(a) and (b) included 18,620 elements and 20,814 nodes. Each node had four degrees of freedom: three spatial degrees of freedom in X, Y, and Z directions and one degree of freedom for temperature. The workpiece mesh was finer near the tool tip, as shown in Fig. 6.8(b), where the largest material deformation was expected to occur. The initial mesh could move independent of the material as a result of adaptive meshing. Across the 1.59 mm thickness of the workpiece, 10 rows of elements were generated in the mesh. The simulation results were sensitive to the element size. If the mesh was too coarse, too many elements experienced severe distortion and were deleted, resulting in improper bushing formation. On the contrary, if the mesh was too fine, the computational time increased significantly and results do not change. A balance was struck between computational time and amount of workpiece mesh removed by element deletion.

Figure 6.8(c) shows the bottom view of the stationary, rigid support plate, which limits the movement of the workpiece in the Y direction. The node in contact with the support plate can move in the X and Z directions with the same coefficient of friction as in the tool-workpiece interface. The support plate was 80 mm in outer diameter with a 24.5 mm diameter hole. The friction drilling starts at the center of the hole.

The tool geometric parameters (Fig. 6.8(d)) of the tool used in this study are $\alpha =$ 90°, $\beta = 36°$, $h_c = 0.940$ mm, and $h_n = 5.518$ mm. The tool was modeled as rigid and has

adiabatic boundary condition. The tool geometry was similar to the one used in previous research [16,17,18].

Aluminum alloy 6061-T6 was chosen as the work-material. This is a common material used in FEM modeling of FSW. The temperature-dependent material properties for Al 6061-T6 are widely available. Material properties used in this study are listed in Table 6.3 [19]. In FSW modeling, the elastic perfectly-plastic model [6] was used. This is adopted in this research to simulate the workpiece material behavior in the analysis.

Frictional behavior and contact interaction between the tool and workpiece in friction drilling are complicated [17]. In this study, a constant coefficient of friction was used by Coulomb's friction law before a more comprehensive friction model can be developed. Different coefficients of friction were evaluated in FEM modeling. The same coefficient of friction was used for the tool and support plate interactions with the workpiece.

Heat partition occurs at the interface between the tool and workpiece. For frictional heat generation at the tool-workpiece interface, 100% of the dissipated energy caused by friction was converted to heat. A common heat partition model determines the amount of heat transferred to the tool and workpiece by their respective thermal conductivity. Based on the energy balance, the ratio of heat partition into the workpiece, $r_{al}$, was determined according to:

$$r_{wp} = \frac{k_{wp}}{k_{wp} + k_{tool}} \tag{12}$$

where $k_{wp}$ and $k_{tool}$ are the thermal conductivity of workpiece and tool, respectively. In this study, $k_{wp}$ of the Al 6061-T6 workpiece is 167 W/m-K and $k_{tool}$ of the A2 tool steel is 26 W/m-K. The ratio of heat generated in the tool-workpiece interface transfer to the workpiece is $r_{wp}$ = 0.87, i.e., most of the frictional heat generated was transferred to the Al workpiece.

## 6.7. Experimental setup for validation

Experiments were conducted to measure the thrust force, torque, and workpiece temperature during friction drilling. These measurements are compared to FEM modeling results for validation. The experiment was conducted in a CNC vertical machining center, Mori Seiki model TV 30. The spindle speed was 3000 rpm and three tool feed rates of 2.54, 4.23, and 5.93 mm/s were conducted.

The tool was made from grade A2 air-hardening steel rod. The coefficient of friction data is readily available for the A2 steel and Al 6061-T6 [6]. The tool has a cylindrical shape and does not have the lobular geometry as in some commercially available tools [17]. Dimensions of the tool match those used in FEM modeling, as shown in Fig. 6.8(d).

The thrust force and torque was measured using a Kistler model 9272 dynamometer. The temperature was measured using a type E thermocouple (Omega 5TC-TT-E-36-72) with 0.13 mm diameter placed 5.1 and 7.5 mm from the center of drilling in a 1.0 mm diameter hole at small depth from the top surface of the workpiece, as shown in Fig. 6.9.

## 6.8. Validation of FEM modeling

The measured thrust force, torque, and temperature were used to validate the FEM modeling of friction drilling. Two sets of FEM simulation were conducted. The first set of FEM simulation investigates the effect of coefficient of friction under a constant (4.23 mm/s) tool feed rate. The modeling results were then compared to measured values to determine the best approximation for coefficient of friction. The second set of FEM simulation adopts this coefficient of friction and compares the experimental and FEM results of thrust force, torque, and temperature at three tool feed rates.

### 6.8.1. Investigation of coefficient of friction

Figure 6.10 shows the thrust force and torque of FEM modeling and experimental measurement results for three different coefficients of friction, 0.5, 0.7, and 1.0, under 4.23 mm/s feed rate and 3000 rpm spindle speed. High coefficient of friction decreases

the thrust force but does not change the torque significantly. Peak thrust force at 1,000, 800, and 600 N is observed for coefficients of friction of 0.5, 0.7, and 1.0, respectively. Coefficient of friction of 0.7 was the best match based on comparison of thrust force and torque of FEM modeling and experimental measurement results.

High friction generates high workpiece temperature, which softens the work-material and reduces the thrust force. The peak workpiece temperature, 530, 580, and 790°C was observed for coefficients of friction of 0.5, 0.7, and 1.0, respectively. For all three tests, the peak temperatures were located on the workpiece surface of the hole contacting the tool at the height close to the deformed sheet metal workpiece. The discoloration of the 1020 sheet metal workpiece in Fig. 6.3 confirmed the location of high temperature in friction drilling experimentally. The time for peak temperature is at the tool location near the maximum torque.

Trend for torque is much less obvious. Torque curves are identical until about 7 mm from the start of the simulation. After 7 mm a trend is noticeable of decreasing torque for increasing coefficient of friction. High coefficient of friction increases the frictional force and, subsequently, the torque. However, increased temperature from frictional heating softens work-material to lower torque. These two phenomena balance each other and results in the small change in torque.

### 6.8.2. Validation of the thrust force and torque

Figure 6.11 shows the comparison of thrust force and torque from experimental measurements and model results for three different feed rates, 5.93, 4.23, and 2.54 mm/s with coefficient of friction of 0.7. Overall agreement between experimental and modeling of thrust force and torque was good. The peak force was about 800, 750, and 700 N for experimental feed rates of 5.93, 4.23, and 2.54 mm/s, respectively. These values were slightly lower than for FEM modeling results under similar conditions.

The FEM modeling thrust force profiles in time were shifted to the left of the experimental profiles, as shown in Fig. 6.11. It was observed that the sheet Al workpiece has noticeable deflection in the initial contact stage. Such phenomenon was not accurately modeled by FEM and led to the early peaking of the thrust force and torque in FEM modeling. Figure 6.12 shows the relative position of workpiece near the peak thrust

force for both FEM model (Fig. 6.12(a)) and experiment (Fig. 6.12(b)) with 4.23 mm/s tool feed rate. The peak thrust force occurs at 1.78 and 2.75 mm from the initial contact of the tool and workpiece for the FEM model and experiment, respectively. The penetration of the tool into the workpiece is approximately the same but the actual tool travel from the initial contact was about 1 mm more in the experiment (Fig. 6.12(b)). This shows the deflection of the workpiece in experiment. At the lowest tool feed rate (2.54 mm/s), the effect of workpiece deflection is less significant. The slower tool feed rate generates lower thrust force and smaller workpiece deflection, which matches better with FEM prediction. The slower feed rate allows more time for heat generation and work-material softening.

For torque, as shown in Fig. 6.11, the discrepancy of modeling and experiment also improved at low tool feed rate. The FEM model overestimated the torque in the initial contact stage, but underestimated the torque in the following contact period. The maximum torque was underestimated by about 33, 32, and 25% for tool rate of 5.93, 4.23, and 2.54 mm/s, respectively. As discussed in Sec. 6.6.1 and shown in Fig. 6.10, adjusting the coefficient of friction has little effect on torque curves in FEM modeling. This discrepancy demonstrates the limitation of the Coulomb friction model and the need to implement new friction models to achieve a more accurate prediction of the torque in friction drilling modeling.

### 6.8.3. Validation of temperature

Figure 6.13 shows the comparison of temperature from experimental measurement and FEM modeling for 4.23 mm/s tool feed rate. For FEM modeling, the temperature at four nodes, 2.74, 3.45, 5.11, and 7.53 mm initial position from the hole center, is presented. The temperature of thermocouple embedded at 5.11 and 7.53 mm from the hole center is also presented. At 5.11 and 7.53 mm from the hole center, the FEM peak temperature is 270 and 190°C, compared to 240 and 170°C for experimental measurement, respectively.

Other thermocouples installed closer to the hole center were damaged during experiment and could not obtain temperature reading. This demonstrates the difficulty to experimentally investigate friction drilling and the benefit of FEM modeling.

Temperatures at 2.74 and 3.45 mm initial position from the hole center are also shown in Fig. 6.13. The temperature is higher close to the hole center. Peak temperatures at 2.74 and 3.45 mm from the hole center are about 400 and 350°C, respectively.

## 6.9. FEM analysis of work-material deformation and temperature

The advantage of FEM simulation is the ability to gain insight into the friction drilling work-material deformation and temperature profile, which are difficult to measure experimentally. Figure 6.14 shows the deformed mesh and distribution of plastic strain, temperature, and von-Mises stress of the cross-section of the workpiece at 1.78, 6.35, and 7.96 mm tool displacement from the contact between tool and workpiece. The tool travel of 1.78 mm and 6.35 mm are near peak thrust force and peak torque, respectively. The deformed bushing shape is completed at 7.96 mm tool travel. Figure 6.16 shows the vectors for velocity and contact force at 0.846, 2.12, 4.02, and 5.50 mm tool displacement. Process parameters for Figs. 6.134 and 6.16 were 4.23 mm/s tool feed rate, 3000 rpm spindle speed.

### 6.9.1. Deformed finite element meshes and strain

The cross-sectional view of the deformed mesh after element deletion is shown in Fig. 6.14. Shearing of the elements from right to left is evident on the inside wall of the hole. The distortion of elements is severe in the initial contact at 1.78 mm tool travel. The distorted elements are likely to contribute to the lack of modeling accuracy to predict the contact force and workpiece deflection at high tool feed rates. At tool travel of 6.35 and 7.96 mm, the formation of bushing is observed. The effect of element deletion on the prediction of bushing shape is a concern. The comparison of the cross-sectional shape of bushing from FEM modeling and experiment at the end of tool penetration is shown in Fig. 6.15. Although some elements were deleted by element deletion, its effect on the shape of bushing is not significant. The extrusion on the top of the workpiece is largely missing. It is likely due to the combination of the element deletion and limitation of the FEM model for small scale features on deformed workpiece.

The peak plastic strain, as shown in Fig. 6.14 is observed on the contact surface with the tool. The peak value of plastic strain is about the same, 2.2, independent of the tool travel. This can be explained by the element deletion, which removes largely distorted elements by the plastic strain criterion.

### 6.9.2. Temperature

Friction drilling temperature measurements have been conducted using the infrared camera in Chapter 2 [1] and by thermocouples in this study. Temperature distribution provided by FEM model is more comprehensive, as shown in Fig. 6.14. Work-material temperature is the highest on the contact surface with the tool. At 1.78 mm of tool travel, temperature is not high, about 300°C on the contact surface. At 6.35 mm of tool travel, a stripe of high temperature close to 580°C is observed along the contact area with the originally undeformed workpiece. This has been presented in the discoloration on the hole surface in friction drilling of AISI 1020 steel (Fig. 6.3). For Al 6061-T6, the solidus temperature of is 582°C and liquidus temperature is 652°C. The high temperature in friction drilling is close to the melting temperature of workpiece. At 7.96 mm tool travel, location of the peak temperature stays in the region of the undeformed sheet. Temperature decreases in the bushing and in the workpiece as distance from the hole increases radially.

### 6.9.3. Von-Mises stress

Von-Mises stress is shown in the last row of Fig. 6.14. Contrary to the intuition that high stress occurs at tool contact surface, the stress is actually low on the inside surface of the hole due to the high temperature. At 1.78 mm tool travel, the maximum stress of 280 $N/mm^2$ can be seen in the workpiece surrounding the hole. This high stress is due to the bending of the workpiece and the low temperature in the region. At 6.35 and 7.96 mm tool travel, the peak stress at about 230 $N/mm^2$ occurs in the workpiece away from the hole. The bending effect and low temperature once again contribute to the location of this high stress.

Distributions of stress and temperature demonstrate how the friction heats and softens the work-material in friction drilling. The high temperature softens the work-material in the contact region and makes the bushing formation possible.

### 6.9.4. Nodal velocity vectors

Figure 6.16 shows the top view and front view of velocity vectors at nodes on the contact surface. Only nodes with velocity larger than 2 mm/s are presented. Velocity vectors in the radial direction represent the deformation axisymmetrically and in the tangential direction represent the deformation in the circumferentially. The top view at 2.12 mm tool travel shows most the deformation is mostly in the radial direction. In this case, the axisymmetric FEM model is adequate to model the deformation. However, the top view at 4.02 and 5.50 mm tool travel indicates large rotational material flow with velocity vectors mostly tangential to the hole. The 3D FEM model is required to model the material flow in the combined rotational and radial directions. In the front view, large velocity can be seen in the horizontal direction, representing shearing of the work-material as the tool rotates. Near the top of the workpiece vectors can be seen pointing upward for the back extrusion. On the bushing, at 4.02 and 5.50 mm tool travel, small velocity vectors to represent the gradual formation of the bushing.

### 6.9.5. Nodal contact force vectors

The last row in Fig. 6.16 shows vectors representing the contact force between the tool and workpiece. All contact force vectors appear normal to the tool surface. The largest nodal contact force (46.4 N) is at 2.12 mm tool travel near the peak thrust force in friction drilling. The contact force is also high at 0.846 mm tool travel. At 4.02 and 5.50 mm tool travel, the contact forces on bushing are small, as most of the contact force vectors are observed in the region of the undeformed sheet. In the analytical model to predict thrust force and torque in friction drilling a hypothesis was proposed that the tool contact surface with bushing does not contribute to the thrust force and torque. This observation directly proves the hypothesis.

## 6.10. Conclusions

A mathematical model based on the contact area between the undeformed workpiece and the rigid, unworn tool was proposed with temperature-dependent stress-strain properties of the work-material. The model-predicted thrust force and torque correlated well with experimental measurements. Some discrepancies existed and showed the limitation of the simplified friction model used in this study. There was a difference in peak force from the neglect of workpiece deflection. The discrepancy in torque near the end of the process suggested that the bushing contribution to the torque should be included. However, the addition of the bushing in the calculations would significantly complicate the analytical model.

The 3D FEM model was capable of modeling the work-material deformation in friction drilling. Three FEM techniques were found to enable simulation convergence with large material flow. Due to uncertainty about frictional properties, an investigation in the model determined the most suitable coefficient of friction was 0.7. The FEM modeling results for thrust force, torque, and temperature had reasonable agreement with the experimental measurements .

The FEM analysis generated detailed data of material deformation that are difficult to measure experimentally. The model showed that the peak temperature of the workpiece in friction drilling was high, about 580°C, close to the melting temperature of the Al6061 workpiece. The deformed mesh and distributions of stress and temperature from the FEM model were valuable to show how the work-material softens and forms the bushing. The work-material flowed in the rotational direction around the tool confirming that 3D FEM modeling was required.

Limitations of the model include the simple Coulomb's friction model, which caused a discrepancy in the torque curves. Tool stress or temperature was not modeled to reduce computational time in the study. Element deletion caused a reduction in mass of the workpiece, but was necessary to enable completion of the simulation.

Table 6.1. Parametric representation of the tool-workpiece contact in six stages.

| Stage | Range of tool travel | Center ($h_1$, $h_2$) | Conical ($h_1$, $h_2$) | Cylindrical ($h_3$) |
|---|---|---|---|---|
| 1 | $0 < h < h_c$ | 0, $h$ | -- | -- |
| 2 | $h_c < h < t$ | 0, $h_c$ | $h_c + h^*$, $h + h^*$ | -- |
| 3 | $t < h < t + h_c$ | $h - t$, $h_c$ | $h_c + h^*$, $h + h^*$ | -- |
| 4 | $t + h_c < h < h_c + h_n$ | -- | $h - t + h^*$, $h + h^*$ | -- |
| 5 | $h_c + h_n < h < h_c + h_n + t$ | -- | $h - t + h^*$, $h_c + h_n + h^*$ | $h - h_c - h_n$ |
| 6 | $h_c + h_n + t < h < h_c + h_n + h_l$ | -- | -- | $t$ |

Table 6.2. Numerical example of the tool-workpiece contact in six stages. (Unit: mm)

| Stage | Range of tool travel | Center ($h_1$, $h_2$) | Conical ($h_1$, $h_2$) | Cylindrical ($h_3$) |
|---|---|---|---|---|
| 1 | $0 < h < 0.97$ | 0, $h$ | -- | -- |
| 2 | $0.97 < h < 1.19$ | 0, 0.97 | 2.985, $h + 2.015$ | -- |
| 3 | $1.19 < h < 2.160$ | $h - 1.19$, 0.97 | 2.985, $h + 2.015$ | -- |
| 4 | $2.160 < h < 9.460$ | -- | $h - 3.205$, $h$ +2.015 | -- |
| 5 | $9.460 < h < 10.650$ | -- | $h - 3.205$, 11.475 | $h - 9.460$ |
| 6 | $10.650 < h < 18.356$ | -- | -- | 1.19 |

Table 6.3. Temperature-dependent material properties for Aluminum 6061-T6 [20].

| Temperature (°C) | 37.8 | 93.3 | 149 | 204 | 260 | 316 | 371 | 427 |
|---|---|---|---|---|---|---|---|---|
| Thermal Conductivity (W/m°C) | 162 | 177 | 184 | 192 | 201 | 207 | 217 | 223 |
| Heat Capacity (J/Kg°C) | 945 | 978 | 1000 | 1030 | 1052 | 1080 | 1100 | 1130 |
| Density (Kg/m$^3$) | 2690 | 2690 | 2670 | 2660 | 2660 | 2630 | 2630 | 2600 |
| Young's Modulus (GPa) | 68.5 | 66.2 | 63.1 | 59.2 | 54.0 | 47.5 | 40.3 | 31.7 |
| Yield Strength (MPa) | 274 | 265 | 248 | 219 | 160 | 66.2 | 34.5 | 17.9 |
| Thermal Expansion (1/°C) *10$^{-6}$ | 23.5 | 24.6 | 25.7 | 26.6 | 27.6 | 28.5 | 29.6 | 30.7 |

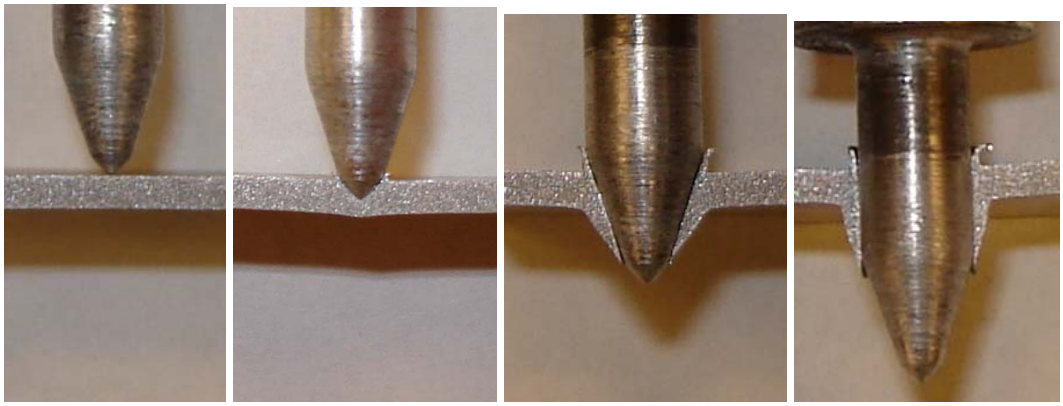

(a) Stage 1 (b) Stage 2 (c) Stage 3 (d) Stage 4

Figure 6.1. Four stages of tool location and workpiece deformation in friction drilling of 1.6 mm thick Al 6061 at tool travel of (a) 0, (b) 2.77 (c) 7.19 and (d) 14.0 mm , from the initial contact (5.3 mm hole diameter).

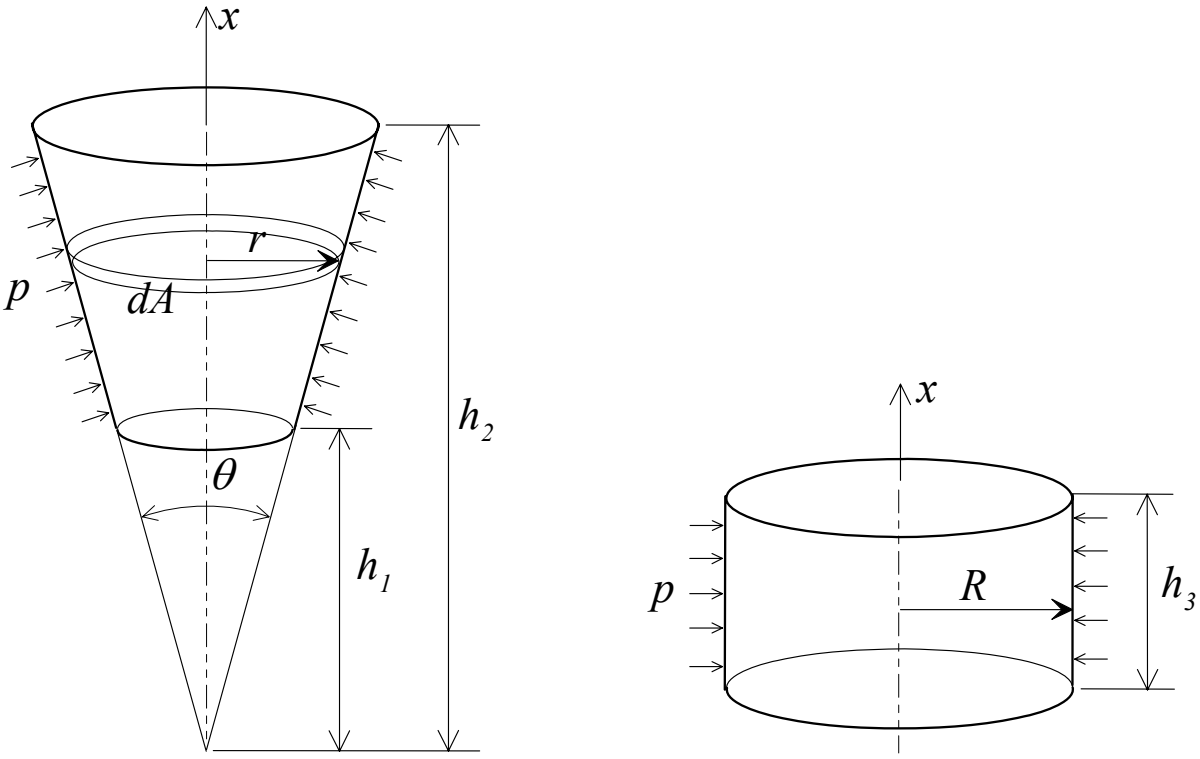


(a) Tapered cylinder (b) Straight cylinder

Figure 6.2. Two basic areas for contact between the tool and workpiece in friction drilling force modeling.

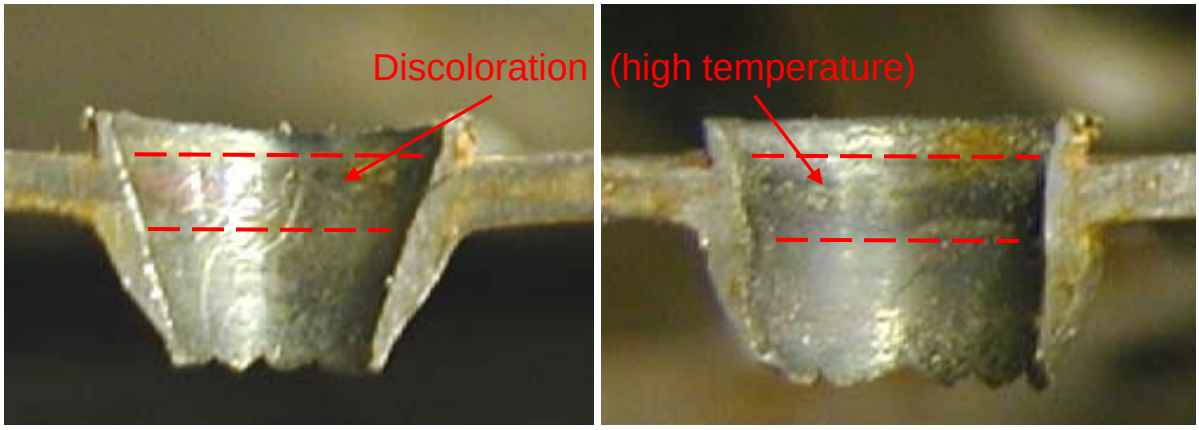


Figure 6.3. A band of discoloration in the drilled hole.

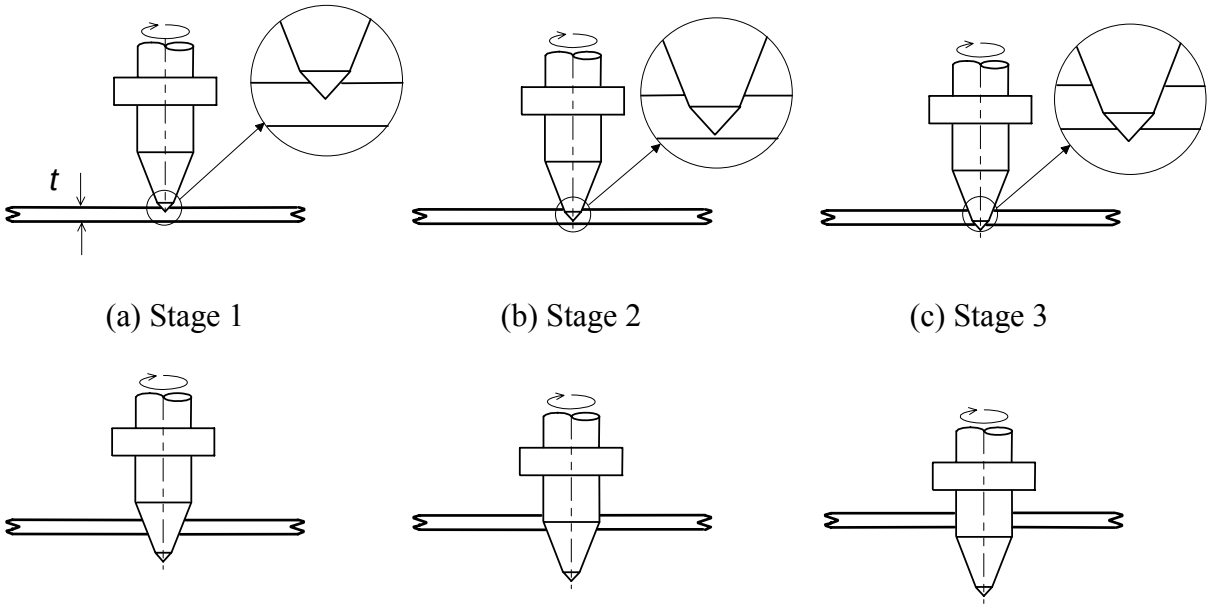


(a) Stage 1 (b) Stage 2 (c) Stage 3

(d) Stage 4 (e) Stage 5 (f) Stage 6

Figure 6.4. Six stages in friction drilling force modeling.

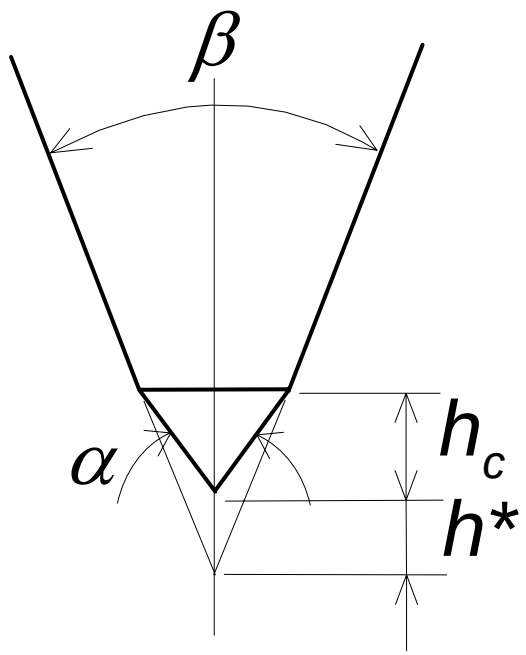


Figure 6.5. Geometrical relationship to calculate $h^*$.

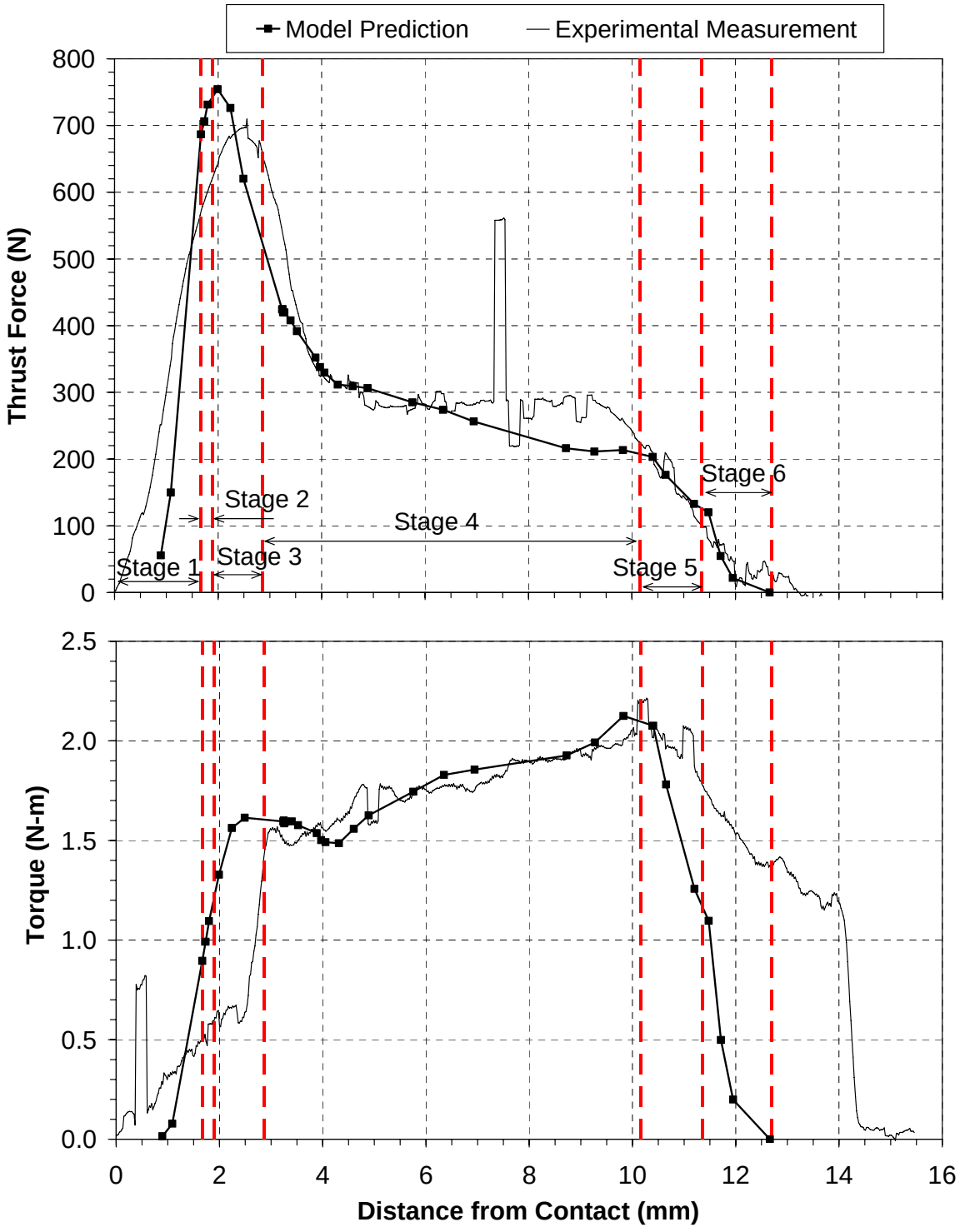


Figure 6.6. Comparison of the experiment vs. model predicted thrust force and torque in friction drilling.

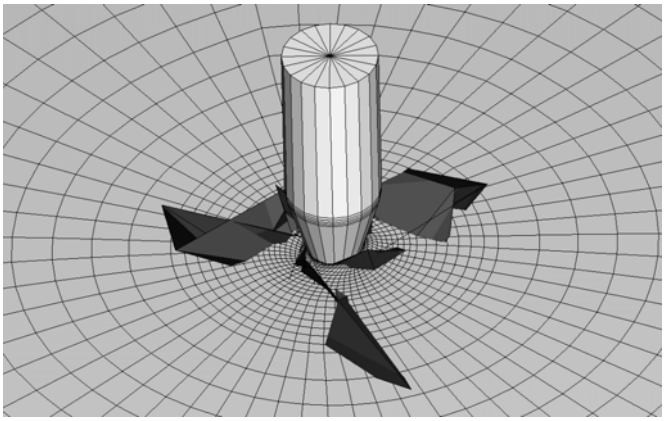

Figure 6.7. Depiction of deleted elements (dark) in FEM modeling of friction drilling.

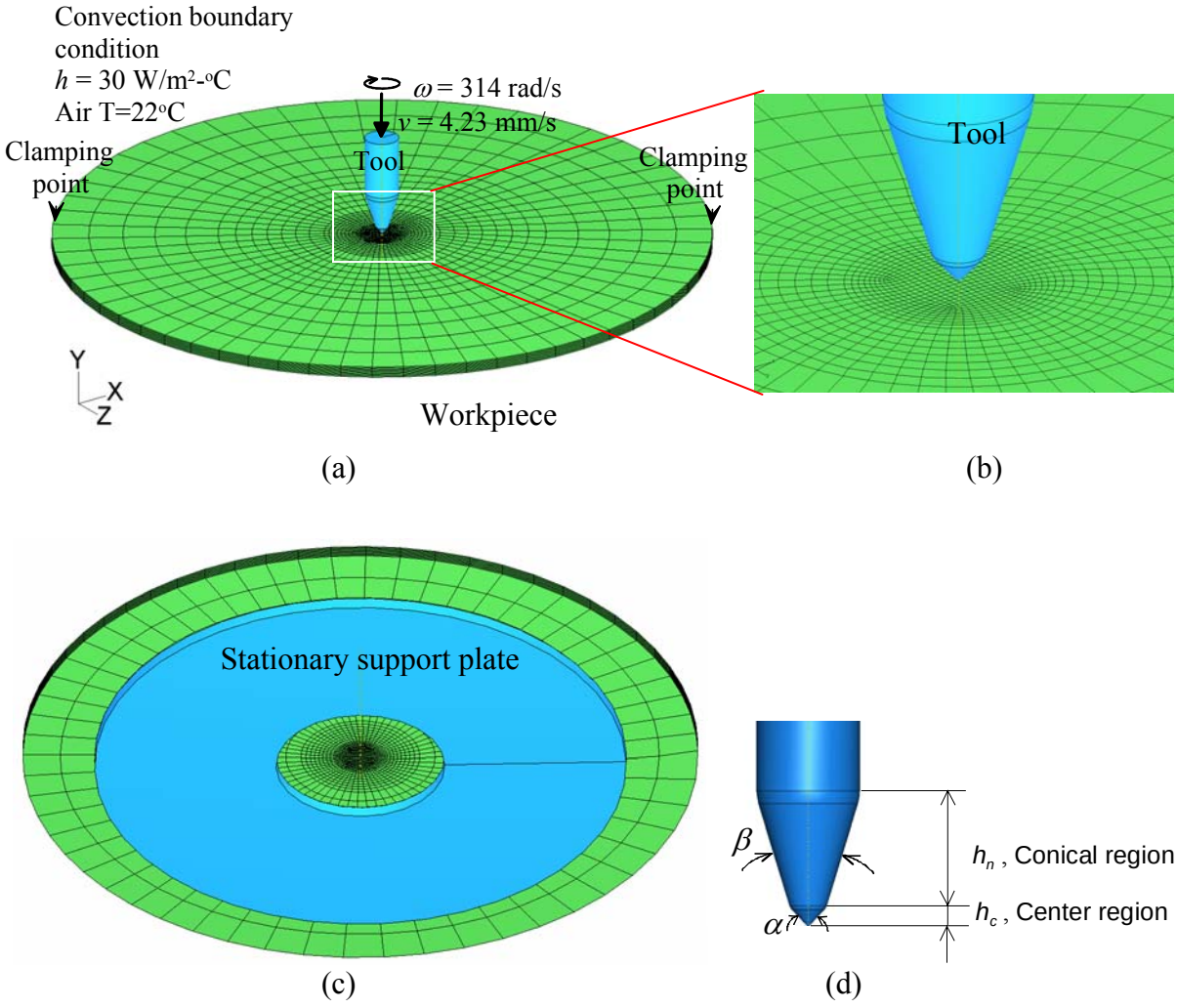


Figure 6.8. FEM modeling of friction drilling (a) initial positions of the tool and workpiece and mesh of the workpiece, (b) close-up view of the mesh near the tool tip, (c) bottom view showing the stationary support plate, and (d) tool geometry parameters.

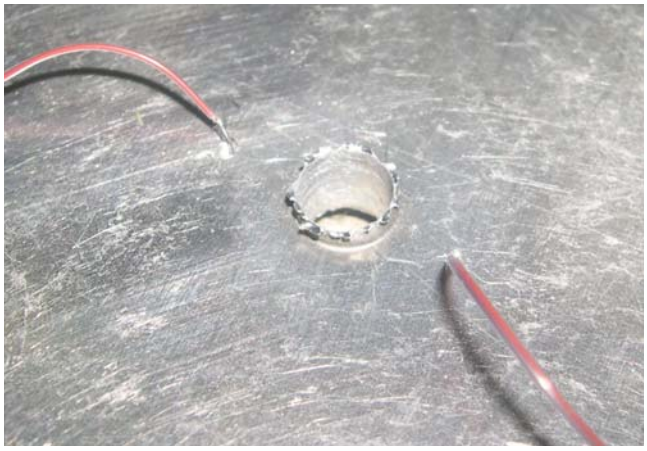

Figure 6.9. Two thermocouples embedded in small holes on workpiece 7.5 and 5.1 mm from the center of drilling for temperature measurement (5.3 mm diameter drilled hole between thermocouples for scale).

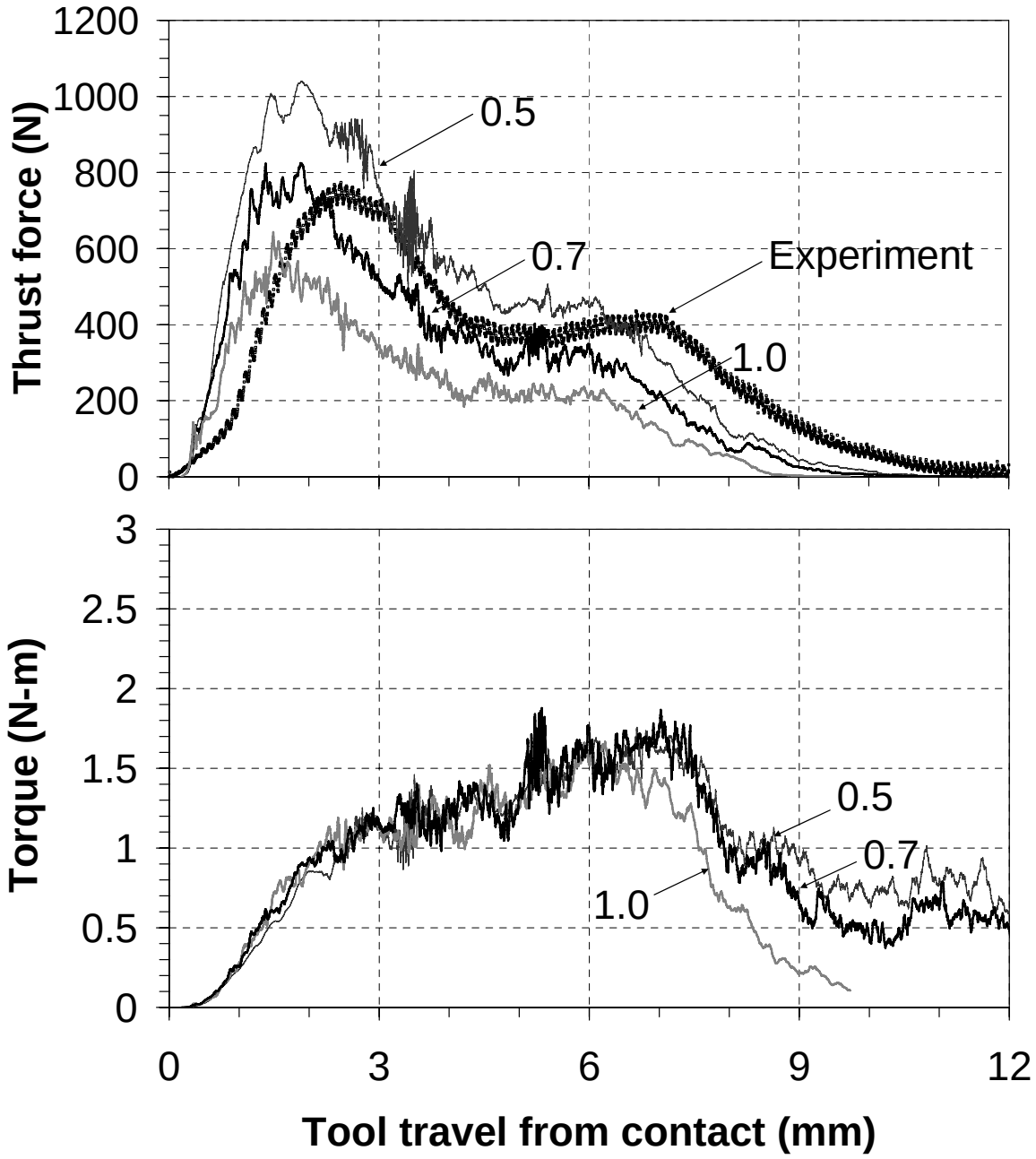


Figure 6.10. Comparison of modeling thrust force and torque for different friction coefficients with 4.23 mm/s feed rate and 3000 rpm spindle speed.

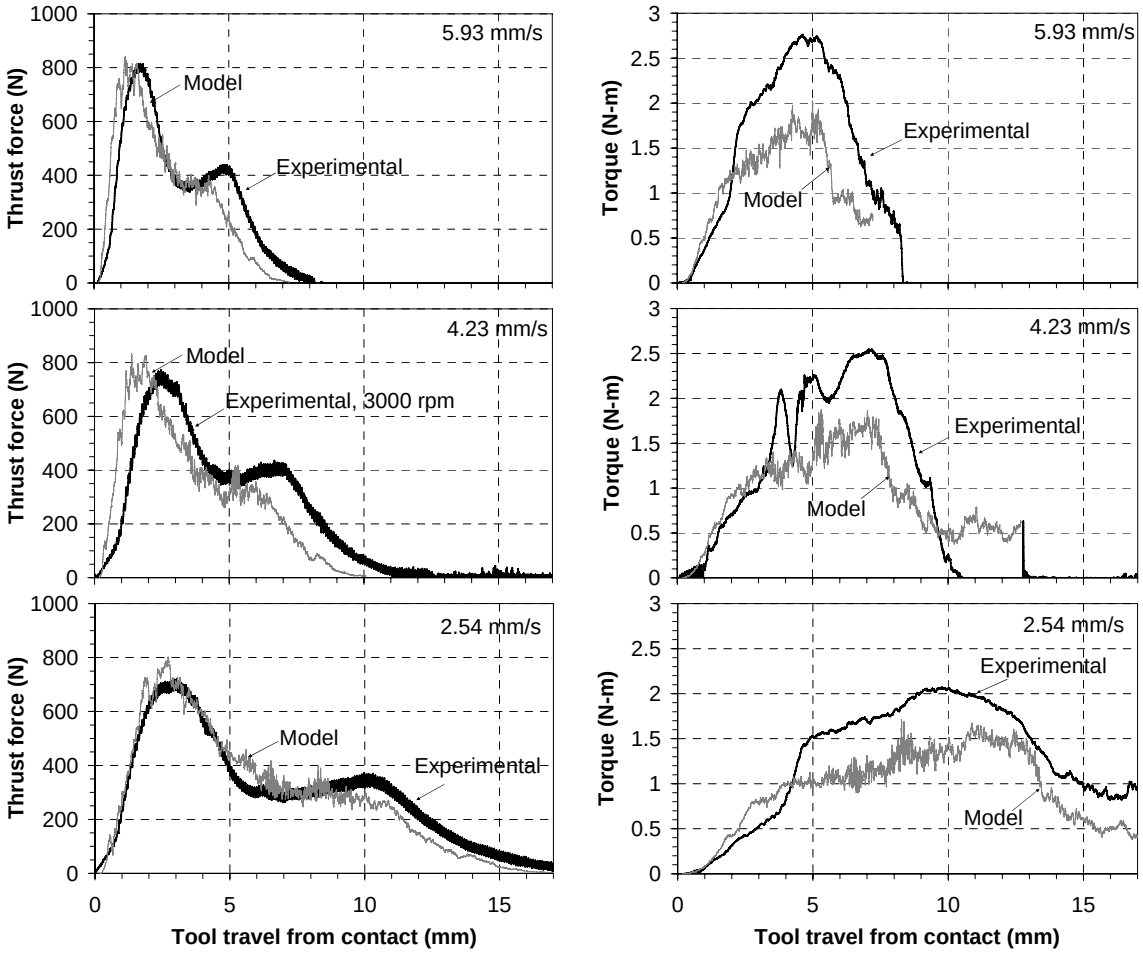


Figure 6.11. Comparison of the experiment vs. model predicted thrust force and torque in friction drilling for 3000 rpm spindle speed, 0.7 coefficient of friction, and three different feed rates, 5.93, 4.23, and 2.54 mm/s.

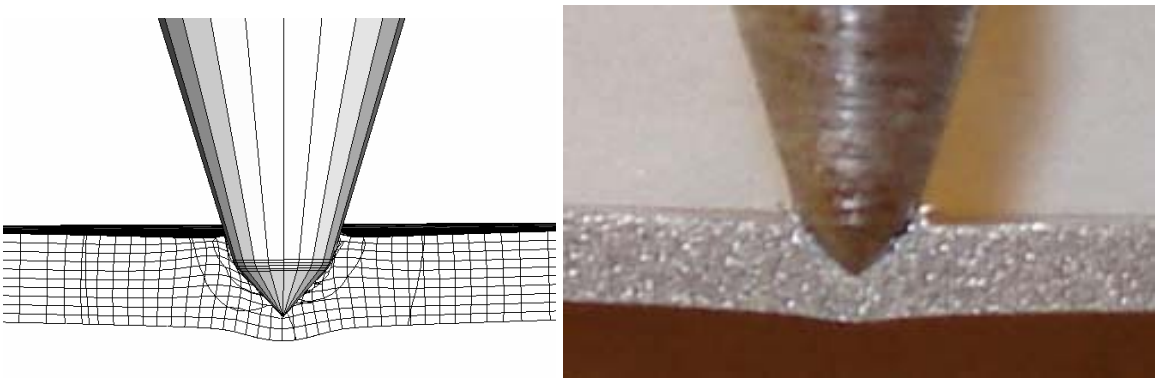

(a) (b)

Figure 6.12. Comparison of the tool-workpiece relative position at peak thrust force (a) FEM model, 1.78 mm tool travel from the initial tool-workpiece contact, and (b) experiment, 2.75 mm tool travel from the initial tool-workpiece contact (4.23 mm/s tool feed rate).

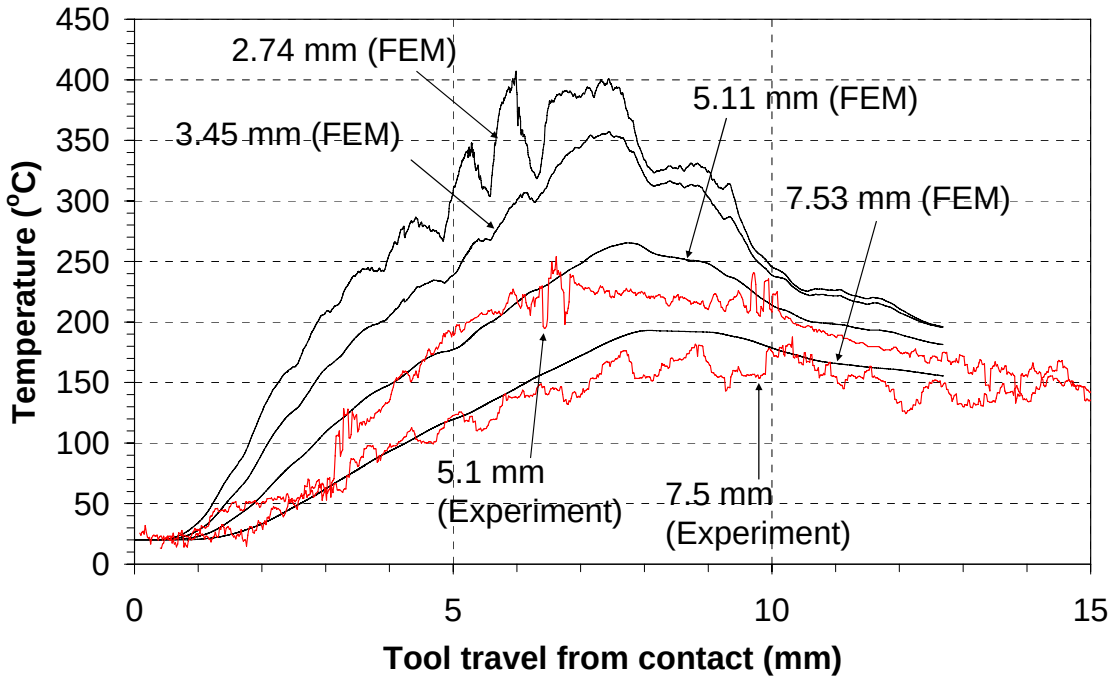


Figure 6.13. FEM modeling and experimental measurement of temperature in friction drilling for 3000 rpm spindle speed, 0.7 coefficient of friction, and 4.23 mm/s tool feed rates.

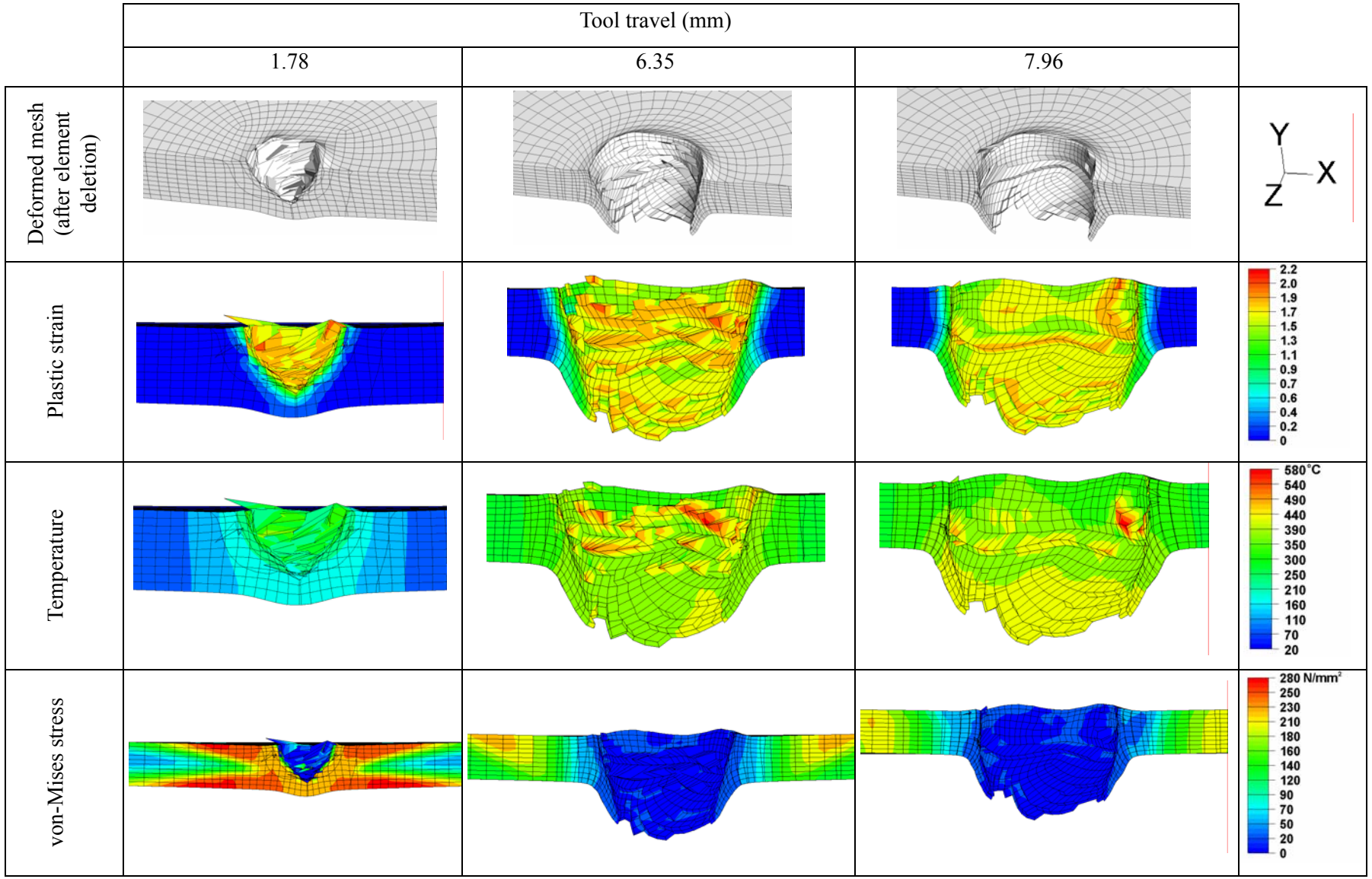


Figure 6.14. Deformed mesh and distribution of plastic strain, temperature, and von-Mises stress in FEM modeling of friction drilling (4.23 mm/s feed rate, 3000 rpm spindle speed, 0.7 coefficient of friction)

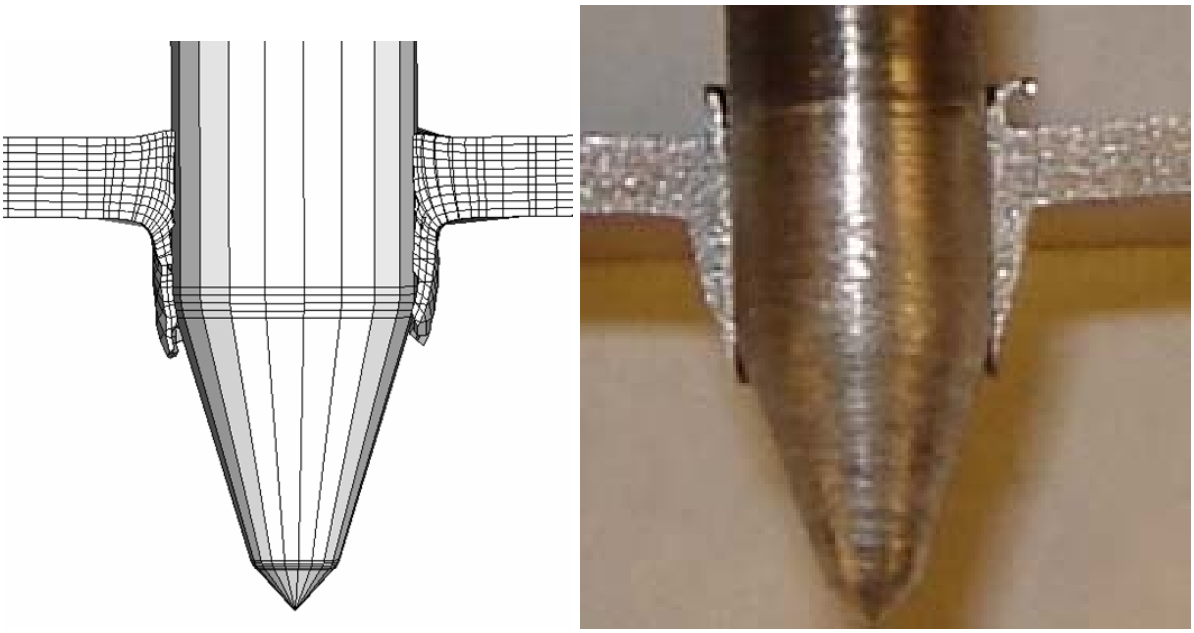

(a) (b)

Figure 6.15. Comparison of the bushing shape (a) FEM model and (b) experiment (4.23 mm/s tool feed rate).

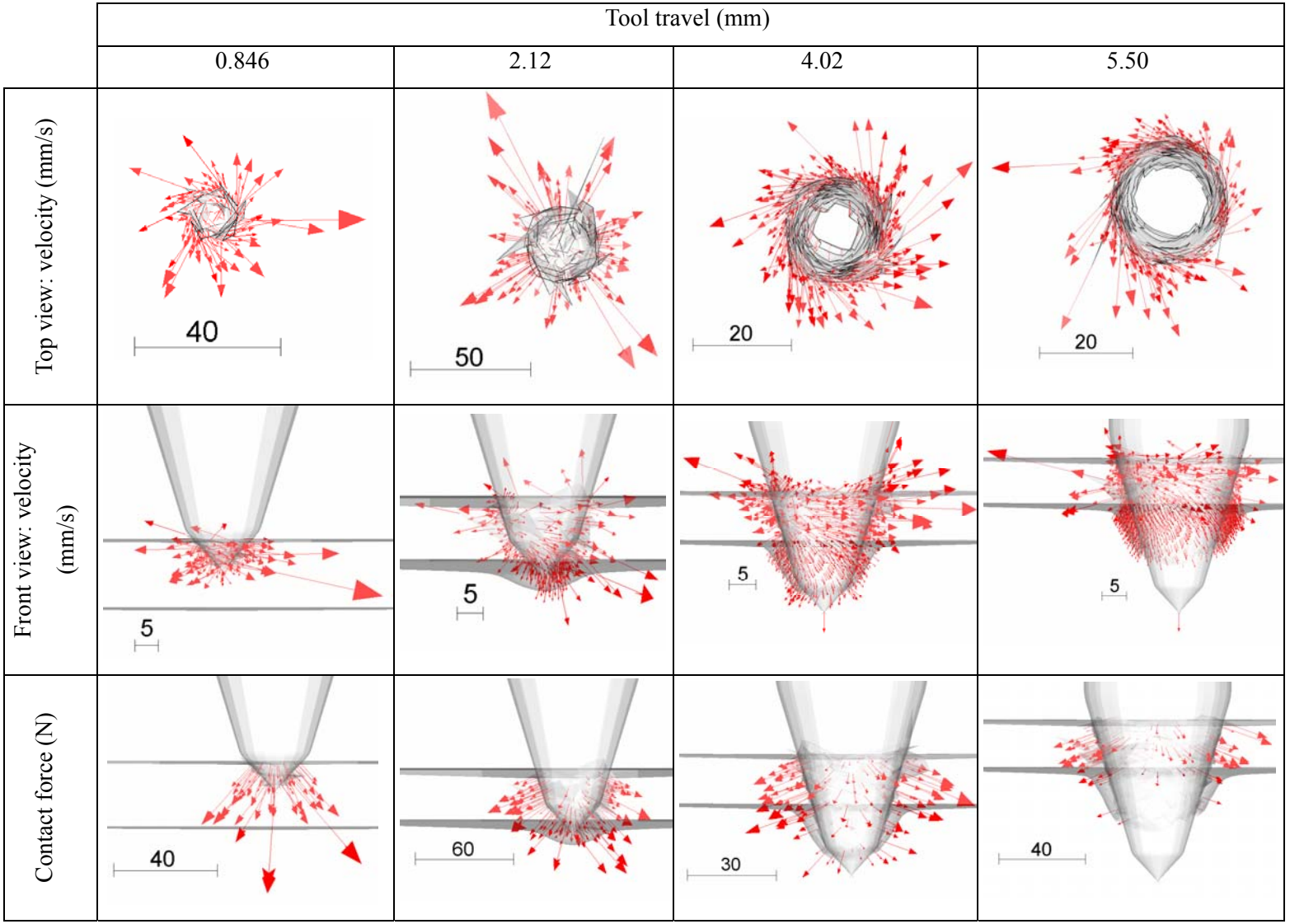


Figure 6.16. Velocity and force vectors for four different locations of tool travel.

## References


[1] S.F. Miller, H. Wang, R. Li, and A.J. Shih, Experimental and numerical analysis of the friction drilling process, Journal of Manufacturing Science and Engineering (accepted) (2004).

[2] Z. Feng, M. L. Santella, S. A. David, R.J. Steel, S.M. Packer, T. Pan, M. Kuo, and R.S. Bhatnagar, Friction Stir Spot Welding of Advanced High-Strength Steels – A Feasibility Study, SAE Technical Paper No 2005-01-1248, Society of Automotive Engineers (2005).

[3] Y.J. Chao, X. Qi, and W. Tang, Heat Transfer in Friction Stir Welding-Experimental and Numerical Studies, Transactions of the ASME, Journal of Manufacturing Science and Engineering 125 (2003) 138-145.

[4] H. Schmidt and J. Hattel, A local model for the thermomechanical conditions in friction stir welding, Modelling and Simulation in Materials Science and Engineering 13 (2005) 77-93.

[5] V. Soundararajan, S. Zekovic, and R. Kovacevic, Thermo-mechanical model with adaptive boundary conditions for friction stir welding of Al 6061, International Journal of Machine Tools & Manufacture 45 (2005) 1577-1587.

[6] M. Awang, V.H. Mucino, Z. Feng, and S.A. David, Thermo-mechanical Modeling of Friction Stir Spot Welding (FSSW) Process: Use of an Explicit Adaptive Meshing Scheme, Technical Paper for the Society of Automotive Engineers 2005 World Congress, April 13, 2005, Detroit, MI.

[7] S.S.T. Kakarla, K.H. Muci-Kuchler, W.J. Arbegast, and C.D. Allen, Three-Dimensional Finite Element Model of the Friction Stir Spot Welding Process, Friction Stir Welding and Processing III as held at the 2005 TMS Annual Meeting; San Francisco, CA; USA; 13-17 Feb. 2005. pp. 213-220.

[8] S.L. Soo, D.K. Aspinwall, and R.C. Dewes, 3D FE modeling of the cutting of Inconel 718, Journal of Materials Processing Technology 150 (2004) 116-123.

[9] Z. Feng, J.E. Gould, and T.J. Lienert, Heat Flow Model for Friction Stir Welding of Aluminum Alloys, Proceedings of the TMS Fall Meeting – Symposium on Hot Deformation of Aluminum Alloys II, Oct 11-Oct 15 1998, Rosemont, IL, USA, pp. 149-158.

[10] G. Buffa, J. Hua, R. Shivpuri, and L. Fratini, A continuum based fem model for friction stir welding – model development, Materials Science and Engineering A 419 (2006) 389-396.

[11] S. Serway, Physics for Scientists and Engineers, 5th ed., Saunders College, PA, 2000.

[12] H. Schmidt, J. Hattel, and J. Wert, An analytical model for the heat generation in friction stir welding, Modelling and Simulation in Materials Science and Engineering 12 (2004) 143-157.

[13] H.E. Boyer, Atlas of Stress-strain Curves, ASM International, pp. 157, 1987.

[14] ABAQUS/Explicit User's Manual, vol. 6.5, 2004.

[15] D. Servis and M. Samuelides, Implementation of the T-failure criterion in finite element methodologies, Computers and Structures 84 (2006) 196-214.

[16] S.F. Miller, P. Blau, and A.J. Shih, Microstructural alterations associated with friction drilling of steel, aluminum, and titanium, Journal of Materials Engineering and Performance 14 (5) (2005) 647-653.

[17] S.F. Miller, P. Blau, and A.J. Shih, Tool Wear in Friction Drilling, Wear (submitted) (2006).

[18] S.F. Miller, J. Tao, and A.J. Shih, Friction drilling of cast metals, International Journal of Machine Tool and Manufacture (accepted) (2005).

[19] Y. Chao, and X. Qi, Thermal and Thermo-Mechanical Modeling of Friction Stir Welding of Aluminum Alloy 6061-T6, Journal of Materials Processing & Manufacturing Science 7 (1998) 215-233.

# CHAPTER 7.

# CONCLUSIONS AND FUTURE WORK

## 7.1. Conclusions

This dissertation investigated experimental analysis and numerical modeling of the friction drilling process. Experiments were conducted to study details of the thrust force, torque, and temperature. Workpiece deflection and deformation were noticed throughout the process. A material analysis was performed to study effects of strain and heat in friction drilling on work-material. Microindentation hardness profiles were made to quantify changes in hardness near the surface of the hole. Optical micrographs were taken at different locations to observe microstructural changes. Effects of workpiece preheating and high spindle speed were investigated in friction drilling of brittle cast metals. An in depth study provided a complete characterization of tool wear. Two models were proposed for the friction drilling process. A simple semi-empirical model was created to predict thrust force and torque. The more detailed 3D FEM modeled the process more accurately. Experiments were performed to validate the models.

### 7.1.1. Experimental measurement of thrust force and torque

Different stages were identified from experimental results of thrust force, torque, and temperature in the friction drilling process as different tool regions engaged the workpiece. Thrust force and temperature initially increased rapidly as the center region contacted the workpiece. Thrust force dropped as the workpiece was separated, and the torque increases gradually as the area of tool-workpiece contact grew. The conical and cylindrical regions of the tool contributed to form the bushing. The heating, mostly from friction, produced high temperature of 760°C, about ½ of the melting temperature.

### 7.1.2. Microstructural and material property changes

Varying amounts of hardening were noticed near the hole surface for different materials, showing evidence of strain hardening. Hardening has a positive effect on strength of a friction drilled hole, insofar as temper embrittlement does not occur. Near hole grain microstructure was altered significantly, suggesting a highly sheared, deformed layer and large material flow rotationally around the tool. The surface of the hole in the aluminum and titanium work-materials was severe damaged and torn.

### 7.1.3. Friction drilling of cast aluminum and magnesium metals

Workpiece preheating improved bushing formation in brittle cast aluminum. The external source of heat increased ductility and softened the work-material. Another idea to increase heat transfer to the workpiece, high spindle speed, did not improve bushing formation. The workpiece preheating and high spindle speed reduced the thrust force and torque enabling higher feed rate and, therefore, improving cycle time.

### 7.1.4. Tool wear

The tool proved to be durable, showing minimal wear after 11000 drilled holes. Results of measurements of tool dimensions indicated that the wear was concentrated at the tool center region and at the intersection between the conical and cylindrical regions. Thrust force measured throughout the study decreased late in tool life due to sharpening of the tool. Oxidation was suggested by EDS analysis of elemental composition. Adhesive and abrasive wear were observed in friction drilling.

### 7.1.5. Analytical and FEM model

The analytical model, based on temperature dependent pressure of work-material yield strength on the tool-workpiece contact area, predicted thrust force and torque for a steel workpiece with reasonable accuracy. However, assumptions caused discrepancies in the modeling results. The neglected workpiece deflection led to the difference in peak force. The area of the bushing was not included in the model, leading to a premature drop in the model result for torque.

The FEM provided a more complex model for friction drilling. FEM meshing techniques enabled the large deformation of the workpiece. A constant coefficient of friction of 0.7 was most suitable for the model. A large amount of work-material deformed in the rotational direction around the tool. Maximum work-material temperature was near the melting temperature of Al 6061 (580°C) on the inside wall of the hole. Due to the high temperature near the tool, the maximum stress was observed further from the wall in the sheet.

Limitations in the FEM model included the simple Coulomb's law for coefficient of friction. This led to the inaccuracy of the modeling results for torque. The FEM failed to model initial workpiece elastic deflection, causing a shift in the thrust force curves. Information of temperature and stress in the tool could not be generated due to the simplification of the isothermal tool. The element deletion feature, although necessary for completion of the simulation, caused a decrease in elements and mass of the work-material, which resulted in a smaller bushing.

### 7.1.6. Contributions of this research

The major contributions of this research are summarized as follows.

- Different stages in the friction drilling process were identified. The stages were marked by changes in thrust force, torque, and temperature. A relationship between these and work-material deformation was established.
- Effects of friction drilling on microstructure and subsurface hardness were characterized for different materials. Knowledge about material behavior and evolution was obtained.
- External heating proved capable to increase work-material ductility and flow, making friction drilling potentially applicable to a wider range of less ductile materials.
- Results of a wear study proved the tool is durable. Tool wear mechanisms were identified in friction drilling. Details of tool wear and how it affects the tool performance were presented.

- Two models were established for friction drilling, which provided a deeper understanding of the friction drilling process. The analytical model took a mathematical approach to describe how the temperature, contact area between the workpiece, and material properties influence thrust force and torque. A 3D FEM simulation of the friction drilling process established meshing techniques that enabled modeling of the large deformation in the friction drilling process. The model generated information about material deformation and temperature and stress distributions.

## 7.2. Future work

This research has identified the need for future studies in following areas.

1. New ideas to improve the quality of bushing are still necessary for brittle cast metals. The deformation and fracture of work-material to form petals are not well understood. Practically, different ways to heat the workpiece, such as using the induction heating to locally raise the temperature on the spot of drilling or the tool, ultrasonic vibration of the workpiece, or designed tool features that cause frictional heating prior to drilling, need to be investigated in friction drilling.
2. Further study is needed to test the strength of the connection with friction drilled hole for different materials. Standardized tests of clampload, torque to failure, cycles to failure, etc. are needed. Performance of this connection should be compared to established joining methods, including weld nuts and threaded inserts, for accurate evaluation. Extension of FEM modeling to tapping process and connection can be investigated.
3. The FEM modeling can be extended to study the temperature and stress in the tool during friction drilling. This can be beneficial for the tool geometry design and tool material selection. A better tool geometry can also help to reduce the thrust force and deflection and improve bushing formation in the workpiece.
4. FEM modeling needs to be expanded to other friction stir technologies such as FSW and SFW. Development in SFW is lacking and would benefit from FEM modeling.

5. This study also shows that further developments of FEM are required to improve the modeling results. The deflection of workpiece was not accurately modeled and required further enhancement in modeling. The Coulomb friction model with a single coefficient of friction was limited to accurately predict the torque and the heat generation. The aluminum work-material is known to bond and adhere to the tool in friction drilling and creates a complicated friction behavior. A more comprehensive friction model depending on the temperature and pressure needs further investigation.